Cell

Stress-sensitive neural circuits change the gut microbiome via duodenal glands

Graphical abstract

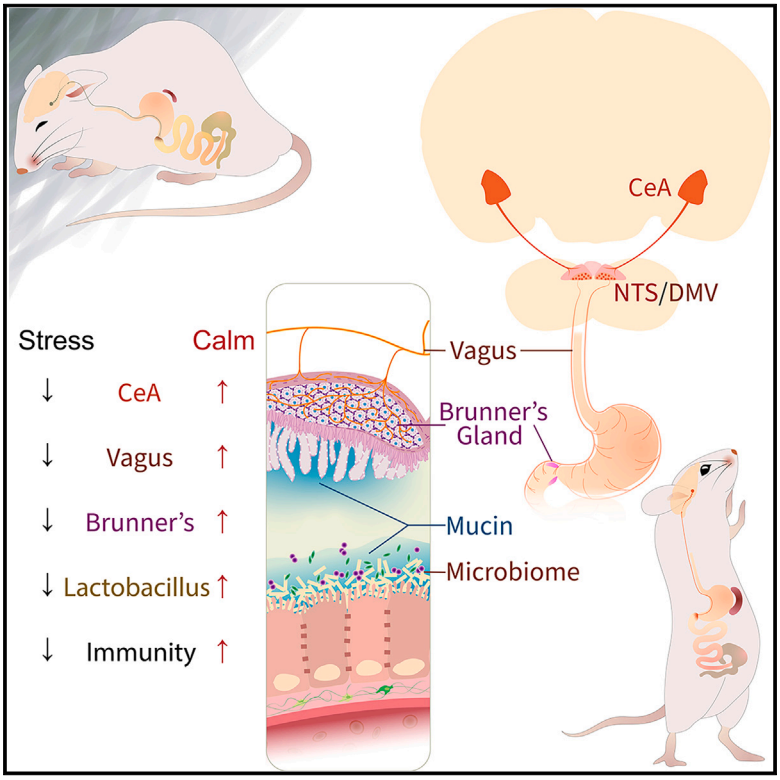

Highlights

- Secretion of mucin from the glands of Brunner promotes gut *Lactobacilli* proliferation
- Central amygdala neurons stimulate Brunner's glands via vagal nerves
- Stress inhibits the central amygdala, thereby suppressing Brunner's glands activity
- Impaired gland activity compromises *Lactobacilli* populations and host immunity

Authors

Hao Chang, Matthew H. Perkins, Leonardo S. Novaes, ..., Ruth E. Ley, Wenfei Han, Ivan E. de Araujo

Correspondence

hao.chang@mssm.edu (H.C.), wenfei.han@tuebingen.mpg.de (W.H.), ivan.dearaujo@tuebingen.mpg.de (I.E.d.A.)

In brief

Secretions from the duodenal glands of Brunner enhance host defense by promoting gastrointestinal *Lactobacilli* proliferation. Chronic stress inhibited a brain-vagus nerve circuit that stimulates glandular secretion, thereby suppressing *Lactobacillus* populations and systemic immunity.

Chang et al., 2024, Cell *187*, 5393–5412
September 19, 2024
https://doi.org/10.1016/j.cell.2024.07.019

CellPress

Cell

CellPress
OPEN ACCESS

Article

Stress-sensitive neural circuits change the gut microbiome via duodenal glands

Hao Chang,[1,*] Matthew H. Perkins,[1] Leonardo S. Novaes,[1] Feng Qian,[2] Tong Zhang,[3,4] Peter H. Neckel,[5] Simon Scherer,[6] Ruth E. Ley,[7] Wenfei Han,[8,*] and Ivan E. de Araujo[1,8,9,*]

[1]Nash Family Department of Neuroscience, Icahn School of Medicine at Mount Sinai, New York, NY 10029, USA
[2]AMPSeq, Gaithersburg, MD 20879, USA
[3]Department of General Surgery, Guangzhou First People's Hospital, Guangzhou 510180, Guangdong, China
[4]Guangzhou Municipal and Guangdong Provincial Key Laboratory of Protein Modification and Disease, Guangzhou Medical University, Guangzhou 510180, Guangdong, China
[5]Institute of Clinical Anatomy and Cell Analysis, University of Tübingen, Tübingen 72074, Germany
[6]Department of Pediatric Surgery and Pediatric Urology, University Children's Hospital, Tübingen 72076, Germany
[7]Max-Planck Institute for Biology, Tübingen 72076, Germany
[8]Max-Planck Institute for Biological Cybernetics, Tübingen 72076, Germany
[9]Lead contact
*Correspondence: hao.chang@mssm.edu (H.C.), wenfei.han@tuebingen.mpg.de (W.H.), ivan.dearaujo@tuebingen.mpg.de (I.E.d.A.)
https://doi.org/10.1016/j.cell.2024.07.019

SUMMARY

Negative psychological states impact immunity by altering the gut microbiome. However, the relationship between brain states and microbiome composition remains unclear. We show that Brunner's glands in the duodenum couple stress-sensitive brain circuits to bacterial homeostasis. Brunner's glands mediated the enrichment of gut *Lactobacillus* species in response to vagus nerve stimulation. Cell-specific ablation of the glands markedly suppressed *Lactobacilli* counts and heightened vulnerability to infection. In the forebrain, we mapped a vagally mediated, polysynaptic circuit connecting the central nucleus of the amygdala to Brunner's glands. Chronic stress suppressed central amygdala activity and phenocopied the effects of gland lesions. Conversely, excitation of either the central amygdala or parasympathetic vagal neurons activated Brunner's glands and reversed the effects of stress on the gut microbiome and immunity. The findings revealed a tractable brain-body mechanism linking psychological states to host defense.

INTRODUCTION

Gut microbiomes, i.e., the microbial communities of the intestinal mucosa, promote nutrient digestion and protection against foodborne pathogens.[1–5] Growing evidence indicates that psychological states impact systemic immunity by altering the host's microbiome,[3,6–8] highlighting a causal link between brain activity and gut bacterial homeostasis. Indeed, numerous human subjects and preclinical studies have reported associations between psychological stress and altered microbiomes.[9–12] In non-human primates, stress models such as maternal separation induce significant decreases in the levels of the beneficial bacteria *Lactobacillus* concomitantly with increasing vulnerability to opportunistic infections.[13] Consistent with this, rodent studies have shown that probiotic administration may improve emotional and physiological markers in models of anxiety.[14]

Such influences of brain states on the gut microbiome may occur via changes in mucosal-bacterial interactions.[8,15–18] Thus, in children, psychosocial stress was associated with deficient mucosal immune protection, reflecting both lower concentrations of secretory immunoglobulin A and increased occurrences of opportunistic infections.[19] Conversely, opposite effects are observed upon the induction of psychological relaxation.[20] Indeed, it is presumed that stress-induced suppression of *Lactobacillus* levels in primates was driven by inhibition of gut mucous secretion.[13] Unfortunately, it remains unknown how brain states may control mucosal secretion in such a way as to affect the microbiome.

Our main objective was to identify neuronal pathways that enable the brain to impact on the mucosa-microbiome system. The glands of Brunner, an exocrine structure confined to the duodenal submucosa, primarily consist of mucus-producing cells.[21–23] Critically, the glands of Brunner are distinctively targeted by nerve terminals, and neural stimulation is necessary for mucus secretion.[21,24,25] Of note, a significant proportion of these terminals are of vagal origin.[24] Thus, we hypothesized that vagal innervation of the mucosal glands of Brunner mediates the influence of psychological states on the microbiome. Accordingly, we probed this neural-glandular circuit using cell-specific approaches for single nuclei sequencing, ablation, intravital imaging, electrophysiological, and behavioral studies.

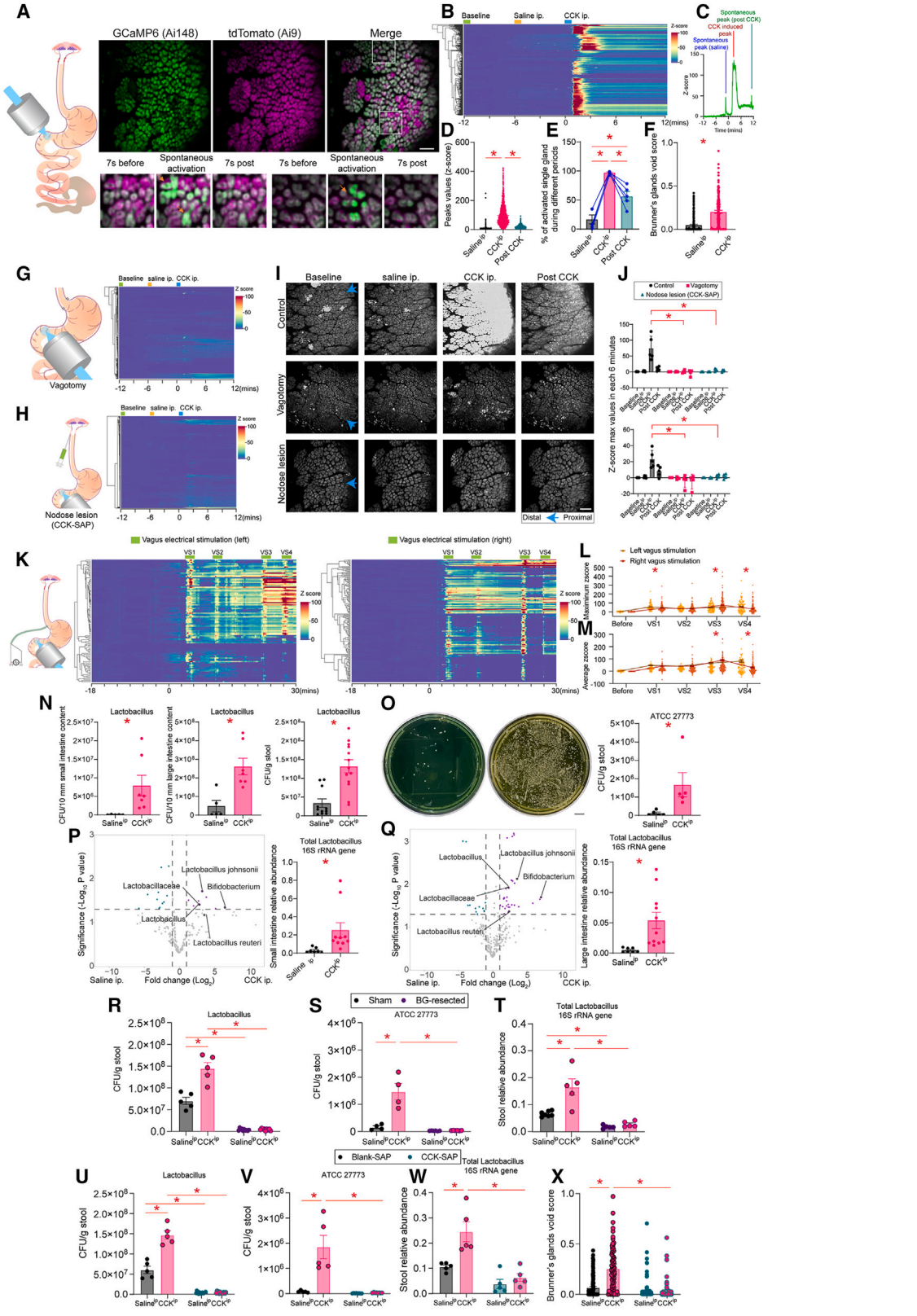

(legend on next page)

RESULTS

Vagal signals control BGs *in vivo*

Brunner's glands ("BGs") are located beneath the epithelium within the upper bulbar duodenal submucosa (Figure S1A). We first established the influence of the vagus nerve on BG activity *in vivo*. The glucagon-like peptide-1 (GLP-1) receptor is a molecular marker of BG,[21] and we generated Glp1r-ires-Cre×Ai148 (TIT2L-GC6f-ICL-tTA2)-D[GCamp6]×Ai9 ("Glp1r[GCamp6]") mice to cell-specifically express the fluorescent calcium indicator GCamp6 in BG (Figures S1B–S1E). We then implanted Glp1r [GCamp6] mice with an abdominal glass window to perform intravital imaging of intracellular calcium activity in the BG (Figure 1A; Video S1). To stimulate BG via the vagus nerve, we used the nutrient-responsive gut peptide cholecystokinin ("CCK,"[24,25] Figure S1F). Using this model, we evaluated the behavior of the glands *in vivo* CCK administration induced robust calcium transients throughout the BG (Figures 1B–1E; Video S2), with calcium currents following a proximal-to-distal spatiotemporal pattern (Figure S1G). We confirmed *in situ* CCK-induced mucus secretion from BG (Figures 1F and S1H–S1K). To assess the role of the vagus nerve in this phenomenon, we performed the same experiments in Glp1r[GCamp6] mice that sustained either subdiaphragmatic vagotomy ("VGx") or gut-specific sensory vagal denervation. In both cases, interrupting vagal transmission abolished BG responses to CCK (Figures 1G–1J and S1L–S1P). Thus, sensory vagal fibers are required for the CCK recruitment of BG *in vivo*.

To support these findings, we implanted a cuff electrode on the vagal trunk to deliver electrical pulses to the nerve in Glp1r [GCamp6] mice. Concomitant intravital BG imaging was performed. We found that vagal stimulation was sufficient to induce robust calcium transients across the BG (Figures 1K and S1Q). We detected a subtle but significant difference between stimulation of the left vs. right trunks, with the right nerve showing earlier latencies (Figures 1L and 1M).

BGs secretions promote *Lactobacillus* proliferation

Given the ability of CCK to engage BG mucosal secretion via the vagus nerve, we evaluated whether this nerve-glandular connection modulates the microbiome. Following 7 daily injections of CCK, we observed marked proliferation of *Lactobacillus* species in cultures from both the small and large intestine tissue, an effect also detected in fecal samples (Figures 1N and S1R–S1T). Consistently, daily CCK injections induced marked proliferation of *Lactobacillus rhamnosus* (American Type Culture Collection, [ATCC] 27773) after seeding the gut of mice with this strain (Figure 1O). Unbiased volcano plot analyses of 16S sequencing of small and large intestinal samples revealed that CCK promoted the proliferation of different *Lactobacilli* species, particularly *L. johnsonii* (Figures 1P and 1Q).

To investigate the role of BG, we designed a surgical approach to resect BG from the submucosa surrounding the duodenal bulb while preserving luminal and myenteric tissues (see STAR Methods and Table S1 for details). CCK-induced *Lactobacillus* growth was completely abolished after BG resection (Figures 1R–1T and S1U–S1HH).

We next evaluated whether lesions to vagal afferents phenocopy the effects of BG resection. Sensory vagal denervation equally abolished CCK-induced *Lactobacillus* growth (Figures 1U–1W), consistent with the inhibition of BG secretory activity (Figure 1X). Both vagal sensory denervation and BG resection

Figure 1. Vagal signals control the microbiome via the glands of Brunner

(A) Left: schematics of intravital BG imaging. Right: calcium (GCamP6) transients with unchanging control (tdTomato) signals. Scale bar, 100 μm.
(B) *Z* score heatmap showing robust calcium transients in BG after CCK.
(C) Calcium transient profile of a representative single gland.
(D) Maximum values (*Z* scores) of calcium transient peaks. Each condition was defined as a 6 min-long timelapse stack.
(E) Percentage of glands activated under each condition.
(F) BG void scores under the saline vs. CCK conditions.
(G) As in (B), but after subdiaphragmatic vagotomy.
(H) As in (G), but after vagal sensory denervation.
(I) Maximum intensity projections of calcium transients in intact mice or after vagal lesions. Scale bar, 100 μm.
(J) Upper: across-animals *Z* score maximal values for all groups and conditions. Lower: equivalent for mean *Z* score values.
(K) As in (B) calcium transients in the BG upon electrical stimulation of the left or right vagal nerve; VS1–4, vagal stimulation periods 1–4.
(L) Maximal calcium transient *Z* scores upon electrical stimulation of the left or right vagal nerve.
(M) As in (L) for mean *Z* scores.
(N) 7-day CCK treatment increased total *Lactobacilli* counts in small intestine, large intestine, and fecal samples.
(O) *Lactobacillus rhamnosus* (ATCC 27773) counts in feces after a 7-day CCK treatment. Left: representative clones cultured in deMan, Rogosa, Sharpe (MRS) plates; right: total clone count per 1 g sample/mouse, Sclae bar, 10 mm.
(P) Left: volcano plot comparing relative abundances of bacteria in the small intestine after 7-day CCK treatment. Cyan points represent downregulated and purple upregulated bacterial species. Right: relative abundances of total *Lactobacilli* counts.
(Q) Same as (P), but for large intestine.
(R) 7-day CCK treatment failed to increase fecal *Lactobacilli* counts in BG-resected mice.
(S) Similar to (R), but after oral inoculation with *Lactobacillus rhamnosus* (ATCC 27773).
(T) Relative abundances of total *Lactobacilli* after 7 days of CCK treatment in Sham- and BG-resected animals.
(U) 7-day CCK treatment failed to increase fecal *Lactobacilli* counts after vagal sensory denervation.
(V) Similar to (U), but after oral inoculation with *Lactobacillus rhamnosus* (ATCC 27773).
(W) Relative abundances of total *Lactobacilli* counts after 7 days of CCK treatment in control mice and after vagal sensory denervation.
(X) Void scores after CCK injections in control mice and after vagal sensory denervation.
All data are presented as mean ± SEM, $*p < 0.05$, see details in Table S3
See also Figure S1 and Videos S1 and S2.

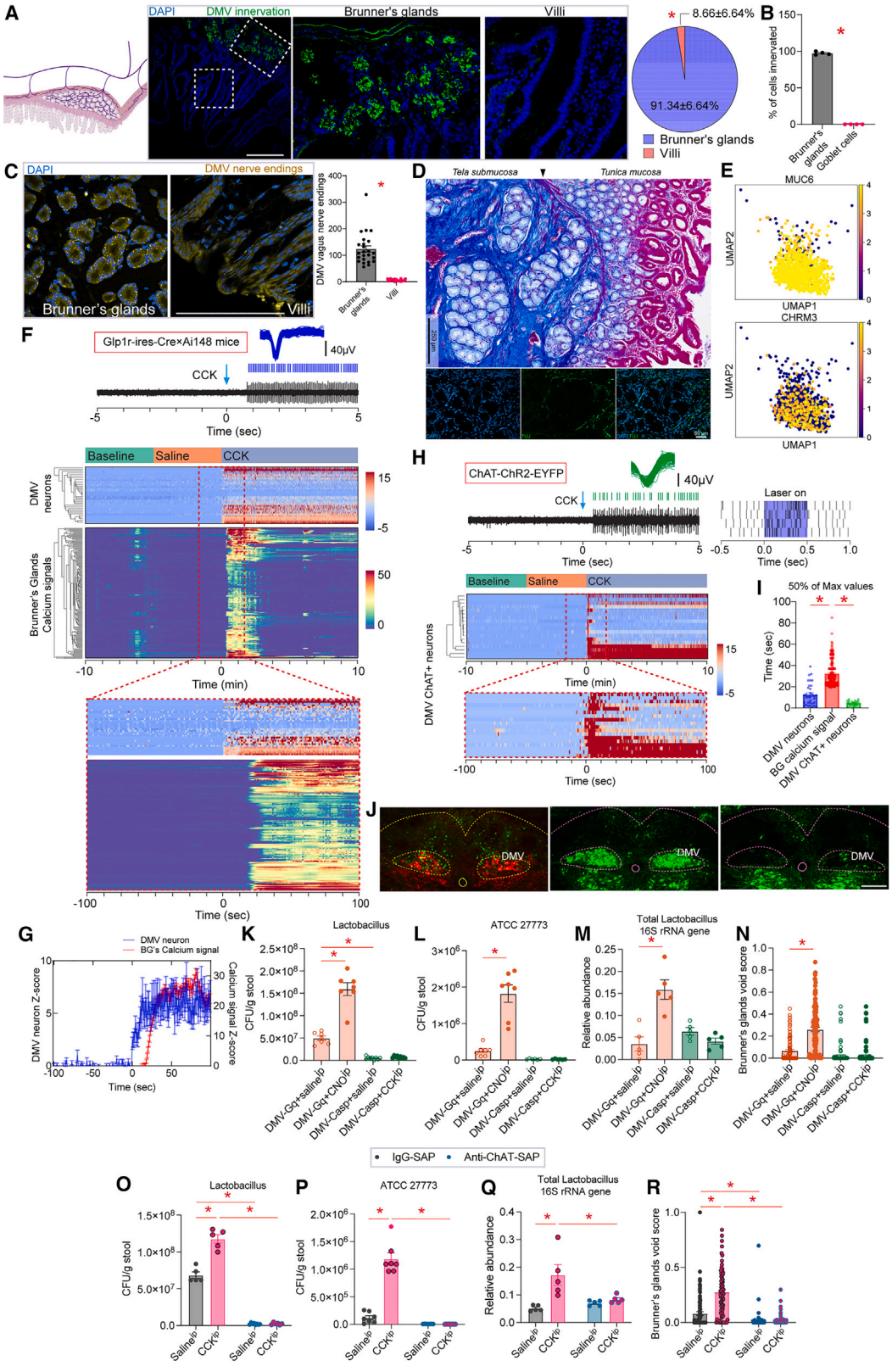

(legend on next page)

markedly reduced the mucosal thickness in the duodenum without affecting the pH values (Figures S1II–S1PP).

Vagal efferents are synaptically connected to BGs, which express pro-secretory cholinergic receptors at the single-cell level

Because CCK acts on afferent-to-efferent vagal circuits to induce biliary and pancreatic secretions,[26] we hypothesized that efferent neurons of the dorsal motor nucleus of the vagus ("DMV") control BG activity. We first confirmed that the glands are directly innervated by DMV. We injected the *Cre*-dependent construct AAV9-hSyn-DIO-GFP into the DMV of choline acetyltransferase (ChAT)-ires-Cre mice to label vagal efferent parasympathetic fibers. Dense efferent innervation was detected in BG but not in epithelial goblet mucous cells across the intestine (Figures 2A and 2B). This result reveals that the vagal influence on mucus secretion is specific to BG and does not involve epithelial mucous cells. Moreover, to detect parasympathetic synaptic endings on BG, we injected the *Cre*-dependent construct AAV1-hSyn-FLEx-mGFP-2A-Synaptophysin-mRuby into the DMV of ChAT-ires-Cre mice. Most vagal synaptic endings were clearly detected on the BG, whereas virtually no labeling was detected on the overlying villi (Figure 2C). This neuro-glandular arrangement parallels that observed in sections of human intestinal samples (Figure 2D; cf. Figure S2A).

Consistent with the aforementioned findings, single nuclei sequencing of RNA transcripts from proximal duodenal tissue revealed that cells expressing the mucin gene *Muc6*, which is distinctive of BG among duodenal cells,[22] constituted the only cell type clearly co-expressing the muscarinic receptor M3 gene (*Chrm3*), the cholinergic receptor critical for parasympathetic control of exocrine secretion[27] (Figures 2E and S2B–S2H). Dual *in situ* hybridization studies along with anatomical tracing revealed the co-expression of *Chrm3* and *Glp1r* in BGs, which were targeted by DMV fibers (Figure S2I). Of note, although *Glp1r* is expressed at relatively low levels in the BG of adults, *in situ* observations reveal its expression in all visualized glands. Consistent with the transcriptomics findings, administration of the specific muscarinic receptor M3 blocker darifenacin completely abolished CCK-induced activation of BG (Figure S2J). Consistently, darifenacin administration markedly suppressed *Lactobacillus* levels in fecal samples (Figure S2K).

Activation of the dorsal motor nucleus of vagus neurons is necessary and sufficient for the modulation of the gut microbiome

To assess the temporal relationship between the activities of DMV and BG, we recorded single neurons in the DMV of Glp1r-ires-Cre×Ai148 mice and simultaneously imaged calcium transients in BG. We found that after CCK injections, DMV neuronal activation reliably preceded increases in BG calcium signals (Figures 2F–2I and S2L). The latency for DMV neurons to reach 50% of the maximum value after CCK was ~12.6 s, whereas that for BG was ~32.3 s. Note that disparate latencies cannot be accounted for by single-cell spiking vs. calcium transient time resolution.

We next injected the *Cre*-dependent design receptor construct AAV9-DIO-hM3D(Gq)-mCherry into the DMV of ChAT-ires-Cre mice to induce cell-specific, chemogenetic activation of vagal efferent neurons. In a separate group of ChAT-ires-Cre mice, we injected into DMV the *Cre*-dependent construct AAV1-flex-taCasp3-TEVp to induce cell-specific ablation of vagal efferent neurons (Figures 2J and S2M–S2O). We found that, whereas DMV activation induced a striking increase in

Figure 2. Vagal efferents control Brunner's glands

(A) Left: cholinergic innervation of BG by DMV neurons. Center and right: magnified view of selected regions. Pie plot: percentage of BG vs. villus innervation. Scale bar, 100 μm.

(B) Percentage of innervated BG vs. goblet cells, the latter stained with anti-Muc2.

(C) DMV synaptic endings localized on Brunner's glands but not on overlying villi. Right: DMV synaptic endings on glands vs. villi. Data pooled from 5 mice. Scale bar 100 μm.

(D) Upper: histological cross-section through *Tunica mucosa* and *Tela submucosa* of the human duodenum. Brunner's glands are visualized underneath the Lamina *muscularis mucosae* (black arrowhead), embedded in the connective tissue of the *Tela submucosa*. Scale bar, 250 μm. Lower: neurites surrounding the human gland of Brunner. Scale bar, 50 μm.

(E) Single-cell transcriptomics of BG reveal *Muc6* co-expression with the pro-secretory cholinergic receptor *Chrm3*.

(F) Simultaneous recordings of DMV single neuron activity and BG calcium transients. Top trace: single unit activity. Scale bar, 40 μV.

(G) DMV neuronal responses to CCK precede responses in BG.

(H) Opto-tagging recordings of ChAT+ DMV cells. Top trace: single neuron activity and laser pulses for cell type identification. Scale bar, 40 μV.

(I) Latencies for CCK-induced 50% of maximum activity in DMV neurons and BG.

(J) Left-middle: expression of an excitatory chemogenetic construct (red) in cholinergic DMV neurons (green). Right: DMV-specific ablation of cholinergic neurons. Scale bar, 100 μm.

(K) DMV activation (7-day CNO) increased fecal *Lactobacilli* levels; 7-day CCK failed to increase *Lactobacilli* levels after cholinergic DMV ablation.

(L) Counts of inoculated *Lactobacillus rhamnosus* (ATCC 27773) in feces after 7 days of CNO in mice expressing chemogenetic constructs (DMV-Gq) and after 7 days of CCK in DMV cholinergic-ablated mice (DMV-Casp).

(M) Relative abundances of total *Lactobacilli* after treatments.

(N) Distribution of BG void scores across groups.

(O) 7-day CCK failed to increase fecal *Lactobacilli* levels after cholinergic denervation of BG (anti-ChAT-SAP).

(P) Similar to (O), but after the oral inoculation of *Lactobacillus rhamnosus* (ATCC 27773).

(Q) Relative abundances of total *Lactobacilli*.

(R) BG void scores across groups.

All data are presented as mean ± SEM,*$p < 0.05$, see details in Table S3.

See also Figure S2.

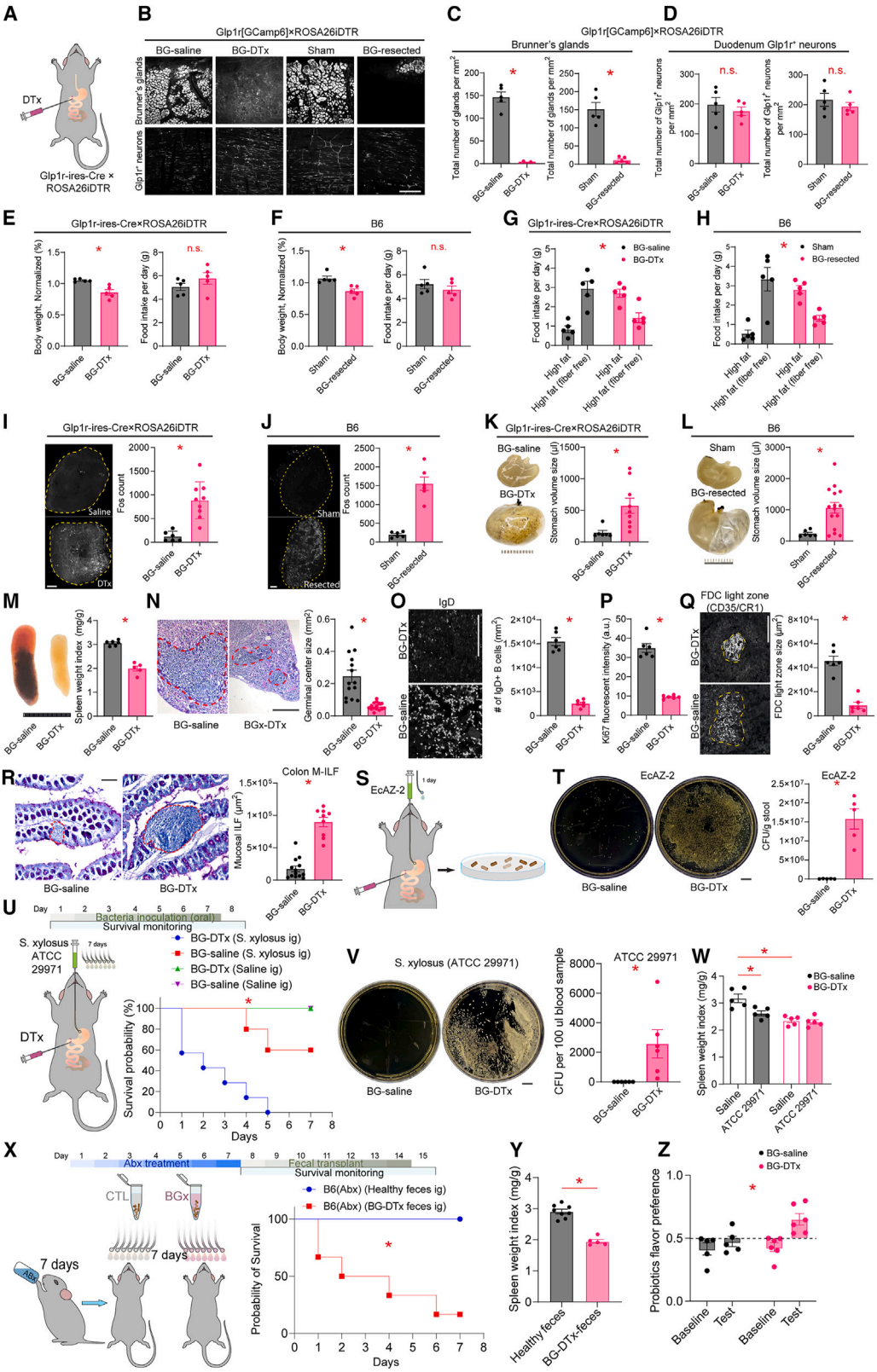

(legend on next page)

Lactobacillus counts, DMV ablation markedly suppressed *Lactobacillus* counts (Figures 2K–2M). In addition, while DMV activation enhanced duodenal (but not ileal or colonic) mucus thickness, DMV ablation markedly suppressed it (Figures 2N and S2P–S2S).

Finally, to assess the anatomical specificity of the above findings, we conducted ablation of cholinergic fibers targeting the BG by injecting the saporin ("SAP")-bound compound anti-ChAT-SAP into the BG region of the duodenal submucosa. Treatment selectively ablated DMV neurons (Figure S2T) and completely abolished CCK-induced BG activation (Figure S2U), *Lactobacillus* growth (Figures 2O–2Q), mucosal secretion (Figure 2R), and mucus thickness enhancement in the duodenum (Figures S2V–S2Y).

In sum, vagal cholinergic efferent neurons innervate BG to stimulate mucus secretion and *Lactobacillus* proliferation via the muscarinic receptor M3.

Cell-specific ablation of BGs leads to abnormalities in the spleen, sympathetic nervous system activation, mortality due to pathogen infection, and increased intestinal permeability

Because BG was found to be critical for microbiome composition, we tested whether gland ablation could lead to immunological and intestinal barrier dysfunction. We designed a strategy to cell-specifically ablate BG. We generated triple mutant Glp1r[GCamp6]×ROSA26iDTR mice to express the diphtheria toxin ("DTx") receptor ("DTR") exclusively in BG cells. Injections of DTx into the duodenal submucosa of Glp1r[GCamp6]×ROSA26iDTR mice phenocopied surgical resections in wild-type mice. Ablation of BG cells preserved duodenal and pancreatic GLP1R+ cells (Figures 3A–3D and S3A–S3E). Although both ablation approaches produced a mild but significant decrease in body weight (Figures 3E and 3F), they also induced higher preferences for fiber-rich vs. fiber-free fatty food pellets (Figures 3G, 3H, and S3F–S3K).

Altered microbiomes also induce overactivity in abdominal sympathetic neurons.[28] Therefore, we measured neuronal activity levels in the celiac ganglia (“CG”) of BG-lesioned mice. We observed marked increases in Fos reactivity in the CG of both BG-resected and BG-DTx mice (Figures 3I and 3J). These animals displayed severe gastric bloating (Figures 3K, 3L, and S3L–S3Q) and spleen contraction (Figures 3M–3Q), both in line with enhanced abdominal sympathetic tone.[29] Consistently, celiactomies reversed both the gastric and splenic phenotypes in BG-DTx mice (Figures S3R and S3S). In line with the sympathetic-induced effects described above, ablation of BG-innervating parasympathetic fibers recapitulated the effects of BG resection on splenic function (Figures S3T–S3DD). Finally, we note that spleen abnormalities were accompanied by a marked enlargement of mucosal lymphoid follicles in the colon of BG-DTx mice (Figure 3R).

We hypothesized that changes in the splenic and mucosal lymphoid tissues could indicate an ongoing immune response. We first tested the susceptibility of BG-DTx mice to gastrointestinal infections. We seeded the guts of both BG-DTx and BG-saline control mice with the *E. coli* strain EcAZ-2 via oral gavage and detected increases in EcAZ-2 counts in the excrement of BG-DTx mice (Figures 3S and 3T). We then performed the same experiment using the pathogenic *Staphylococcus xylosus* strain (ATCC 29971).[30] Although *S. xylosus* infection led to marked mortality in BG-DTx mice, all BG-saline control mice survived the infections (Figure 3U).

Finally, and in line with vulnerability to infection, we observed greater intestinal permeability in BG-DTx and BG-resected mice as assessed by measuring fluorescein isothiocyanate (FITC)-dextran in the systemic circulation after intraluminal administration (permeability in Duo-lesion resection controls

Figure 3. Ablation of the glands of the Brunner leads to an immunodeficiency syndrome and to mortality upon intestinal infection

(A) Strategy for cell-specific ablation of BG using diphtheria toxin (DTx) injections.
(B) Confocal microscopy visualization of ablation efficiency. Scale bar, 500 μm.
(C and D) Total number of glands/mm^2 or GLP1R+ neurons/mm^2 in the proximal duodenum.
(E and F) Normalized body weight (left) and daily food intake (in gram, right).
(G and H) Preferences of fiber-rich fatty pellets across groups.
(I and J) Neuronal activity levels (as indexed by Fos) in celiac ganglia (CG). Scale bars, 200 μm.
(K and L) Gastric distension across groups, with representative examples; scale bars, 1 cm.
(M and N) Spleen morphology and germinal center sizes across groups, with representative examples; scale bars, 1 cm (whole spleen) and 500 μm (germinal center). Spleen weight indexes obtained by normalizing spleen weight to body weight (mg/g).
(O) Representative sections and total counts of spleen IgD$^+$ B cells/mm^2 between groups. Scale bar, 100 μm.
(P) Mean Ki67 fluorescent intensity (cell proliferation marker) in spleen.
(Q) Representative sections and zone sizes of spleen follicular dendritic cell (FDC) markers. Scale bar, 100 μm.
(R) Representative sections and sizes of isolated colonic mucosal lymphoid follicles (M-ILFs) via periodic acid Schiff (PAS) staining. Scale bar, 100 μm.
(S) Inoculation with the kanamycin-resistant *E. coli* strain EcAZ-2.
(T) Representative culture plates and fecal counts after inoculation with EcAZ-2. Scale bar, 1 cm.
(U) Survival curves following gut colonization with the pathogenic *Staphylococcus xylosus* (ATCC 29971), log-rank test (Mantel-Cox), *$p < 0.0001$.
(V) Blood cultures after three daily oral inoculations with *S. xylosus* (ATCC 29971). Scale bar, 1 cm.
(W) Spleen weight indexes (mg/g BW) after three daily oral inoculations of *S. xylosus* (ATCC 29971).
(X) Mortality after transplanting fecal samples from BG-DTx and BG-saline mice into C57BL/6J specific-pathogen-free (SPF) mice after 7 days of treatment with an antibiotic cocktail (“Abx”). Log rank (Mantel-Cox), *$p < 0.001$.
(Y) As in (X), but for the spleen weight.
(Z) Preference indexes for probiotic solutions.
All data are presented as mean ± SEM, *$p < 0.05$, see details in Table S3.
See also Figure S3.

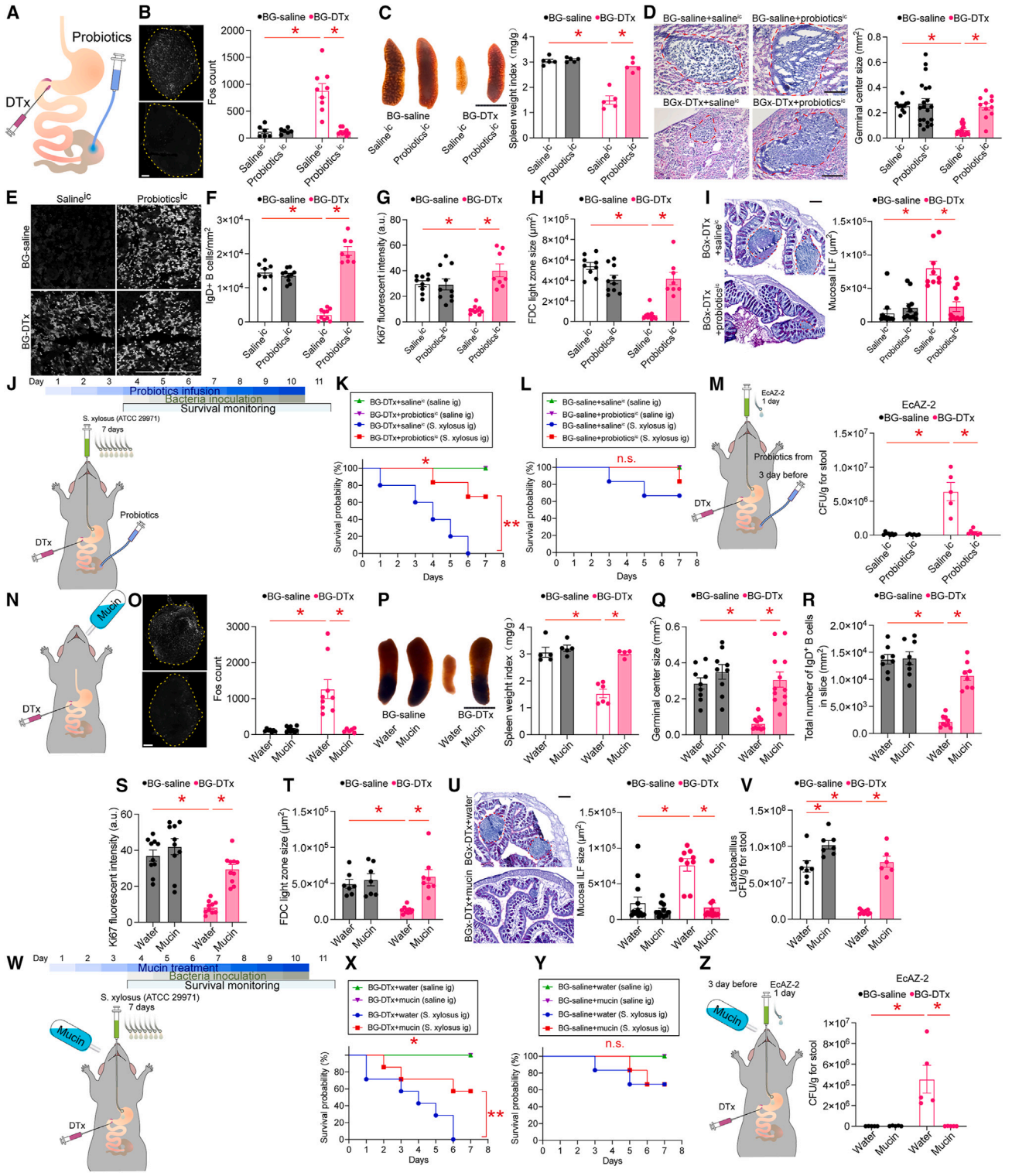

Figure 4. Probiotics and mucin restore immune functions and promote survival in animals lacking glands of Brunner

(A) Brunner's gland ablation combined with intra-cecal administration of [*Lactobacillus* + *Bifidobacteria*] probiotics.

(B) Neuronal (Fos) activity in celiac ganglia (CG). Scale bar, 200 μm.

(C) Spleen weights after probiotics. Left: representative examples of whole spleens. Scale bar, 1 cm. Right: spleen weight index.

(D) Germinal center sizes after probiotics. Left: representative examples using HE staining. Scale bar, 200 μm. Right: same as (C) but for the germinal center size.

(legend continued on next page)

returned to normality after recovery from surgery, Figures S3EE–S3GG). Consistently, after gut colonization, high levels of *S. xylosus* were detected in the blood of BG-DTx mice, whereas they remained undetected in control mice (Figures 3V and 3W). Overall, ablation of the glands of Brunner leads to a markedly weakened ability to fight intestinal infections and to increased gut barrier permeability.[31]

Fecal transplants from animals lacking BGs cause intestinal infection-associated mortality

We then assessed the physiological consequences of microbiome alteration in BG-DTx mice. We collected feces from both BG-saline and BG-DTx mice and prepared two liquid dilutions that were administered via gavage to two groups of wild-type mice previously treated with antibiotics for 7 days. We found that fecal transplants from BG-DTx mice induced significant mortality following a single oral inoculation with pathogenic bacteria; by contrast, all animals receiving fecal transplants from BG-saline mice survived the experiments. Figures 3X, 3Y, and S3HH–S3OO present a detailed description of the effects of BG-DTX microbiome transplantation.

To further validate the relevance of microbiome composition, we performed additional two-bottle preference tests on mice not treated with antibiotics. The tests revealed a striking increase in preference for solutions containing live *Lactobacilli + Bifidobacteria* probiotics in BG-DTx mice but not in control mice (Figure 3Z). Increased probiotic preference is potentially analogous to greater ingestion of fiber-containing foods after BG ablation (Figures 3G and 3H); indeed, both outcomes point to a motivation to behaviorally compensate for altered microbiomes.

Probiotic or mucin administration counteracts the syndrome associated with the ablation of BGs

We hypothesized that if the immunological syndrome following BG ablation is indeed due to an altered microbiome, probiotic or mucin administration could improve its symptoms. To test this hypothesis, we implanted a catheter into the cecum of BG-saline and BG-DTx mice (i.e., the mice sustaining cell-specific ablation of BG) for the administration of a 12-strain probiotic cocktail of *Lactobacilli* + *Bifidobacteria* (“Probiotics[*Lac* + *Bif*]”; see STAR Methods for details) or neutral solutions under a 2 × 2 design (Figure 4A). *Lactobacilli* + *Bifidobacteria* were chosen due to their enhancement by CCK (cf. Figures 1P and 1Q). Interestingly, administering Probiotics[*Lac* + *Bif*] to the cecum of BG-DTx mice completely reversed the sympathetic, splenic, and lymphoid abnormalities that follow BG ablation (Figures 4B–4I). Probiotics[*Lac* + *Bif*] also restored the body weight of BG-DTx mice to normal levels (Figure S4A). These effects occurred in the absence of significant changes in food intake or exploratory activity (Figures S4B and S4C). In addition, cecum infusions with Probiotics[*Lac* + *Bif*] in BG-DTx mice significantly decreased mortality after gut infection by *S. xylosus* (Figures 4J–4L). Finally, Probiotics[*Lac* + *Bif*] prevented bacterial *E. coli* proliferation after seeding the guts of BG-DTx mice with the EcAZ-2 strain (Figure 4M).

Since we initially hypothesized that BG might play a key role in mucosal-microbiome interactions, we reasoned that administering mucin solutions to animals would produce effects similar to those induced by Probiotics[*Lac* + *Bif*]. Indeed, providing a mucin solution to BG-DTx mice phenocopied the effects of Probiotics[*Lac* + *Bif*] by reversing the sympathetic, splenic, and mucosal lymphoid abnormalities that follow BG ablation (Figures 4N–4U). Mucin effects included reconstituting the gut barrier, duodenal mucus thickness (Figures S4D–S4K), and, strikingly, *Lactobacillus* levels (Figure 4V).

Finally, mucin consumption decreased mortality following gut infection by *S. xylosus* (Figures 4W–4Y). Mucin solutions also prevented bacterial proliferation after seeding the guts of BG-DTx mice with the *E. coli* strain EcAZ-2 (Figure 4Z). In summary, mucin secretion by BG appears to provide the conditions for *Lactobacillus* proliferation, which in turn regulates gut permeability, sympathetic tone, spleen morphology, and mucosal lymphoid enlargement.

(E and F) B cell counts after probiotic exposure. (E) Representative immunoglobulin D (IgD) immunostaining of spleen sections. Scale bar, 100 μm. (F) Same as (D) but for IgD+ counts.
(G) Proliferation markers after probiotics. Same as in (D) but for the Ki67 signal.
(H) Follicular dendritic cell (FDC) light zones after probiotics.
(I) Size of mucosal colonic lymphoid follicles (M-ILFs) after probiotics. Scale bar, 200 μm.
(J) Probiotics (or saline) followed by oral inoculation with the pathogenic *S. xylosus* (ATCC 29971).
(K and L) Mortality after *S. xylosus* (ATCC 29971) infection (or control), log-rank test (Mantel-Cox), $^*p < 0.001$.
(M) Probiotic effects on *E. coli* proliferation after gavage of EcAZ-2.
(N) Brunner’s gland ablation combined with oral administration of mucin.
(O) CG Fos expression after mucin. Scale bar, 200 μm.
(P) As in (C), but for mucin. Scale bar, 1 cm.
(Q) Same as (P), but for germinal center sizes.
(R) Same as (P), but for IgD+ counts.
(S) Similar to (P), but showing the Ki67 proliferation marker signal.
(T) Similar to (P), but showing follicular dendritic cell (FDC) light zones in the spleen.
(U) Same as in (P), but for colonic mucosal isolated lymphoid follicles (M-ILFs). Scale bar, 200 μm.
(V) *Lactobacilli* colony-forming unit (CFU) counts across groups after mucin.
(W–Z) Mucin ingestion rescues immunological function in mice lacking Brunner’s glands. (W) Schematics of Brunner’s gland-ablated mice combined with 10% mucin in drinking water (3 days), followed by 7 days of daily gavage with the pathogen *S. xylosus* (ATCC 29971) (combined with continued mucin availability).
(X and Y) As in (K) and (L), for mucin ingestion, $^*p < 0.001$. (Z) As in (M), for mucin ingestion.
All data are presented as mean ± SEM, $^*p < 0.05$, see details in Table S3.
See also Figure S4.

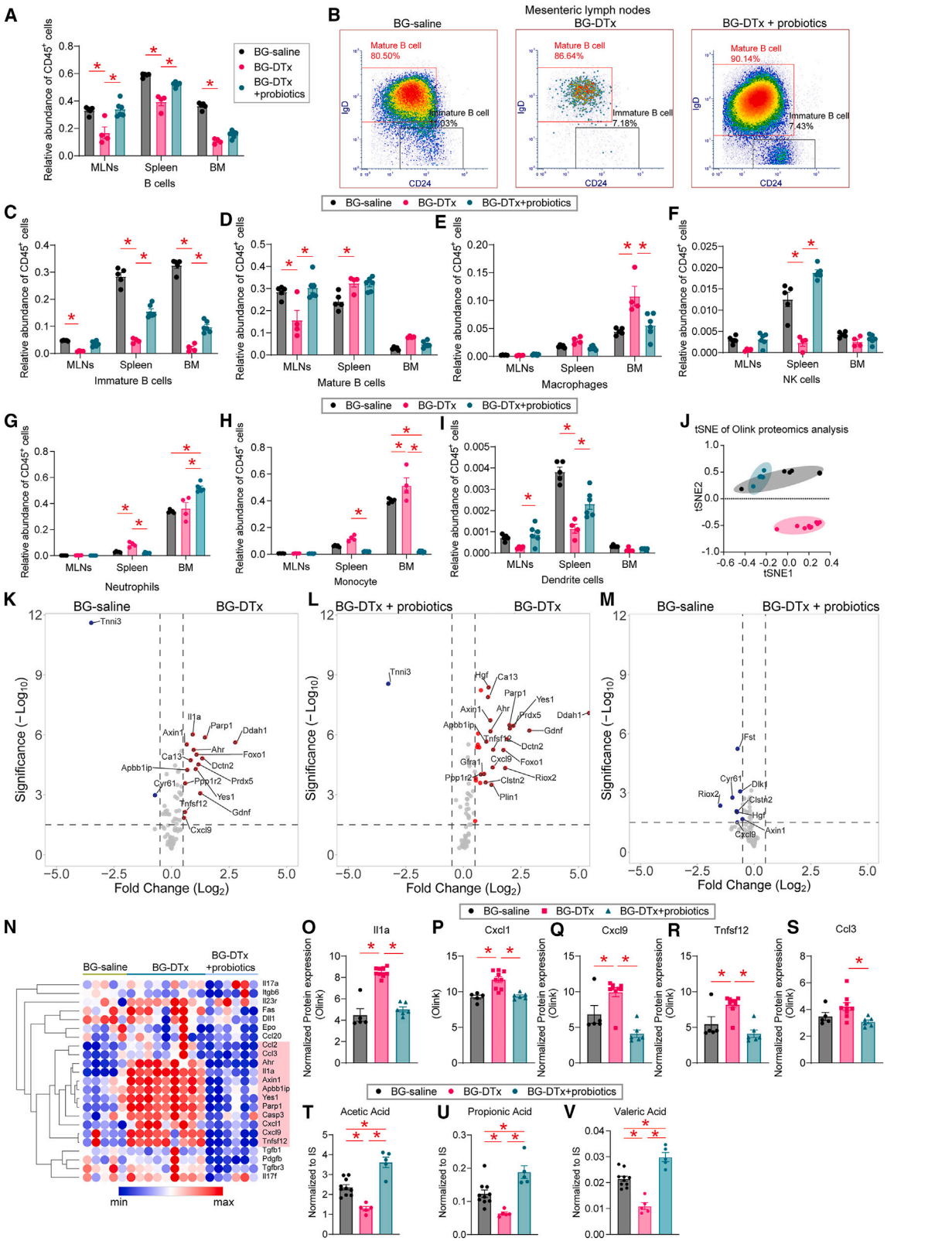

(legend on next page)

We also assessed the effects of probiotic administration on B cell counts. The rationale is based on the fact that the spleen is the primary lymphoid tissue that stores immature B cells. We anticipated that B cell counts and other immune factors would be altered in mice with BG lesions (which show altered spleen morphologies). We characterized the immune signatures of BG-saline (controls), BG-DTx, and BG-DTx+ Probiotics[*Lac* + *Bif*] mice. This was accomplished by performing cytometry by time of flight (CyTOF) analyses of the spleen, bone marrow, and mesenteric lymph node samples (Figure S5A).

BG ablation caused marked reductions in overall B cell counts, an effect that was (in some cases only partially) normalized by Probiotics[*Lac* + *Bif*] (Figures 5A, 5B, and S5B). Across tissues, immature B cells comprised the cell type affected by BG lesions that most significantly responded to Probiotics[*Lac* + *Bif*] (Figure 5C). By contrast, tissue-specific responses, particularly in the spleen, were observed for natural killer (NK) cells, neutrophils, monocytes, and dendritic cells (Figures 5D–5I and S5C–S5G). The effects were less conspicuous for other cell types, except for bone marrow macrophages, which were strongly induced by BG lesions but suppressed by Probiotics[*Lac* + *Bif*] (Figure 5E).

Resection of the duodenal bulb triggers immune responses in humans

We tested whether changes in the immunological profile after BG ablation appear to parallel findings in human subjects undergoing resection of the duodenal bulb (i.e., the first portion of the duodenum that contains the BGs). The subjects were patients with gastroduodenal stromal tumors; the comparison group underwent similar duodenal resections but in segments distal to the duodenal bulb. All patients were non-metastatic and were not treated with chemotherapy or radiation (surgery was curative; see STAR Methods). We found significant group effects associated with increased leucocyte, lymphocyte, neutrophil, and monocyte counts in patients whose duodenal bulb was removed compared with the removal of more distal duodenal sites. Surgery did not moderate this effect (Figures S5H–S5K). Although not specific to BG, these observations suggest that the duodenal bulb is a site of immune modulation in humans.

Brunner gland lesions increase the expression of proinflammatory cytokines and alter short-chain fatty acid profiles

We then suspected that changes in immune cell counts could trigger altered levels of circulating and colonic cytokines.[32] Proteomic (Olink) analyses conducted on blood samples from the same mice as described above revealed that BG ablation caused significant increases in the levels of proinflammatory and proapoptotic cytokines, both in the circulation and colonic tissue; these effects were largely reversed by Probiotics[*Lac* + *Bif*] (Figures 5J–5S and S5L–S5O).

Finally, we analyzed the blood contents of short-chain fatty acids, which are the main bacterial metabolites known to impact systemic physiology.[28] We found significant reductions in acetic, propionic, and valeric acid levels in BG-DTx mice; Probiotics [*Lac* + *Bif*] recovered metabolites to normal levels (Figures 5T–5V). Changes were less pronounced for butyric acid, isobutyric acid, hexanoic acid, and isohexanoic acid (Figures S5P–S5S).

A neuronal circuit connects the CeA to the glands of Brunner via the vagus nerve

We then sought to identify the brain regions that control vagal parasympathetic fibers innervating the BG. We first injected the *Cre*-dependent, polysynaptic, retrograde pseudorabies virus strain (“PRV”) PRV-CAG-DIO-TK-GFP into the proximal duodenal submucosa of Glp1r-ires-Cre mice. In addition to vagal parasympathetic neurons in the dorsal vagal complex (“DVC”), we detected clear labeling of BG origin in regions linked to autonomic control, especially the paraventricular and parasubthalamic *hypothalami*, *locus coeruleus*, and insular cortices. Interestingly, we observed dense labeling in the medial aspect of the central nucleus of the amygdala (“CeA”), a brain region deeply implicated in emotional regulation.[33,34] To verify that the wiring is dependent on the vagus nerve, we repeated the tracing experiment in Glp1r-ires-Cre mice that underwent bilateral subdiaphragmatic vagotomy. We found that severing the nerve at the abdominal level completely abolished labeling in the DVC and CeA (Figure 6A). By contrast, ablating the sympathetic CG and splenic nerves[35] did not affect labeling in most regions, including CeA (Figure S6A, which includes additional controls). Thus, CeA

Figure 5. Immune and metabolomics signatures are rescued by probiotic treatment in animals lacking the glands of Brunner

(A) Relative abundance of B cells among the total pool of live CD45$^+$ cells in mesenteric lymph node, spleen, and bone marrow samples from the experimental groups. The detailed gating strategy is shown in Figure S5A.
(B) B cell counts in mesenteric lymph nodes.
(C) Relative abundance of immature B cells from the total pool of CD45$^+$ cells in mesenteric lymph nodes, spleen, and bone marrow.
(D) As in (C), but for mature B cells.
(E) As in (C), but for macrophages.
(F) As in (C), but for natural killer (NK) cells.
(G) Similar to (C), but for neutrophil cells.
(H) Similar to (C), but for monocytes.
(I) As in (C), but for dendritic cells (DCs).
(J) Unsupervised clustering of proteomic analyses of blood samples from the three treatment groups.
(K) Volcano plots of blood proteomics profiles following BG ablation.
(L and M) Volcano plots of blood proteomics profiles following BG ablation with probiotic administration.
(N) Cytokine profile following BG ablation with probiotic administration.
(O–S) Levels of five inflammation-related cytokines, *Il1a* (O), *Cxcl1* (P), *Cxcl9* (Q), *Tnfsf12* (R), and *Ccl3* (S), following BG ablation with probiotics administration.
(T–V) Metabolomics analysis of blood samples after BG ablation with probiotic administration.
All data are presented as mean ± SEM, $^*p < 0.05$, see details in Table S3.
See also Figure S5 and Table S2.

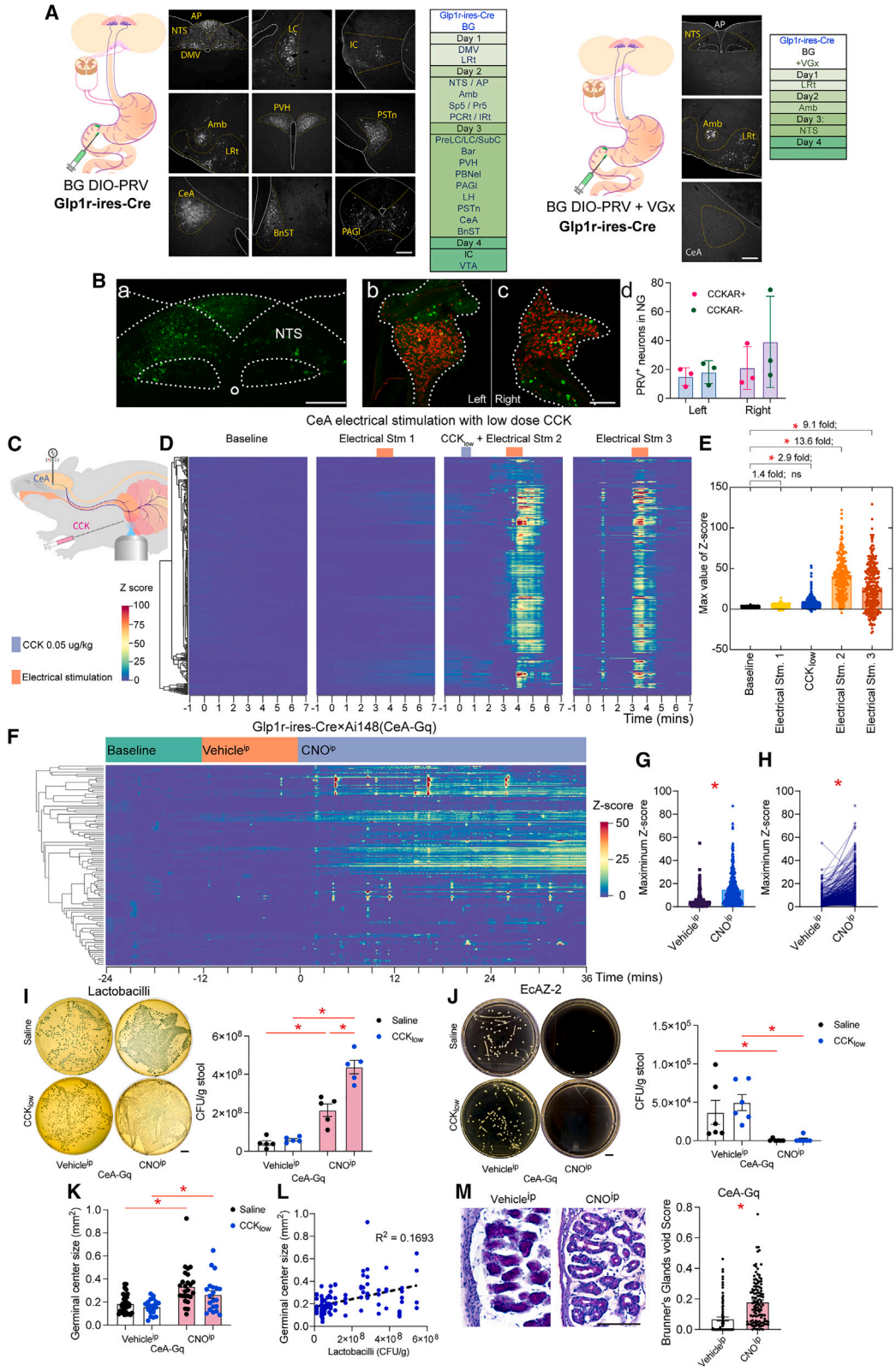

(legend on next page)

is neuronally connected to BG via vagal but not spinal/sympathetic pathways.

To perform the converse experiment, we injected the (non-*Cre*-dependent) Pseudorabies construct PRV-152-CMV-EGFP into the medial CeA of $Cckar^{Cre}$×Ai9 mice. Cholecystokinin A receptor (Cckar) is a marker of gut-innervating nodose neurons.[36] Retrograde labeling was visualized in the *nucleus tractus solitarius* ("NTS") and in both the right and left nodose ganglia (Figure 6B). A significant proportion of viral expression overlapped with the Cckar marker. This implies that in addition to controlling BG via vagal efferents, CeA may be modulated by gut sensory signals such as CCK.

We then tested whether this bidirectional gut-brain circuit was functional. We unilaterally implanted the tip of a stimulation electrode in the CeA of Glp1r[GCamp6] mice. We concomitantly performed intravital imaging of the BG (Figure 6C). First, we observed non-significant increases in BG calcium transients after brief electrical stimulation pulses were applied to CeA. We then decided to prime BG baseline activity levels by injecting mice with a subthreshold dose of CCK that was ineffective on its own ("CCK_{Low}"). Under these conditions, brief pulses of electrical stimulation of CeA caused robust, supra-additive increases in BG calcium transients (Figures 6D and 6E; Video S3). Consistently, BG transients remained unaltered in animals with splenic (sympathetic) nerve lesions (Figure S6B).

We investigated in more depth the ability of CeA to activate BG. We tested whether, unlike phasic, tonic neuronal activation is sufficient for gland activation independent of vagal priming with CCK. To modulate the activity of CeA neurons in awake animals, we performed chemogenetic activation of excitatory design receptors by expressing the construct AAV5-hSyn-hM3D(Gq)-mCherry into the CeA of wild-type mice and administering the designer drug clozapine-N-oxide ("CNO"). In line with the idea that CeA acts as a parasympathetic modulator, CNO injections induced strong neuronal activity in the DMV (Figure S6C). As anticipated, sustained, tonic activation of BG was observed without the requirement of CCK injections (Figures 6F–6H).

The ability of CeA to trigger sustained activity in BG indicates a potential role for the amygdala in modulating the microbiome. We found that CeA chemogenetic excitation was sufficient to markedly increase *Lactobacilli* counts in excrement of the stimulated mice; consistent with the BG imaging experiments above, this effect was further magnified by priming BG with CCK_{Low} (Figure 6I).

We then tested the ability of CeA stimulation to suppress the proliferation of exogenous gut bacteria. We again seeded mice with the *E. coli* strain EcAZ-2 via oral gavage. CeA chemogenetic excitation was sufficient to suppress EcAZ-2 proliferation, an effect that did not depend on CCK_{Low} (Figure 6J). In addition, we found that the same treatment caused a moderate, yet statistically significant, expansion of the spleen germinal centers (Figure 6K). Moreover, we again observed a significant, CeA-mediated within-subject correlation between *Lactobacillus* counts and germinal center areas (Figure 6L). Finally, because microbiome modulation depends on mucus release, we confirmed that chemogenetic CeA activation induces strong BG voiding (Figure 6M). These findings demonstrate the CeA-driven modulation of peripheral immune-related tissues via the microbiome.

Central amygdala-vagal-glandular connections mediate the effects of chronic stress on the microbiome and immunity

Previous studies in non-human primates, humans, and laboratory rodents have indicated that *Lactobacilli* are consistently reduced after stress.[37] We sought to verify whether such an effect is mediated by the CeA-DMV-BG circuitry.

We first recorded large neuronal ensembles in CeA in male and female mice exposed to either acute (one event) or chronic restraint stressors (6 daily exposures; see STAR Methods). Compared with baseline activity, chronic restraint stress produced widespread inhibition of neuronal activity across CeA; this effect was present during acute stress, although less pronounced (Figures 7A–7H and S7A–S7H for non-stressed controls).

Figure 6. Central nucleus of the amygdala controls the intestinal microbiome via modulation of Brunner's glands secretion

(A) Injection of a retrograde, cell-specific polysynaptic pseudorabies (PRV) strain into the duodenal submucosa resulted in dense labeling in well-defined subcortical regions (left), including the DMV and central nucleus of the amygdala (CeA). Most labeling, including DMV and CeA, was absent when tracing was performed after subdiaphragmatic vagotomy ("VGx") (right). Scale bars, 100 μm.

(B) Similar injections into CeA instead labeled *nucleus tractus solitarius* (NTS) (a), left (b), and right NG (c). (d) Counts of $Cckar^+$ and PRV^+ neurons in left vs. right nodose ganglia. Scale bars, 100 μm.

(C and D) *Z* score heatmap showing BG calcium transients in response to electrical stimulation of CeA in combination with a subthreshold dose of CCK.

(E) Maximal *Z* scores of calcium transients under different experimental conditions (300 glands analyzed from 3 mice).

(F–H) BG calcium transients in response to chemogenetic activation of CeA. (F) *Z* score heatmap showing BG calcium transients in response to chemogenetic stimulation of CeA. (G and H) Maximum *Z* score values for each BG.

(I) *Lactobacilli* CFU counts across experimental conditions. Scale bar, 1 cm.

(J) Effects of CeA stimulation and CeA stimulation + CCK_{Low} on EcAZ-2 oral inoculation, scale bar, 1 cm.

(K) Spleen germinal center size after CeA chemogenetic stimulation.

(L) Significant linear association between *Lactobacilli* CFU counts and spleen germinal center sizes across conditions ($n = 56$), Pearson, $^*p < 0.0001$.

(M) BG mucin exhaustion after CeA activation. Left: representative examples of BG in chemogenetic mice and controls. Scale bar, 100 μm. Right: distribution of BG void scores in chemogenetic mice and controls.

dorsal motor nucleus of the vagus, DMV; lateral reticular nucleus, LRt ; nucleus of the solitary tract / area postrema, NTS / AP ; nucleus ambiguus, Amb ; spinal trigeminal nucleus / principal trigeminal sensory nucleus, Sp5 / Pr5 ; parvicellular reticular nucleus / intermediate reticular nucleus, PCRt / IRt; per-locus coeruleus / locus coeruleus / subcoeruleus, PreLC / LC / SubC; Barrington's nucleus, Bar; paraventricular hypothalamic nucleus, PVH; parabrachial nucleus, externolateral part, PBNel; lateral periaqueductal gray, PAGl; lateral hypothalamus, LH; parasubthalamic nucleus, PSTn; central nucleus of the amygdala, CeA; bed nucleus of the stria terminalis, BnST; insular cortex, IC; ventral tegmental area, VTA. All data are presented as mean ± SEM, $^*p < 0.05$, see details in Table S3.

See also Figure S6 and Video S3.

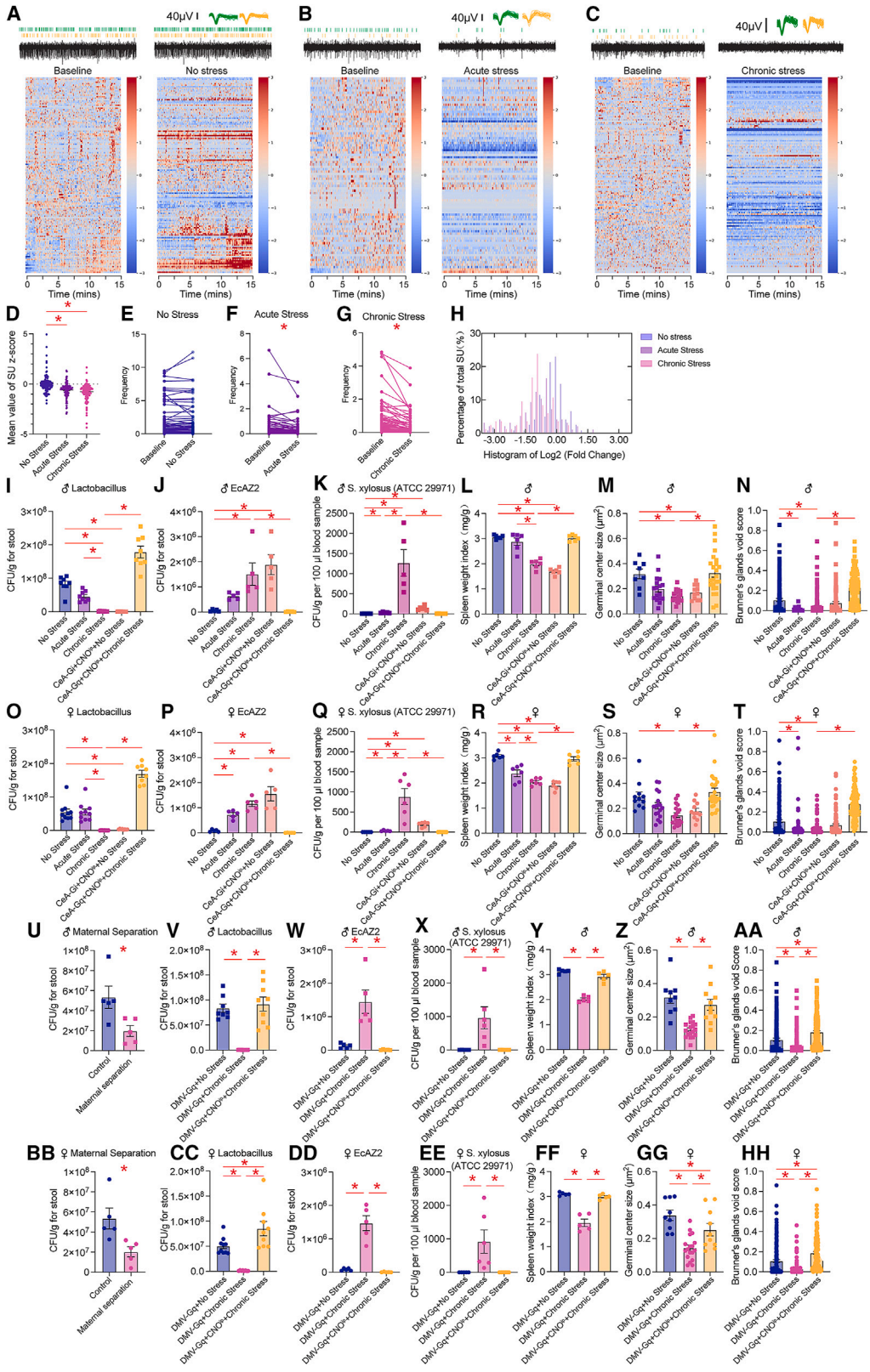

(legend on next page)

These findings indicate that the CeA-DMV-BG axis was inhibited by exposure to the stressor. In line with previous studies and our hypothesis, chronic stress not only strongly suppressed *Lactobacillus* counts but, remarkably, chemogenetic inhibition of CeA in non-stressed mice phenocopied this effect. By contrast, robust growth of *Lactobacillus* counts was observed upon chemogenetic stimulation of CeA in chronically stressed mice (Figure 7I). Thus, CeA bidirectionally controls microbiome composition, specifically *Lactobacillus* growth.

In line with the above, both stressor exposure and inhibition of CeA in non-stressed mice recapitulated phenotypes associated with BG lesions: stressed male and female mice were more vulnerable to gut infections, showed augmented gut permeability, and exhibited alterations in spleen morphology and immune profile (Figures 7J–7M and S7I–S7L for males and Figures 7O–7S and S7N–S7Q for females). Consistently, both stressor exposure and CeA inhibition suppressed BG mucus secretion (Figures 7N and 7T for males and females, respectively). Moreover, we note that suppression of *Lactobacillus* counts was not specific to physical restraint: maternal separation equally suppressed *Lactobacillus* counts in mice (replicating the pattern observed in primates; Figures 7U and 7BB for males and females, respectively).

Finally, and critically, if inhibition of the CeA-DMV pathway mediated the immunological impact of stress, then activation of either structure should be sufficient to reverse these effects. Indeed, chemogenetic stimulation of CeA in stressed male and female mice recovered *Lactobacillus* levels, prevented infections, decreased gut permeability, normalized spleen morphology, and reactivated BG mucus secretion (see Figures 7J–7N and S7I–S7L for males and Figures 7O–7T and S7N–S7Q for females). In line with the hypothesis that these effects are mediated by the CeA-DMV-BG circuitry, the ability of CeA activation to induce *Lactobacillus* growth was abolished by BG lesions (Figures S7M and S7R for males and females, respectively).

Consistent with the above, these effects were phenocopied by chemogenetic activation of DMV: chemogenetic stimulation of DMV in stressed male and female mice recovered *Lactobacilli* levels, prevented gastrointestinal infections, restricted gut permeability, normalized spleen morphology, and reactivated BG mucus secretion (see Figures 7V–7AA for males and Figures 7CC–7HH for females; see also Figures S7S–S7FF for

Figure 7. Amygdalo-vagal-glandular circuits are inhibited by chronic stress and mediate stress-induced altered intestinal microbiome and immunodeficiency

(A–C) Scale bars, 40 μV. (A) Top: representative traces of single CeA cell activity. Bottom: heatmap showing the Z-transform of the time-binned firing frequency of 126 CeA neurons calculated with respect to baseline under the no-stress condition. (B) As in (A) for 110 CeA neurons calculated with respect to baseline under acute stress condition. (C) As in (A) for 131 CeA neurons, calculated with respect to baseline under chronic stress conditions.
(D) *Z* score values of cells under both acute and chronic stress conditions compared with the no stress.
(E) Firing frequencies of 126 CeA neurons in the no-stress condition compared with baseline.
(F) Firing frequencies of 110 CeA neurons under acute stress compared with baseline.
(G) As in (F) for 131 CeA neurons under chronic stress condition.
(H) Histograms of firing frequencies (log_2), representing fold changes compared with baseline.
(I) *Lactobacilli* CFU counts in fecal samples from experimental groups and conditions, i.e., no stress, acute stress, chronic stress, CeA chemogenetic inhibition (CeA-Gi + CNO^{ip}), and CeA chemogenetic activation + chronic stress (CeA-Gq + CNO^{ip} + chronic stress) mice.
(J) EcAZ-2 proliferation in male mice in experimental groups and conditions.
(K) Translocation of orally delivered pathogenic *S. xylosus* (ATCC 29971) into the systemic circulation in male mice of different experimental groups and conditions.
(L and M) Spleen characteristics of male mice in different experimental groups and conditions. (L) Spleen sizes of male mice in different experimental groups and conditions. (M) Spleen germinal center sizes of male mice in the experimental groups and under different conditions.
(N) BG void scores of the experimental groups and conditions.
(O) As in (I), but for female mice.
(P) As in (J), but so for female mice.
(Q) As in (K), but for female mice.
(R and S) As in (L) and (M), but for female mice.
(T) As in (N), but so for female mice.
(U) *Lactobacilli* counts after maternal separation in male pups.
(V) *Lactobacilli* CFU counts in the fecal samples of chronically stressed male mice sustaining chemogenetic activation of DMV.
(W) EcAZ-2 proliferation in chronically stressed male mice sustaining chemogenetic activation of DMV.
(X) Translocation of pathogenic bacteria into systemic circulation in chronically stressed male mice sustaining chemogenetic activation of DMV.
(Y and Z) Altered spleen characteristics in male mice. (Y) Spleen sizes of chronically stressed male mice that sustain the chemogenetic activation of DMV. (Z) Spleen germinal center sizes in chronically stressed male mice that sustain chemogenetic activation of DMV.
(AA) BG void scores from chronically stressed male mice that sustain chemogenetic activation of DMV.
(BB) As in (U), but so for female mice.
(CC) As in (V) but for female mice.
(DD) As in (W), but for female mice.
(EE) As in (X), but so for female mice.
(FF) As in (Y), but for female mice.
(GG) As in (Z), but so for female mice.
(HH) As in (AA), but so for female mice.
All data are presented as mean ± SEM, $*p < 0.05$, see details in Table S3
See also Figure S7.

additional details and validation of the chemogenetic approach). In summary, activation of either the central amygdala or vagal parasympathetic nervous system is sufficient to completely reverse the effects of stress on the microbiome and immunity.

DISCUSSION

We identified a stress-sensitive neuroglandular circuit that links brain states to changes in the gut microbiome. Emotion-related brain circuits control the glands of Brunner via the vagus nerve; mucosal secretions from these glands support the proliferation of microbes, particularly *Lactobacilli*. Indeed, several lines of evidence from non-human primates, laboratory rodents, and humans demonstrate that gut bacteria in the genus *Lactobacillus* are significantly reduced during stress.[37]

A neuroepithelial circuit for gut mucus secretion has been demonstrated for goblet cells. Specifically, gut sensory nociceptor fibers engage the calcitonin gene-related peptide (CGRP)-Ramp1 pathway to induce goblet cell emptying and mucus secretion.[38] Interestingly, genetic disruption of gut nociceptors also leads to severe inflammation and alterations in the intestinal microbiota, including a transmissible dysbiosis.[39] These findings indicate that extrinsic gastrointestinal nerves play a critical role in controlling the microbiome by targeting mucus-secreting cells. Moreover, recent findings have implicated colonic enteric neurons in the relationship between psychological stress and intestinal inflammation.[40] Our study adds to this emerging picture by revealing a neuroglandular circuit through which vagal fibers target the submucosal glands of the upper intestine to promote bacterial homeostasis.

Our results implicate BGs in the generation of altered immunity in response to chronic stressors. The proposed model suggests the following sequence of events: mucin release from BGs serves as a substrate for *Lactobacilli* proliferation. When stress inhibits mucus release, *Lactobacilli* growth is similarly suppressed. The effects of the latter include enhanced gut permeability, sympathetic overtone, and lymphoid tissue abnormalities (especially contraction of spleen and overgrowth of mucosal lymphoid follicles). Inoculation with probiotics appears to be sufficient to mitigate these negative effects: while *Lactobacillus* + *Bifidobacteria* administration restored the integrity of the gut barrier and lessened sympathetic nerve activity, antibiotic-treated animals displayed enhanced gut permeability. These findings are in agreement with studies demonstrating that commensal bacteria, especially *Lactobacilli*, enhance gut barrier function by upregulating epithelial tight junction proteins.[41,42]

Our findings are therefore directly consistent with the notion that efferent vagal fibers promote immune function and anti-inflammatory signaling.[43] Of particular interest are the reported beneficial effects of vagal cholinergic signaling on spleen function,[44] which parallel our findings linking the glands of Brunner with splenic characteristics. Our proposed circuit may, on the one hand, clarify the mechanisms by which the vagus nerve reduces inflammatory states via the spleen. Indeed, we showed that vagal stimulation expands the spleen tissue in opposition to sympathetic effects. The beneficial effects of vagus nerve stimulation may be mediated by enhanced mucosal integrity. Noninvasive (auricular branch) vagal nerve stimulation reduced the permeability of the small intestine in human subjects pretreated with intravenous administration of stress hormones.[45] This effect is consistent with preclinical studies in which vagal stimulation reversed stress-induced changes in intestinal permeability[46] and attenuated inflammatory bowel disease symptoms.[47] The mechanisms linking vagal cholinergic signaling and intestinal barrier integrity remain, however, unknown.[47] Thus, this study suggests that the glands of Brunner and their mucus secretion may account for at least part of the protective effects of vagal stimulation on gut mucosal immunity. In line with this idea, our findings demonstrate that vagal parasympathetic activity bidirectionally modulates microbiome composition, including in response to stressors.

In addition to cholinergic signaling, the sensory branch of the vagus nerve may be involved in microbiome modulation. Indeed, we found that CCK, a pro-digestive gut hormone[48] whose action depends on vagal sensory ganglia,[49] promotes the expansion of *Lactobacilli* populations via BGs. This suggests the possibility that *Lactobacilli* populations expand in response to the activity of vagal nutrient-sensing fibers. Moreover, vagal sensory fibers can sense intestinal microbial content. Probiotic administration improved physiological markers in rodent models of anxiety, an effect mediated by vagal sensing.[14] Indeed, the vagal sensory ganglia sense bacterial metabolites, mediating the generation of autonomic responses in response to bacterial signaling.[28] These findings agree with our observations that mice with lesions in the glands of Brunner developed preferences for fiber-enriched pellets and probiotic-containing drinking solutions. Dietary fibers promote *Lactobacilli* and *Bifidobacteria* growth[50] and suppress metabolic syndrome in animals with altered microbiomes.[51] In other words, the effects of altered microbiomes may be sensed via interoceptive pathways,[52–54] enabling the triggering of compensatory behavioral responses.

Finally, we found that the CeA, a subcortical area within the temporal lobes, controls BGs and modulates the microbiome. Central amygdala neurons are fundamentally implicated in emotional behavior.[33,34,55,56] The central amygdala plays a major role in conditioned fear and anxiety,[33,57,58] and may thus be a critical link between negative psychological states and altered microbiomes. We found that stressor exposure robustly inhibited neuronal activity in the central amygdala and that central amygdala inhibition recapitulates the effects of stress on the gut microbiome and immunity. In line with this idea, gut-borne vagal sensory signals were shown to modulate anxiety states via the central amygdala.[59] Consistent with the aforementioned findings, *L. rhamnosus*, a *Lactobacillus* species we found to be regulated by CCK, reduced stress-induced anxiety- and depression-like behaviors by modulating the forebrain levels of gamma-aminobutyric acid (GABA), the major neurotransmitter of the central amygdala, via the vagus nerve.[14] Our findings demonstrate that central amygdala activity bidirectionally modulates microbiome composition. Alterations in amygdala processing may underlie psychological disorders whose severity is correlated with the degree of microbiome alteration.

Limitations of the study

An important limitation of this study was the absence of experiments involving BG lesions in germ-free animals. In fact, both our approaches to lesioning the glands involved invasive procedures

that could compromise the germ-free status of the subjects. Unfortunately, our single-cell transcriptome analyses failed to reveal clear genetic markers specific to BGs (i.e., when considering the whole organism). Although this limitation does not directly impact our conclusions, future intersectional genetic approaches may enable the targeting of BGs without the need for invasive interventions. Finally, while we focused primarily on neuroimmune circuitries, future studies should advance our understanding of the mechanisms linking BG, *Lactobacillus*, and host immunity.

STAR★METHODS

Detailed methods are provided in the online version of this paper and include the following:

- KEY RESOURCES TABLE
- RESOURCE AVAILABILITY
  - Lead contact
  - Materials availability
  - Data and code availability
- EXPERIMENTAL MODEL AND STUDY PARTICIPANT DETAILS
  - Experimental Animals
- METHOD DETAILS
  - Lesions of the glands of Brunner
  - Vagal, Splenic Nerve, and sympathetic ganglia lesions
  - Brain stereotactic surgeries
  - In vivo electrophysiological recordings with opto-tagging
  - *In vivo* electrophysiological recordings during exposure to stressor
  - Intravital window for confocal microscopy
  - In vivo ultrasound studies
  - Gut permeability
  - Intraperitoneal Glucose Tolerance Tests
  - Oral glucose tolerance tests
  - Behavioral tests
  - Bacterial manipulations
  - Analyses of microbiome composition
  - Vesicles and membrane secretion analysis
  - Pseudorabies virus tracing
  - Histology analysis
  - Immunohistology of human Brunner's glands
  - Single nuclei sequencing
  - CyTOF
  - Olink proteomics analysis
  - Metabolomics analysis for Short Chain Fatty Acids
- QUANTIFICATION AND STATISTICAL ANALYSIS
  - Mouse behavioral data analysis
  - Calcium imaging data analysis
  - Electrophysiology data analysis
  - Single nuclei sequencing data analysis

SUPPLEMENTAL INFORMATION

Supplemental information can be found online at https://doi.org/10.1016/j.cell.2024.07.019.

ACKNOWLEDGMENTS

Food Allergy Science Initiative Consortium (to I.E.d.A.), NIH-NCCIH R01 AT011697-01 (to I.E.d.A.), and Modern Diet and Physiology Research Center (to I.E.d.A.). We thank Dr. Amir Zarrinpar for providing the engineered *E. coli* strain EcAZ-2. We thank Geoffrey Kelly and Kai Nie, Mount Sinai Human Immune Monitoring Center, for assistance in processing CyTOF and Olink samples. We also thank Drs. Nikos Tzavaras, Shilpa Kumar, and Glenn Doherty, Mount Sinai Microscopy CoRE, for assisting us with accomplishing intravital imaging of calcium transients, and Dr. Manuel Gonzalez-Rodrigues, Mount Sinai Neurometabolomics and Neuroinformatics Core, for the processing and analyses of short-chain fatty acids.

AUTHOR CONTRIBUTIONS

I.E.d.A. conceived and supervised experiments; H.C. and W.H. designed, performed, interpreted, and analyzed all mouse experiments. F.Q. performed and analyzed 16S sequencing. H.C. and W.H. implemented intravital imaging. M.H.P. implemented electrophysiology system. L.S.N. performed behavioral assessments. P.H.N. and S.S. performed human tissue analyses. T.Z. acquired and analyzed human patient data. R.L. supervised microbiome analyses. I.E.d.A., W.H., and H.C. wrote manuscript. All authors interpreted data and edited manuscript.

DECLARATION OF INTERESTS

The authors declare no competing interests.

Received: October 31, 2023
Revised: May 13, 2024
Accepted: July 12, 2024
Published: August 8, 2024

REFERENCES

1. Ley, R.E., Peterson, D.A., and Gordon, J.I. (2006). Ecological and evolutionary forces shaping microbial diversity in the human intestine. Cell *124*, 837–848. https://doi.org/10.1016/j.cell.2006.02.017.
2. Ley, R.E., Lozupone, C.A., Hamady, M., Knight, R., and Gordon, J.I. (2008). Worlds within worlds: evolution of the vertebrate gut microbiota. Nat. Rev. Microbiol. *6*, 776–788. https://doi.org/10.1038/nrmicro1978.
3. Cryan, J.F., and Dinan, T.G. (2012). Mind-altering microorganisms: the impact of the gut microbiota on brain and behaviour. Nat. Rev. Neurosci. *13*, 701–712. https://doi.org/10.1038/nrn3346.
4. Thaiss, C.A., Zmora, N., Levy, M., and Elinav, E. (2016). The microbiome and innate immunity. Nature *535*, 65–74. https://doi.org/10.1038/nature18847.
5. Khosravi, A., Yáñez, A., Price, J.G., Chow, A., Merad, M., Goodridge, H.S., and Mazmanian, S.K. (2014). Gut microbiota promote hematopoiesis to control bacterial infection. Cell Host Microbe *15*, 374–381. https://doi.org/10.1016/j.chom.2014.02.006.
6. Fülling, C., Dinan, T.G., and Cryan, J.F. (2019). Gut Microbe to Brain Signaling: What Happens in Vagus…. Neuron *101*, 998–1002. https://doi.org/10.1016/j.neuron.2019.02.008.
7. Allen, A.P., Dinan, T.G., Clarke, G., and Cryan, J.F. (2017). A psychology of the human brain-gut-microbiome axis. Soc. Personal. Psychol. Compass *11*, e12309. https://doi.org/10.1111/spc3.12309.
8. Lyte, M., Vulchanova, L., and Brown, D.R. (2011). Stress at the intestinal surface: catecholamines and mucosa-bacteria interactions. Cell Tissue Res. *343*, 23–32. https://doi.org/10.1007/s00441-010-1050-0.
9. Chen, Y.H., Bai, J., Wu, D., Yu, S.F., Qiang, X.L., Bai, H., Wang, H.N., and Peng, Z.W. (2019). Association between fecal microbiota and generalized anxiety disorder: Severity and early treatment response. J. Affect. Disord. *259*, 56–66. https://doi.org/10.1016/j.jad.2019.08.014.
10. Foster, J.A., Rinaman, L., and Cryan, J.F. (2017). Stress & the gut-brain axis: Regulation by the microbiome. Neurobiol. Stress *7*, 124–136. https://doi.org/10.1016/j.ynstr.2017.03.001.
11. Bailey, M.T., Dowd, S.E., Galley, J.D., Hufnagle, A.R., Allen, R.G., and Lyte, M. (2011). Exposure to a social stressor alters the structure of the intestinal microbiota: implications for stressor-induced immunomodulation. Brain Behav. Immun. *25*, 397–407. https://doi.org/10.1016/j.bbi.2010.10.023.

12. Morita, C., Tsuji, H., Hata, T., Gondo, M., Takakura, S., Kawai, K., Yoshihara, K., Ogata, K., Nomoto, K., Miyazaki, K., et al. (2015). Gut Dysbiosis in Patients with Anorexia Nervosa. PLoS One *10*, e0145274. https://doi.org/10.1371/journal.pone.0145274.

13. Bailey, M.T., and Coe, C.L. (1999). Maternal separation disrupts the integrity of the intestinal microflora in infant rhesus monkeys. Dev. Psychobiol. *35*, 146–155. https://doi.org/10.1002/(SICI)1098-2302(199909)35:2<146::AID-DEV7>3.0.CO;2-G.

14. Bravo, J.A., Forsythe, P., Chew, M.V., Escaravage, E., Savignac, H.M., Dinan, T.G., Bienenstock, J., and Cryan, J.F. (2011). Ingestion of Lactobacillus strain regulates emotional behavior and central GABA receptor expression in a mouse via the vagus nerve. Proc. Natl. Acad. Sci. USA *108*, 16050–16055. https://doi.org/10.1073/pnas.1102999108.

15. Guzmán-Mejía, F., Godínez-Victoria, M., Vega-Bautista, A., Pacheco-Yépez, J., and Drago-Serrano, M.E. (2021). Intestinal Homeostasis under Stress Siege. Int. J. Mol. Sci. *22*, 5095. https://doi.org/10.3390/ijms22105095.

16. Donaldson, G.P., Ladinsky, M.S., Yu, K.B., Sanders, J.G., Yoo, B.B., Chou, W.C., Conner, M.E., Earl, A.M., Knight, R., Bjorkman, P.J., et al. (2018). Gut microbiota utilize immunoglobulin A for mucosal colonization. Science *360*, 795–800. https://doi.org/10.1126/science.aaq0926.

17. Yoo, B.B., and Mazmanian, S.K. (2017). The Enteric Network: Interactions between the Immune and Nervous Systems of the Gut. Immunity *46*, 910–926. https://doi.org/10.1016/j.immuni.2017.05.011.

18. Johansson, M.E.V., Larsson, J.M.H., and Hansson, G.C. (2011). The two mucus layers of colon are organized by the MUC2 mucin, whereas the outer layer is a legislator of host-microbial interactions. Proc. Natl. Acad. Sci. USA *108*, 4659–4665. https://doi.org/10.1073/pnas.1006451107.

19. Drummond, P.D., and Hewson-Bower, B. (1997). Increased psychosocial stress and decreased mucosal immunity in children with recurrent upper respiratory tract infections. J. Psychosom. Res. *43*, 271–278. https://doi.org/10.1016/s0022-3999(97)00002-0.

20. Hewson-Bower, B., and Drummond, P.D. (1996). Secretory immunoglobulin A increases during relaxation in children with and without recurrent upper respiratory tract infections. J. Dev. Behav. Pediatr. *17*, 311–316. https://doi.org/10.1097/00004703-199610000-00004.

21. Voetmann, L.M., Underwood, C.R., Rolin, B., Hansen, A.K., Kirk, R.K., Pyke, C., Knudsen, L.B., and Frederiksen, K.S. (2022). In vitro cell cultures of Brunner's glands from male mouse to study GLP-1 receptor function. Am. J. Physiol. Cell Physiol. *322*, C1260–C1269. https://doi.org/10.1152/ajpcell.00345.2021.

22. Krause, W.J. (2000). Brunner's glands: a structural, histochemical and pathological profile. Prog. Histochem. Cytochem. *35*, 259–367. https://doi.org/10.1016/S0079-6336(00)80006-6.

23. Leeson, T.S., and Leeson, C.R. (1968). The fine structure of Brunner's glands in man. J. Anat. *103*, 263–276.

24. Moore, B.A., Kim, D., and Vanner, S. (2000). Neural pathways regulating Brunner's gland secretion in guinea pig duodenum in vitro. Am. J. Physiol. Gastrointest. Liver Physiol. *279*, G910–G917. https://doi.org/10.1152/ajpgi.2000.279.5.G910.

25. Lang, I.M., and Tansy, M.F. (1982). Neural and hormonal control of Brunner's gland secretion. Life Sci. *30*, 409–417. https://doi.org/10.1016/0024-3205(82)90456-8.

26. Travagli, R.A., and Anselmi, L. (2016). Vagal neurocircuitry and its influence on gastric motility. Nat. Rev. Gastroenterol. Hepatol. *13*, 389–401. https://doi.org/10.1038/nrgastro.2016.76.

27. Nakamura, T., Matsui, M., Uchida, K., Futatsugi, A., Kusakawa, S., Matsumoto, N., Nakamura, K., Manabe, T., Taketo, M.M., and Mikoshiba, K. (2004). M(3) muscarinic acetylcholine receptor plays a critical role in parasympathetic control of salivation in mice. J. Physiol. *558*, 561–575. https://doi.org/10.1113/jphysiol.2004.064626.

28. Muller, P.A., Schneeberger, M., Matheis, F., Wang, P., Kerner, Z., Ilanges, A., Pellegrino, K., Del Mármol, J., Castro, T.B.R., Furuichi, M., et al. (2020). Microbiota modulate sympathetic neurons via a gut-brain circuit. Nature *583*, 441–446. https://doi.org/10.1038/s41586-020-2474-7.

29. Bakovic, D., Pivac, N., Eterovic, D., Breskovic, T., Zubin, P., Obad, A., and Dujic, Z. (2013). The effects of low-dose epinephrine infusion on spleen size, central and hepatic circulation and circulating platelets. Clin. Physiol. Funct. Imaging *33*, 30–37. https://doi.org/10.1111/j.1475-097X.2012.01156.x.

30. Coton, E., Desmonts, M.H., Leroy, S., Coton, M., Jamet, E., Christieans, S., Donnio, P.Y., Lebert, I., and Talon, R. (2010). Biodiversity of coagulase-negative Staphylococci in French cheeses, dry fermented sausages, processing environments and clinical samples. Int. J. Food Microbiol. *137*, 221–229. https://doi.org/10.1016/j.ijfoodmicro.2009.11.023.

31. Camilleri, M. (2019). Leaky gut: mechanisms, measurement and clinical implications in humans. Gut *68*, 1516–1526. https://doi.org/10.1136/gutjnl-2019-318427.

32. Maltz, R.M., Marte-Ortiz, P., Rajasekera, T.A., Loman, B.R., Gur, T.L., and Bailey, M.T. (2022). Stressor-Induced Increases in Circulating, but Not Colonic, Cytokines Are Related to Anxiety-like Behavior and Hippocampal Inflammation in a Murine Colitis Model. Int. J. Mol. Sci. *23*, 2000. https://doi.org/10.3390/ijms23042000.

33. LeDoux, J.E. (1996). The Emotional Brain (Simon and Schuster).

34. LeDoux, J.E., Iwata, J., Cicchetti, P., and Reis, D.J. (1988). Different projections of the central amygdaloid nucleus mediate autonomic and behavioral correlates of conditioned fear. J. Neurosci. *8*, 2517–2529. https://doi.org/10.1523/JNEUROSCI.08-07-02517.1988.

35. Zhang, T., Perkins, M.H., Chang, H., Han, W., and de Araujo, I.E. (2022). An inter-organ neural circuit for appetite suppression. Cell *185*, 2478–2494.e28. https://doi.org/10.1016/j.cell.2022.05.007.

36. Diepenbroek, C., Quinn, D., Stephens, R., Zollinger, B., Anderson, S., Pan, A., and de Lartigue, G. (2017). Validation and characterization of a novel method for selective vagal deafferentation of the gut. Am. J. Physiol. Gastrointest. Liver Physiol. *313*, G342–G352. https://doi.org/10.1152/ajpgi.00095.2017.

37. Galley, J.D., and Bailey, M.T. (2014). Impact of stressor exposure on the interplay between commensal microbiota and host inflammation. Gut Microbes *5*, 390–396. https://doi.org/10.4161/gmic.28683.

38. Yang, D., Jacobson, A., Meerschaert, K.A., Sifakis, J.J., Wu, M., Chen, X., Yang, T., Zhou, Y., Anekal, P.V., Rucker, R.A., et al. (2022). Nociceptor neurons direct goblet cells via a CGRP-RAMP1 axis to drive mucus production and gut barrier protection. Cell *185*, 4190–4205.e25. https://doi.org/10.1016/j.cell.2022.09.024.

39. Zhang, W., Lyu, M., Bessman, N.J., Xie, Z., Arifuzzaman, M., Yano, H., Parkhurst, C.N., Chu, C., Zhou, L., Putzel, G.G., et al. (2022). Gut-innervating nociceptors regulate the intestinal microbiota to promote tissue protection. Cell *185*, 4170–4189.e20. https://doi.org/10.1016/j.cell.2022.09.008.

40. Schneider, K.M., Blank, N., Alvarez, Y., Thum, K., Lundgren, P., Litichevskiy, L., Sleeman, M., Bahnsen, K., Kim, J., Kardo, S., et al. (2023). The enteric nervous system relays psychological stress to intestinal inflammation. Cell *186*, 2823–2838.e20. https://doi.org/10.1016/j.cell.2023.05.001.

41. Ulluwishewa, D., Anderson, R.C., McNabb, W.C., Moughan, P.J., Wells, J.M., and Roy, N.C. (2011). Regulation of tight junction permeability by intestinal bacteria and dietary components. J. Nutr. *141*, 769–776. https://doi.org/10.3945/jn.110.135657.

42. Qin, D., Ma, Y., Wang, Y., Hou, X., and Yu, L. (2022). Contribution of Lactobacilli on Intestinal Mucosal Barrier and Diseases: Perspectives and Challenges of Lactobacillus casei. Life (Basel) *12*, 1910. https://doi.org/10.3390/life12111910.

43. Pavlov, V.A., and Tracey, K.J. (2012). The vagus nerve and the inflammatory reflex–linking immunity and metabolism. Nat. Rev. Endocrinol. *8*, 743–754. https://doi.org/10.1038/nrendo.2012.189.

44. Ji, H., Rabbi, M.F., Labis, B., Pavlov, V.A., Tracey, K.J., and Ghia, J.E. (2014). Central cholinergic activation of a vagus nerve-to-spleen circuit

alleviates experimental colitis. Mucosal Immunol. *7*, 335–347. https://doi.org/10.1038/mi.2013.52.

45. Mogilevski, T., Rosella, S., Aziz, Q., and Gibson, P.R. (2022). Transcutaneous vagal nerve stimulation protects against stress-induced intestinal barrier dysfunction in healthy adults. Neurogastroenterol. Motil. *34*, e14382. https://doi.org/10.1111/nmo.14382.
46. Costantini, T.W., Bansal, V., Krzyzaniak, M., Putnam, J.G., Peterson, C.Y., Loomis, W.H., Wolf, P., Baird, A., Eliceiri, B.P., and Coimbra, R. (2010). Vagal nerve stimulation protects against burn-induced intestinal injury through activation of enteric glia cells. Am. J. Physiol. Gastrointest. Liver Physiol. *299*, G1308–G1318. https://doi.org/10.1152/ajpgi.00156.2010.
47. Meregnani, J., Clarençon, D., Vivier, M., Peinnequin, A., Mouret, C., Sinniger, V., Picq, C., Job, A., Canini, F., Jacquier-Sarlin, M., et al. (2011). Anti-inflammatory effect of vagus nerve stimulation in a rat model of inflammatory bowel disease. Auton. Neurosci. *160*, 82–89. https://doi.org/10.1016/j.autneu.2010.10.007.
48. Ivy, A.C., and Oldberg, E. (1928). A hormone mechanism for gall-bladder contraction & evacuation. Am. J. Physiol. *86*, 599–613. https://doi.org/10.1152/ajplegacy.1928.86.3.599.
49. Han, W., Tellez, L.A., Perkins, M.H., Perez, I.O., Qu, T., Ferreira, J., Ferreira, T.L., Quinn, D., Liu, Z.W., Gao, X.B., et al. (2018). A Neural Circuit for Gut-Induced Reward. Cell *175*, 665–678.e23. https://doi.org/10.1016/j.cell.2018.08.049.
50. Cai, Y., Folkerts, J., Folkerts, G., Maurer, M., and Braber, S. (2020). Microbiota-dependent and -independent effects of dietary fibre on human health. Br. J. Pharmacol. *177*, 1363–1381. https://doi.org/10.1111/bph.14871.
51. Zou, J., Chassaing, B., Singh, V., Pellizzon, M., Ricci, M., Fythe, M.D., Kumar, M.V., and Gewirtz, A.T. (2018). Fiber-Mediated Nourishment of Gut Microbiota Protects against Diet-Induced Obesity by Restoring IL-22-Mediated Colonic Health. Cell Host Microbe *23*, 41–53.e4. https://doi.org/10.1016/j.chom.2017.11.003.
52. Bai, L., Mesgarzadeh, S., Ramesh, K.S., Huey, E.L., Liu, Y., Gray, L.A., Aitken, T.J., Chen, Y., Beutler, L.R., Ahn, J.S., et al. (2019). Genetic Identification of Vagal Sensory Neurons That Control Feeding. Cell *179*, 1129–1143.e23. https://doi.org/10.1016/j.cell.2019.10.031.
53. Chen, W.G., Schloesser, D., Arensdorf, A.M., Simmons, J.M., Cui, C., Valentino, R., Gnadt, J.W., Nielsen, L., Hillaire-Clarke, C.S., Spruance, V., et al. (2021). The Emerging Science of Interoception: Sensing, Integrating, Interpreting, and Regulating Signals within the Self. Trends Neurosci. *44*, 3–16. https://doi.org/10.1016/j.tins.2020.10.007.
54. Borgmann, D., Ciglieri, E., Biglari, N., Brandt, C., Cremer, A.L., Backes, H., Tittgemeyer, M., Wunderlich, F.T., Brüning, J.C., and Fenselau, H. (2021). Gut-brain communication by distinct sensory neurons differently controls feeding and glucose metabolism. Cell Metab. *33*, 1466–1482.e7. https://doi.org/10.1016/j.cmet.2021.05.002.
55. Tovote, P., Esposito, M.S., Botta, P., Chaudun, F., Fadok, J.P., Markovic, M., Wolff, S.B.E., Ramakrishnan, C., Fenno, L., Deisseroth, K., et al. (2016). Midbrain circuits for defensive behaviour. Nature *534*, 206–212. https://doi.org/10.1038/nature17996.
56. Swanson, L.W., and Petrovich, G.D. (1998). What is the amygdala? Trends Neurosci. *21*, 323–331. https://doi.org/10.1016/s0166-2236(98)01265-x.
57. Kalin, N.H., Shelton, S.E., and Davidson, R.J. (2004). The role of the central nucleus of the amygdala in mediating fear and anxiety in the primate. J. Neurosci. *24*, 5506–5515. https://doi.org/10.1523/JNEUROSCI.0292-04.2004.
58. Davis, M. (1992). The role of the amygdala in conditioned fear. In The Amygdala, J.P. Aggleton, ed. (Wiley-Liss), pp. 255–305.
59. Krieger, J.P., Asker, M., van der Velden, P., Börchers, S., Richard, J.E., Maric, I., Longo, F., Singh, A., de Lartigue, G., and Skibicka, K.P. (2022). Neural Pathway for Gut Feelings: Vagal Interoceptive Feedback From the Gastrointestinal Tract Is a Critical Modulator of Anxiety-like Behavior. Biol. Psychiatry *92*, 709–721. https://doi.org/10.1016/j.biopsych.2022.04.020.
60. Pnevmatikakis, E.A., and Giovannucci, A. (2017). NoRMCorre: An online algorithm for piecewise rigid motion correction of calcium imaging data. J. Neurosci. Methods *291*, 83–94. https://doi.org/10.1016/j.jneumeth.2017.07.031.
61. Young, M.D., and Behjati, S. (2020). SoupX removes ambient RNA contamination from droplet-based single-cell RNA sequencing data. Gigascience *9*, giaa151. https://doi.org/10.1093/gigascience/giaa151.
62. Krull, A., Buchholz, T.-O., and Jug, F. (2018). Noise2Void - Learning Denoising from Single Noisy Images. 2019 IEEE/CVF Conference on Computer Vision and Pattern Recognition (CVPR). https://doi.org/10.1109/CVPR.2019.00223.
63. Kirillov, A., Mintun, E., Ravi, N., Mao, H., Rolland, C., Gustafson, L., Xiao, T., Whitehead, S., Berg, A.C., Lo, W.-Y., et al. (2023). Segment Anything. 2023 IEEE/CVF International Conference on Computer Vision (ICCV). https://doi.org/10.1109/ICCV51070.2023.00371.
64. Han, W., and de Araujo, I.E. (2021). Dissection and surgical approaches to the mouse jugular-nodose ganglia. Star Protoc. *2*, 100474. https://doi.org/10.1016/j.xpro.2021.100474.
65. Paxinos, G., and Franklin, K. (2001). The Mouse Brain in Stereotaxic Coordinates, Second Edition (Academic Press).
66. Li, X., Zhang, G., Wu, J., Zhang, Y., Zhao, Z., Lin, X., Qiao, H., Xie, H., Wang, H., Fang, L., et al. (2021). Reinforcing neuron extraction and spike inference in calcium imaging using deep self-supervised denoising. Nat. Methods *18*, 1395–1400. https://doi.org/10.1038/s41592-021-01225-0.
67. Callahan, B.J., McMurdie, P.J., Rosen, M.J., Han, A.W., Johnson, A.J.A., and Holmes, S.P. (2016). DADA2: High-resolution sample inference from Illumina amplicon data. Nat. Methods *13*, 581–583. https://doi.org/10.1038/nmeth.3869.
68. Bolyen, E., Rideout, J.R., Dillon, M.R., Bokulich, N.A., Abnet, C.C., Al-Ghalith, G.A., Alexander, H., Alm, E.J., Arumugam, M., Asnicar, F., et al. (2019). Reproducible, interactive, scalable and extensible microbiome data science using QIIME 2. Nat. Biotechnol. *37*, 852–857. https://doi.org/10.1038/s41587-019-0209-9.
69. Segata, N., Izard, J., Waldron, L., Gevers, D., Miropolsky, L., Garrett, W.S., and Huttenhower, C. (2011). Metagenomic biomarker discovery and explanation. Genome Biol. *12*, R60. https://doi.org/10.1186/gb-2011-12-6-r60.
70. Pomeranz, L.E., Ekstrand, M.I., Latcha, K.N., Smith, G.A., Enquist, L.W., and Friedman, J.M. (2017). Gene Expression Profiling with Cre-Conditional Pseudorabies Virus Reveals a Subset of Midbrain Neurons That Participate in Reward Circuitry. J. Neurosci. *37*, 4128–4144. https://doi.org/10.1523/JNEUROSCI.3193-16.2017.
71. Dejea, C.M., Wick, E.C., Hechenbleikner, E.M., White, J.R., Mark Welch, J.L., Rossetti, B.J., Peterson, S.N., Snesrud, E.C., Borisy, G.G., Lazarev, M., et al. (2014). Microbiota organization is a distinct feature of proximal colorectal cancers. Proc. Natl. Acad. Sci. USA *111*, 18321–18326. https://doi.org/10.1073/pnas.1406199111.
72. Renier, N., Wu, Z., Simon, D.J., Yang, J., Ariel, P., and Tessier-Lavigne, M. (2014). iDISCO: a simple, rapid method to immunolabel large tissue samples for volume imaging. Cell *159*, 896–910. https://doi.org/10.1016/j.cell.2014.10.010.
73. Rahman, A.H., Tordesillas, L., and Berin, M.C. (2016). Heparin reduces nonspecific eosinophil staining artifacts in mass cytometry experiments. Cytometry A *89*, 601–607. https://doi.org/10.1002/cyto.a.22826.
74. Stern, A.D., Rahman, A.H., and Birtwistle, M.R. (2017). Cell size assays for mass cytometry. Cytometry A *91*, 14–24. https://doi.org/10.1002/cyto.a.23000.
75. Kirillov, A., Wu, Y., He, K., and Girshick, R. (2020). PointRend: Image Segmentation as Rendering. 2020 IEEE/CVF Conference on Computer Vision and Pattern Recognition (CVPR). https://doi.org/10.1109/CVPR42600.2020.00982.
76. Tervo, D.G.R., Hwang, B.Y., Viswanathan, S., Gaj, T., Lavzin, M., Ritola, K.D., Lindo, S., Michael, S., Kuleshova, E., Ojala, D., et al. (2016). A

Designer AAV Variant Permits Efficient Retrograde Access to Projection Neurons. Neuron *92*, 372–382. https://doi.org/10.1016/j.neuron.2016.09.021.

77. Kvitsiani, D., Ranade, S., Hangya, B., Taniguchi, H., Huang, J.Z., and Kepecs, A. (2013). Distinct behavioural and network correlates of two interneuron types in prefrontal cortex. Nature *498*, 363–366. https://doi.org/10.1038/nature12176.
78. Wolf, F.A., Angerer, P., and Theis, F.J. (2018). SCANPY: large-scale single-cell gene expression data analysis. Genome Biol. *19*, 15. https://doi.org/10.1186/s13059-017-1382-0.

STAR★METHODS

KEY RESOURCES TABLE

REAGENT or RESOURCE	SOURCE	IDENTIFIER
Antibodies		
Rabbit-anti-c-Fos	Abcam	Cat # ab190289; RRID: AB_2737414
Goat Anti-GFP antibody (FITC)	Abcam	Cat # ab6662; RRID: AB_305635
Alexa Fluor® 594 AffiniPure Donkey Anti-Rabbit IgG	Jackson Immuno Research Labs	Cat # 711-585-152; RRID:AB_2340621
TRITC-conjugated affinipure Goat anti-Rabbit IgG (H+L)	Jackson Immuno Research Labs	Cat # 111-025-144; RRID: AB_2337932
FITC-conjugated affinipure goat anti-rabbit IgG (H+L)	Jackson Immuno Research Labs	Cat # 111-095-144; RRID: AB_2337978
FITC-conjugated affinipure Donkey Anti-Goat IgG (H+L)	Jackson Immuno Research Labs	Cat # 705-095-147; RRID: AB_2340401
TRITC-conjugated affinipure Donkey Anti-Goat IgG (H+L)	Jackson Immuno Research Labs	Cat # 705-025-147; RRID: AB_2340389
Goat Anti-Rabbit IgG Antibody (H+L), DyLight™ 649	Vector Laboratories	SKU # DI-1649-1.5; RRID: AB_3065224
Alexa647-conjugated anti-mouse IgD antibody	Biolegend	Cat. # 405707; RRID:AB_893528
Brilliant Violet 421-conjuncted anti-mouse CD21/CD35 antibody	Biolegend	Cat. # 123421; RRID:AB_2650891
Alexa488-conjuncted anti-mouse/human Ki-67 antibody	Biolegend	Cat # 151204; RRID:AB_2566800
Anti-Mouse CD45 (30-F11)-89Y	Standard BioTools	Cat # 3089005B; RRID:AB_2651152
Anti-Mouse CD90.2 (30-H12)-113In#	Biolegend	Cat # 105333; RRID:AB_2563765
Anti-Mouse Ly-6G (1A8)-141Pr	Standard BioTools	Cat # 3141008B; RRID:AB_2814678
Anti-Mouse CD11c (N418)-142Nd#	Biolegend	Cat # 117341; RRID:AB_2562807
Anti-Mouse TCRb (H57-597)-143Nd	Standard BioTools	Cat # 3143010B
Anti-Mouse CD24 (M1/69)-144Nd#	Biolegend	Cat # 101829; RRID:AB_2563732
Anti-Mouse F4/80 (BM8)-146Nd	Standard BioTools	Cat # 3146008B; RRID:AB_2895117
Anti-Mouse CD11b (M1/70)-148Nd	Standard BioTools	Cat # 3148003B; RRID:AB_2814738
Anti-Mouse CD19 (6D5)-149Sm	Standard BioTools	Cat # 3149002B; RRID:AB_2814679
Anti-Mouse IgD (11-26c.2a)-150Nd#	Biolegend	Cat # 405737; RRID:AB_2563774
Anti-Mouse CD25 (3C7)-151Eu	Standard BioTools	Cat # 3151007B; RRID:AB_2827880
Anti-Mouse SiglecF (S17007L)-163Dy#	Biolegend	Cat # 155502; RRID:AB_2810420
Anti-Mouse CD335 (NKp46) (29A1.4)-153Eu#	Biolegend	Cat # 137625; RRID:AB_2563744
Anti-Mouse CD64 (X54-5/7.1)-156Gd#	Biolegend	Cat # 139301; RRID:AB_10613107
Anti-Mouse CD117 (2B8)-166Er#	Biolegend	Cat # 105829; RRID:AB_2563710
Anti-Mouse CD62L (MEL-14)-160Gd	Standard BioTools	Cat # 3160008B
Anti-Mouse CD103 (2E7)-161Dy#	Biolegend	Cat # 121401; RRID:AB_535944
Anti-Mouse Ly-6C (HK1.4)-162Dy	Standard BioTools	Cat # 3162014B; RRID:AB_2922921
Anti-Mouse CD8a (53-6.7)-168Er	Standard BioTools	Cat # 3168003B; RRID:AB_2811241
Anti-Mouse CD206/MMR (C068C2)-169Tm	Standard BioTools	Cat # 3169021B; RRID:AB_2832249
Anti-Mouse NK1.1 (PK136)-170Er	Standard BioTools	Cat # 3170002B; RRID:AB_2885023
Anti-Mouse CD44 (IM7)-171Yb#	Biolegend	Cat # 103051; RRID:AB_2562799
Anti-Mouse CD4 (RM4-5)-172Yb	Standard BioTools	Cat # 3172003B; RRID:AB_2811242
Anti-Mouse MHCII (I-A/I-E) (M5/114.15.2)-Bi209#	Biolegend	Cat # 107602; RRID:AB_313317
Anti-Human/Mouse CD45R/B220 (RA3-6B2)-176Yb	Standard BioTools	Cat # 3176002B; RRID:AB_2895123
TruStain FcX™ (anti-mouse CD16/32) Antibody	Biolegend	Cat # 101319; RRID:AB_1574975
PE-conjugated anti-mouse IL-1a	Biolegend	Cat # 503203; RRID: AB_315281
PE-conjugated anti-mouse CXCL9 (MIG)	Biolegend	Cat # 515603; RRID: AB_2245490
Goat-anti-ChAT antibody	Millipore	Cat #AB144; RRID: AB_90650
Rabbit polyclonal to beta III Tubulin	Abcam	Cat# ab18207; RRID:AB_444319
Chemicals, peptides, and recombinant proteins		
CCK-SAP	Advanced Targeting Systems	Cat # IT-31

(*Continued on next page*)

Continued

REAGENT or RESOURCE	SOURCE	IDENTIFIER
Blank-SAP	Advanced Targeting Systems	Cat # IT-21
Anti-ChAT-SAP	Advanced Targeting Systems	Cat # KIT-42
IgG-SAP	Advanced Targeting Systems	Cat # KIT-42
CCK8	AnaSpec	Cat # AS-20739
Diphtheria Toxin	Sigma-Aldrich (Merck)	Cat # D0564-1MG
FITC-dextran	Chondrex	Cat # 4013
Sucralose	Sigma-Aldrich (Merck)	Cat # 69293-100G
Clozapine N-oxide (CNO)	Enzo Life Sciences	Cat # BML-NS105-0025
Krebs-Henseleit Buffer Modified	Sigma-Aldrich (Merck)	Cat # K3753-10L
RNAscope® Probe Mm-Glp1r	ACDBio	Cat # 418851
RNAscope® Probe Mm-Cckar-C2	ACDBio	Cat # 313751-C2
RNAscope® Probe Mm-Chrm3-C3	ACDBio	Cat # 437701-C3
2.5 duplex mouse positive control probe	ACDBio	Cat # 321651
2-plex negative control probe	ACDBio	Cat # 320751
Vancomycin	Sigma-Aldrich (Merck)	Cat # 1709007
Metronidazole	Sigma-Aldrich (Merck)	Cat # 1442009-100MG
Ampicillin	Sigma-Aldrich (Merck)	Cat # PHR2838
Neomycin	Sigma-Aldrich (Merck)	Cat # 1458009-200MG
Carbenicillin disodium	Fisher Scientific	Cat # AC455360010
Chloramphenicol	Sigma-Aldrich (Merck)	Cat # C0378-25G
Urethane	Sigma-Aldrich (Merck)	Cat # U2500-100G
Darifenacin hydrobromide	Sigma-Aldrich (Merck)	Cat # 1164200
Dichloromethane	Sigma-Aldrich (Merck)	Cat # 270997
Hydrogen peroxide solution	Sigma-Aldrich (Merck)	Cat # H1009
Methanol	Sigma-Aldrich (Merck)	Cat # 34860
Dibenzyl ether	Sigma-Aldrich (Merck)	Cat # 33630
FluoroGold (FG)	Manufacturer: Fluorochrome Inc; Purchased from Fisher scientific	Cat# NC0560981
Critical commercial assays		
VECTASTAIN Elite ABC HRP Kit (Peroxidase, Standard)	Vector Laboratories	Cat# PK-6100
RNAscope Multiplex Fluorescent Reagent Kit v2	ACDBio	CAT # 323110
H&E Staining Kit (Hematoxylin and Eosin)	Abcam	Cat # ab245880
Periodic Acid Schiff (PAS) Stain Kit (Mucin Stain)	Abcam	Cat # ab150680
Olink® Target 96 Mouse Exploratory	Olink	https://olink.com/products-services/target/biological-process/
Experimental models: Organisms/strains		
Mouse: C57BL/6J (B6)	The Jackson Laboratory	JAX: 000664
Mouse: *Glp1r*$^{tm1.1(cre)Lbrl}$/RcngJ (Glp1r-ires-Cre)	The Jackson Laboratory	JAX: 029283
Mouse: C57BL/6-*Gt(ROSA)26Sor*$^{tm1(HBEGF)Awai}$/J (B6-iDTR)	The Jackson Laboratory	JAX: 007900
Mouse: B6.129S-*Chat*$^{tm1(cre)Lowl}$/MwarJ (B6J.ChAT-ires-Cre::Δneo)	The Jackson Laboratory	JAX: 031661
Mouse: B6.Cg-*Gt(ROSA)26Sor*$^{tm9(CAG-tdTomato)Hze}$/J (Ai9)	The Jackson Laboratory	JAX: 007909
Mouse: B6.Cg-*Igs7*$^{tm148.1(tetO-GCaMP6f,CAG-tTA2)Hze}$/J (Ai148D)	The Jackson Laboratory	JAX: 030328
Mouse: B6;129-*Gt(ROSA)26Sor*$^{tm5(CAG-Sun1/sfGFP)Nat}$/J (CAG-Sun1/sfGFP)	The Jackson Laboratory	JAX: 021039
C57BL/6J-Gt(ROSA)26Sor$^{em1(CAG-Cd63/EmGFP)Adly}$/J (CD63-emGFP$^{l/s/l}$)	The Jackson Laboratory	JAX: 036865

(*Continued on next page*)

Continued

REAGENT or RESOURCE	SOURCE	IDENTIFIER
Mouse: Cckar$^{em1(cre)Shah}$/J	The Jackson Laboratory	Jax: 037017
Mouse: B6J.ChAT-ires-Cre::Δneo	The Jackson Laboratory	Jax: 031661
Mouse: B6.Cg-Tg(Chat-COP4*H134R/EYFP,Slc18a3)6Gfng/J (ChAT-ChR2-EYFP)	The Jackson Laboratory	Jax: 014546
Bacterial and virus strains		
AAV1 hSyn FLEx mGFP-2A-Synaptophysin-mRuby	Dr. Luo-Addgene AAV Viral Service	Addgene Viral Prep: 71760-AAV1
AAV8.2-hEF1a-DIO-synaptophysin-EYFP	Viral Gene Transfer Core, McGovern Institute for Brain Research, Massachusetts Institute of Technology	N.A.
AAV-DJ-hSyn-DIO-EGFP	Dr. Roth - Duke Viral Vector Core	Addgene Plasmids: 50457
AAV5-hSyn-hM3D(Gq)-mCherry	Addgene	Addgene Plasmids: 50474
AAV1-flex-taCasp3-TEVp	Dr. Shah - University of North Carolina's Vector Core	Addgene Plasmids: 45580
AAV9-hSyn-DIO-hM3D(Gq)-mCherry	Addgene	Addgene Plasmids: 44361
AAV5-hSyn-hM4D(Gi)-mCherry	Addgene	Addgene Plasmids: 50475
PRV CMV-EGFP	NIH Center for Neuroanatomy with Neurotropic Virus	# 152
PRV CAG-DIO-TK-GFP	NIH Center for Neuroanatomy with Neurotropic Virus	Ba-2017
E. coli EcAZ-2	Gift from Dr. Amir Zarrinpar	EcAZ-2
Staphylococcus xylosus	ATCC	ATCC 29971
Lactobacillus rhamnosus	ATCC	ATCC 27773
12 strains probiotics[Lac+Bif]	RenewLife Extra care probiotic 50 billion live cultures	Lacto Probiotic: *Lactobacillus plantarum* Lp-115®; *Lactobacillus rhamnosus* GG; *Lactobacillus acidophilus* NCFM®; *Lactococcus lactis* LI-23 ™; *Lactobacillus casei* Lc-11®; *Lactobacillus paracasei* Lpc-37®; *Lactobacillus acidophilus* La-14®; *Lactobacillus brevis* Lbr-35 ™; Bifido probiotic: *Bifidobacterium lactis* BI-04®; *Bifidobacterium lactis* HN019™; *Bifidobacterium lactis* Bi-07®; *Bifidobacterium infantis* Bi-26 ™.
Deposited data		
Raw 16S sequencing	BioProject	PRJNA1126813
Behavioral, electrophysiological, graphs, and analyzed intravital imaging raw data	Mendeley Data	DOI: 10.17632/pw7y7wtsg2.2
Software and algorithms		
Igor Pro 6.36	WaveMetrics	https://www.wavemetrics.com/
EthoVision XT 11.5	Noldus	http://www.noldus.com/animal-behavior-research/products/ethovision-xt
LabView 2014	LabView	http://www.ni.com/download/labview-development-system-2014/4735/en/

(*Continued on next page*)

Continued

REAGENT or RESOURCE	SOURCE	IDENTIFIER
GraphPad Prism 9	GraphPad	http://www.graphpad.com/scientific-software/prism/
Adobe design standard CS6	Adobe	http://shop.adobe.com/
IBM SPSS statistics 24.0	IBM Predictive Software	https://www.ibm.com/docs/en/spss-statistics
Win Movie Maker	VideoWinSoft Software	http://www.VideoWinSoft.com
ImageJ	NIH	https://imagej.nih.gov/ij/
Fiji ImageJ	Fiji	https://imagej.net/software/fiji/
Python 3	Python Software Foundation.	https://www.python.org/
OpenCV 4.5.3	OpenCV team	https://opencv.org/
Ffmpeg n4.4	FFmpeg team	https://www.ffmpeg.org/
NoRMCorre: Non-Rigid Motion Correction	Pnevmatikakis and Giovannucci[60]	https://github.com/flatironinstitute/NoRMCorre
Cell Ranger (v. 7.1.0)	10x Genomics	https://support.10xgenomics.com/single-cell-gene-expression/software/pipelines/latest/installation
SoupX (v. 1.6.1)	Young and Behjati[61]	https://github.com/constantAmateur/SoupX
Scrublet	PMID: 30954476	https://github.com/swolock/scrublet
Scanpy (v. 1.9.1)	PMID: 29409532	https://github.com/scverse/scanpy
Cytoscape (v. 3.10.1)	PMID: 14597658	https://cytoscape.org/
segment-anything	Krull et al.[62] and Kirillov et al.[63]	https://github.com/facebookresearch/segment-anything
Cellpose (v. 2.2.2)	PMID: 33318659	https://github.com/MouseLand/cellpose
PyTorch (v. 2.1.0)	Facebook	https://pytorch.org/
Seaborn (v. 0.11.2)	GitHub	https://github.com/mwaskom/seaborn
Tensorflow (v. 2.9.0)	Google	https://www.tensorflow.org/
N2V	Citation: Krull et al.[62]	https://github.com/juglab/n2v
Other		
Cell-ID™ Intercalator-Rh (500 μM)	Standard BioTools	Cat # 201103A
Cell-ID™ 20-Plex Pd Barcoding Kit	Standard BioTools	Cat # 201060
Cellaca MX High-throughput Automated Cell Counter	Nexcelom	https://www.nexcelom.com/nexcelom-products/cellaca-3/
Homeothermic Monitoring System	Harvard Apparatus	Cat # 55-7020
Tungsten 2 Channel Electrode (B Twisted Wire)	Protech International	MS303T/3-B/SPC
Sl2c/sb 2 channel commutator, single brush	Protech International	SL2C/SB
305-bnc 5cm - 100cm w/mesh x62(cm) connection wires	Protech International	305-BNC-WM
Nanofil Application Kits (Microinjection)	World Precision Instruments	Cat # Beveled (IO-KIT)
NanoFil Needles (Microinjection)	World Precision Instruments	Cat # Beveled, 36G (NF36BV-2)
Pump 11 Elite Nanomite (Microinjection)	Harvard Apparatus	Cat # 70-4507
Spinal Cord Hook (Vagal operation)	Fine Science Tools	Cat # 10162-12
Mouse Spinal Adaptor (Spinal operation)	Stoelting	Cat # 51690
Mouse Transverse Clamps (Spinal operation)	Stoelting	Cat # 51691
Delicate Suture Tying Forceps (Microsurgery)	Fine Science Tools	Cat # 11063-07
Formvar-Insulated Nichrome Wires (EMG recording)	A-M system	Cat # 761000
Microwire connections (EMG recording)	Neuralynx	Cat # EIB-16
16 tungsten microwires, 35-μm diameter (Electrophysiological recordings)	TDT systems	Cat # OMN1005
Masterflex® Nylon, Female Luer (Fistula)	Cole-Parmer	Cat # UX-45502-20

(*Continued on next page*)

Continued

REAGENT or RESOURCE	SOURCE	IDENTIFIER
Masterflex®, Polypropylene, Male Luer Lock (Fistula)	Cole-Parmer	Cat # EW-30800-30
Round Cover Slip German Glass #1.5, 15 mm (Intravital microscopy)	Electron Microscopy Sciences	Cat # 64-0713
Ultra Gel Control Super Glue (Intravital window)	Loctite	Cat # 45208
Stainless steel large penny fender washers M12x24x1.5mm (Intravital microscopy)	Dywishkey	Cat # 304
Low Toxicity Silicone Adhesive (Intravital microscopy)	WPI	Cat # KWIK-SIL
FluoroDish Cell Culture Dish 50mm	WPI	Cat # FD5040-100
Catheter for mouse jugular vein, 1 to 3Fr, 10.5cm, collar @1.2cm. Fits 22ga. (Gastric balloon)	Instech laboratories	Cat # C10PU-MJV1403
MicroRenathane tubing (OD 0.025") (Ileo catheterization)	Braintree Scientific	Cat # MRE025
Patch Clamp Amplifier	Molecular Devices	Cat # Multiclamp 700B
Confocal microscope	Leica	TCS SP8 STED 3X
Confocal microscope	Zeiss	LSM980 Airyscan 2
Single Unit Recording Amp	TDT	RZ5
Digitizer and Sequencer	CED	Micro 1401
LED for slice illumination	Mightex	LCS-0470-50-22
Miltenyi Tyto microfluidic sorter	Miltenyi Biotec	Cat # 130-103-931
Behavioral, electrophysiological, anatomy, and analyzed intravital imaging rare data	Mendeley Data.com	https://doi.org/10.17632/zkjm36wp8s.1
Vevo 2100 Micro-Imaging System for small animals	FUJIFILM VisualSonics	Vevo 2100
Rodent Diet With 10 kcal% Fat (Matching Sucrose to D12451)	Research Diets	D12450H
Rodent Diet With 45 kcal% Fat	Research Diets	D12451
Rodent Diet With 45 kcal% Fat (fiber free)	Research Diets	D13121101
Diet With High Fiber (Cellulose)	Research Diets	D22072013
Rodent Diet With 10 kcal% Fat	Research Diets	D12450B
Rodent Diet With high protein concentration	Research Diets	D17120803
Probiotics with 50 billion live cultures	RenewLife orderd from Amazon	Cat. # 1148061
OneTouch Ultra Test Strips for Diabetes	One Touch	https://shop.onetouch.com/onetouch-test-strips
One Touch Ultra 2 Blood Glucose Monitoring System	One Touch	https://www.onetouch.com/products/glucose-meters/onetouch-ultra2
MRS Agar	Sigma-Aldrich (Merck)	Cat # 41782-500G-F
LB agar kan50	Fisher Scientific	Cat # 50842594
Brain heart infusion broth	Fisher Scientific	Cat. # CM1135B
Mitsubishi pouch-anaero 20/pk	Fisher Scientific	Cat # 23246379
Agar, granulated 500g	Fisher Scientific	Cat # BP9744500
Flexible Plastic Tubing Oral Gavage Needles (Box of 20)	GavageNeedle	SKU# PDAFN2030NB
16-channel movable electrophysiological recording bundles	Innovative Neurophysiology	Specs: 16-channel single drive movable bundles, 23-um tungsten electrodes, 4.5-mm cannula length, 4-mm moving distance, with ground wire. Omnetics A79014-001 connectors.
Implantable Optical Fibers	Doric Lenses, Canada	MFC_200/240-0.22_6mm_ZF1.25(G)_FLT
Low Toxicity Silicone Adhesive (Intravital microscopy)	WPI	Cat # KWIK-SIL
Single Unit Recording Amp	TDT	RZ5

#All the antibodies labeled for CyTOF analysis were conjunct by Human Immune Monitoring Center at Mount Sinai

RESOURCE AVAILABILITY

Lead contact

Further information and requests for resources and reagents should be directed to and will be fulfilled by the lead contact, Ivan E de Araujo (Ivan.DeAraujo@tuebingen.mpg.de) and by technical contacts Hao Chang (hao.chang@mssm.edu) and Wenfei Han (wenfei.han@tuebingen.mpg.de).

Materials availability

This study did not generate new unique reagents.

Data and code availability

- Behavioral, electrophysiological, anatomical, and post-processed intravital imaging data have been deposited at *Mendeley Data* and are publicly available as of the date of publication. DOIs are listed in the key resources table. The accession number for the 16S sequencing data reported in this paper is Bioproject: PRJNA1126813. All the sequencing data are publicly available as of the date of publication.
- This paper did not generate any original code.
- Any additional information needed for reanalyzing the datasets reported in this article will be made available by the technical contacts upon request.

EXPERIMENTAL MODEL AND STUDY PARTICIPANT DETAILS

All experiments presented in this study were conducted according to the animal research guidelines from NIH and were approved by the Institutional Animal Care and Use Committee of Icahn School of Medicine at Mount Sinai.

Experimental Animals

A total of 1078 adult male mice were used. Strain details and number of animals are as follows:

427 C57BL/6J (Jax Mouse Strain #000664).
15 Glp1r-ires-Cre (Jax Mouse Strain #029283).
43 Glp1r-ires-Cre x Ai148D (Jax Mouse Strain #029283 and #030328).
10 Glp1r-ires-Cre x CD63-emGFP$^{l/s/l}$ (Jax Mouse Strain #029283 and # 036865).
3 Glp1r-ires-Cre x Ai148D x Ai9 (Jax Mouse Strain #029283 and #030328 and #007907).
453 Glp1r-ires-Cre x ROSA26iDTR (Jax Mouse Strain #029283 and #007900).
36 Glp1r-ires-Cre x Ai148D x ROSA26iDTR (Jax Mouse Strain #029283 and #030328 and #007900).
3 Ai9 x Glp1r-ires-Cre (Jax Mouse Strain #007914 and #029283).
5 Glp1r-ires-Cre x CAG-Sun1/sfGFP (Jax Mouse Strain #029283 and #021039).
75 B6J.ChAT-ires-Cre::Δneo (Jax Mouse Strain #031661).
3 Cckar^{Cre} x Ai9 (Jax Mouse Strain #037017 and #007909).
5 ChAT-ChR2-EYFP line 6 (Jax Mouse Strain #014546).

All mice used in behavioral experiments were individually housed under a 12-hour light/dark cycle. At the time of the behavioral experiments, animals were 8–20 weeks old and weighted approximately 25-28 grams. All animals were used in scientific experiments for the first time. This includes no previous exposure to pharmacological substances or alternative diets. Health status was normal for all animals. Animals used for anatomical tracing studies were group housed and 3 weeks old at the time of injection. Please see details on surgical procedure in Table S1

METHOD DETAILS

The following provides details on viral and drug injections, catheterizations, denervation, brain electrode implantation, and intravital imaging preparations for each mouse strain (Also see key resources table). All surgeries were performed in a Biosafety Level 2-approved laboratory. All mice including surgical mice were housed at the Mount Sinai specific-pathogen-free (SPF) Animal Facility. The surgical mice were monitored daily for body weight and food intake. In all cases, preoperative analgesia: 0.05 mg/Kg Buprenorphine (*s.c.*); anesthesia induced by 3% isoflurane and maintained by 1.5% ∼2% isoflurane; postoperative analgesia: 0.05mg/Kg Buprenorphine (s.c.) twice a day for three consecutive days. The surgical areas were shaved and cleaned with iodine soap and wiped with 70% isopropyl alcohol. All incisions were thoroughly disinfected with a layer of Baytril ointment. All surgeries were performed under stereomicroscopes, with animals placed on a heated pad (CMA 450; Harvard Apparatus, Holliston, MA). After surgery, animals were allowed to recover under infrared heat until they chose to reside in the unheated side of the cage.

Lesions of the glands of Brunner

Surgical resection of Brunner' glands (BG-resected)

The abdomen of an 8-hour food-restricted animal was shaved and cleaned. A midline incision was made into the abdomen. The stomach was exteriorized through the midline incision, and the pyloric antrum was loosely stitched to the left rectus abdominis to maximize the view of the proximal duodenum. Wet surgical gauze was applied to isolate the duodenum and the duodenum bulb held with cotton tips. The scalpel tip was carefully manipulated to avoid the mesenteric blood vessels. A longitudinal incision was made on the ventral side of the duodenum bulb (to the distal direction, 5mm from the duodenum-pyloric sphincter junction). The lumen was opened with fine tweezers, and the lumen contents gently flushed with saline. The submucosal tissue underneath the pyloric sphincter was resected with an electric cauterizer. The duodenal incision was sutured with an 8-0 absorbable vicryl suture (Ethicon V548G, USA), the loose suture attached to the stomach removed, and the rectus abdominis/skin incisions were closed with sterile sutures.

Duodenum resection (Duo-lesion)

This is a control procedure for the Brunner's gland resection described above. The mouse duodenum was exposed as described above. The descending part of the duodenum (approximately at the location of the sphincter of Oddi) was held with cotton tips. The scalpel tip was carefully manipulated to avoid mesenteric blood vessels. A longitudinal incision was made on the ventral side of the duodenum (~5mm long and at least 10mm distal to the duodenal-pyloric junction, thereby avoiding the glands of Brunner). The lumen was opened with fine tweezers and slightly flushed with saline. The submucosal tissue underneath the pyloric sphincter was resected with the electric cauterizer. The duodenal incision was sutured with an 8-0 absorbable vicryl suture (Ethicon V548G, USA), the loose suture attached to the stomach removed, and the rectus abdominis/skin incisions were closed with sterile sutures.

Sham surgery (negative control)

The mouse duodenum bulb was exposed, and a ~5mm longitudinal incision was cut as described above. The duodenal incision was sutured with an 8-0 absorbable vicryl suture (Ethicon V548G, USA), the loose suture attached to the stomach removed, and the rectus abdominis/skin incisions were closed with sterile sutures.

Brunner DTx / Saline injection (BG-DTx and BG-saline)

The abdomen of an 8-hour food-restricted animal was shaved and cleaned. A midline incision was made into the abdomen. The stomach was exteriorized through the midline incision, and the pyloric antrum was loosely stitched to the left rectus abdominis to maximize the view of proximal duodenum. 0.2mg/mL diphtheria toxin (Sigma D0564), or saline, was loaded into a Nanofil™ 36G beveled needle (WPI, Sarasota, FL) and Nanofil™ tubing (WPI, Sarasota, FL) was connected to a Nanofil™ 10μl syringe (WPI, Sarasota, FL) mounted on a Pump 11 Elite Nanomite (Harvard Apparatus, Holliston, MA). Eight 25nL injections (total volume of 200 nL) were made at 10nL/s into evenly distributed punctures targeting the submucosal layer of the duodenum bulb (within 3 mm approximate to the pyloric sphincter). The needle tip was carefully manipulated to avoid mesenteric blood vessels. After the infusions were completed, the needle was left in place for 5s before extraction to ensure complete absorption. After removing the loose suture attached to the stomach, sterile sutures were then applied to the skin.

Anti-ChAT-SAP and Rabbit IgG-SAP injection for Brunner's glands cholinergic denervation

Same procedure as injections into Brunner's glands above except that mice were injected with 200nL Anti-ChAT-SAP or Rabbit IgG-SAP (Cat. #KIT-42, Advanced Targeting Systems, USA).

Duodenum DTx injection in myenteric layer (Duo-DTx)

This is a control procedure for the Brunner's gland ablation described above. The duodenal bulb was exposed as described above. 0.2mg/mL diphtheria toxin (Sigma D0564), or saline, was loaded into a Nanofil™ 36G beveled needle (WPI, Sarasota, FL), and Nanofil™ tubing (WPI, Sarasota, FL) connected to a Nanofil™ 10μl syringe (WPI, Sarasota, FL) and mounted on a Pump 11 Elite Nanomite (Harvard Apparatus, Holliston, MA). Eight 25nL injections (total volume of 200 nL) were made at 10nL/s into evenly distributed punctures targeting the myenteric layer of the duodenum 10mm below the bulb. The needle tip was carefully manipulated to avoid mesenteric blood vessels. After the infusions were completed, the needle was left in place for 5s before extraction to ensure complete absorption. After removing the loose suture attached to the stomach, sterile sutures were then applied to the skin.

Vagal, Splenic Nerve, and sympathetic ganglia lesions

Nodose CCK-SAP lesion

Mice injected with unconjugated saporin (Blank-SAP) or cholecystokinin-conjugated saporin (CCK-SAP) were 3 weeks old at the time of surgery. Nodose ganglia injections were performed as described previously.[64] Briefly, a ventral midline incision was made along the length of the neck; submandibular glands were retracted along with sternohyoid and omohyoid muscles to expose the trachea and the carotid artery. The vagus nerve was separated from the carotid artery with the Spinal Cord Hook (FST, Foster City, CA) until the nodose ganglion became visibly accessible. Viral or chemical aliquots were loaded into a Nanofil™ 36G beveled needle (WPI, Sarasota, FL) and Silflex™ tubing (WPI, Sarasota, FL). For each nodose ganglion, a total of 500nL volume of Blank-SAP or CCK-SAP was delivered at 50nL/min using a Nanofil™ 10μl syringe (WPI, Sarasota, FL) mounted on a Pump 11 Elite Nanomite (Harvard Apparatus, Holliston, MA). Sterile suture was then applied to the skin.

Subdiaphragmatic vagotomy

3-week-old animals were 8-hour food restricted before the surgery. The abdomen was shaved and cleaned. A midline incision was made into the abdomen. The liver and stomach were retracted aside to expose the esophagus. The branches of the vagus nerves

innervating the stomach were carefully separated from both the esophagus and the left gastric artery, and bilaterally severed with an electrical cauterizer. Sterile suture was then applied to muscle and skin.

Splenectomies

Animals at the time of splenectomies were 3 weeks old. The abdomen was shaved and cleaned. A midline incision was made into the abdomen. The stomach was exteriorized through a midline incision. The stomach fundus was pulled towards the liver to expose the celiac and superior mesenteric ganglia attached respectively to the celiac and superior mesenteric arteries. The greater, lesser, and least splanchnic nerves carrying the 5th through 11th thoracic sensory and sympathetic innervations were identified, carefully separated away from the celiac artery and aorta, and dissected with miniature forceps and spring scissors (FST, Foster City, CA). Sterile sutures were then applied to the skin.

Celiactomy

Animals at the time of celiactomy were 3-week-old. The abdomen was shaved and cleaned. A midline incision was made into the abdomen. The stomach was exteriorized through the midline incision. The stomach fundus was pulled towards the liver to expose the celiac ganglion. The celiac ganglion was carefully separated away from the celiac artery with a miniature forceps (FST, Foster City, CA). The base of the celiac ganglion was ligated before resection. Sterile suture was then applied to skin.

Brain stereotactic surgeries

Stereotaxic viral injection and probe implantation

Animals at the time of surgery were 6-week-old. Injections were performed with a Hamilton 1.0μL Neuros Model 7001KH syringe, at a rate of 20nL/min. In what follows, and for each mouse strain, we first list the viral construct injected or device implanted, then the relevant stereotaxic coordinates are described. Stereotaxic coordinates are shown with respect to *bregma*, according to a standardized atlas of the mouse brain.[65]

Mouse strain **ChAT-ires-Cre**
Injection Location *DMV*
Viral construct AAV1 hSyn FLEx mGFP-2A-Synaptophysin-mRuby (300nL bilateral), AAV8.2-hEF1a-DIO-synaptophysin-EYFP (300nL bilateral), AAV1-flex-taCasp3-TEVp (300nL bilateral), AAV9-hSyn-DIO-hM3D(Gq)-mCherry (300nL bilateral), Or AAV9-Ef1a-DIO EYFP (300nL each, bilateral).
Coordinates: AP: -7.5mm, ML: ±0.3mm, DV: -5.5 ∼-5.3mm.
Mouse strain **Glp1r-ires-Cre x Ai148D.**
Injection Location *CeM.*
Viral construct AAV5-hSyn-hM3D(Gq)-mCherry (300nL each, bilateral).
Injection Coordinates: AP: -1.0mm, ML: ±2.5mm, DV: -4.8mm ∼-5.2mm.
Mouse strain **B6.**
Injection Location *CeM.*
Viral construct AAV5-hSyn-hM3D(Gq)-mCherry (300nL each, bilateral) Or AAV5-hSyn-hM4D(Gi)-mCherry (300nL each, bilateral).
Injection Coordinates: AP: -1.0mm, ML: ±2.5mm, DV: -4.8mm ∼-5.2mm. 0.3μL/side.
Mouse strain **Cckar^{Cre} x Ai9.**
Injection Location *CeM.*
Viral construct PRV-152-CMV-EGFP.
Injection Coordinates: AP: -1.0mm, ML: ±2.5mm, DV: -4.8mm ∼-5.2mm. 0.1μL right side.
Mouse strain **Glp1r-ires-Cre x Ai148D.**
Implant Location *CeM.*
Stereotaxic electrode implantation.
Electrode type: B-twisted wire 2-channel electrode (Protech international).
Electrode Coordinates: AP: -1.0mm, ML: ±2.5mm, DV: -5.0mm.
Mouse strain **B6.**
Implant Location *CeM.*
Stereotaxic electrode implantation.
Electrode type: B twisted wire 2-channel electrode (Protech international).
Electrode Coordinates: AP: -1.0mm, ML: ±2.5mm, DV: -5.0mm.

In vivo electrophysiological recordings with opto-tagging

For array implantation, after intraperitoneal (i.p.) catheterization (as detailed below), ChAT-ChR2-EYFP mice were placed on the stereotaxic apparatus, and one electrode containing a 16-channel movable bundle (23 μm tungsten, Innovative Neurophysiology, Inc. USA) attached to an angle-tipped optic fiber (Doric lenses) was implanted onto DMV (AP: -7.5mm, ML: ±0.3mm, DV: -5.4mm). The implanted bundle was left in target location for 30 mins before switching anesthesia to urethane 1.0-1.5 g/kg and initiating neuronal recordings. The locations of electrodes were confirmed histologically. Recordings were performed using the spike modules of the multichannel acquisition processor (Tucker-Davis Technologies). After a 12 minutes-long baseline and saline i.p. period, 0.1mL of 10μg/Kg CCK8 was infused via the i.p. catheter at 0.1mL/min and recording last for 12 minutes. At the end of the recording session,

473-nm blue stimulation was delivered at 1Hz, 0.5s on/0.5s off cycles to identify which isolated units DMV ChAT+ (cholinergic parasympathetic) neurons. To prevent photo-electric artifacts, light intensity was minimized and tests performed at multiple sites.

In vivo electrophysiological recordings during exposure to stressor

For array implantation, C57BL6/J mice were placed on the stereotaxic apparatus, and one electrode containing 16-channel movable bundles (23 μm tungsten, Innovative Neurophysiology, Inc. USA) was implanted onto CeM (AP: -1.0mm, ML: ±2.5mm, DV: -4.3mm). The locations of electrodes were confirmed histologically. Recordings were performed with the spike modules of a multichannel acquisition processor (Tucker-Davis Technologies). During the 7 days recovery period, mice were briefly anesthetized with isoflurane and bundles were screwed down 200μm on the first day and 50μm for the next 6 consecutive days. Mice were connected to commutators with flexible cables for habituation to recording conditions.

Non-stressed

Mice were recorded free-movingly in the home cage on day 1 for 15 min to assess baseline and then briefly anesthetized with isoflurane. After recovery, a second 15-min recording was conducted.

Acute stress

On day 2, the animals were immobilized on an acrylic plastic board lying on their back with surgical tape for 12 h during the light-off period. On day 3, mice were recorded free-moving in their home cages for a 15-min period to assess baseline. Then, under brief anesthetization with isoflurane, the mice were restrained again. The circular opening on the board enabled connection of the recording cable to the head implant Omnetics connector. After recovery from anesthesia, restrained mice were recorded for a second 15 min period for acute stressor exposure.

Chronic stress

Mice were repeatedly retrained to the acrylic plastic board for 6 h each day for the next 6 consecutive days (Day3-Day8). On day 9, mice were first recorded free-moving in the home cage for the first 15 min for baseline assessment. After short anesthetization with isoflurane, mice were immobilized on an acrylic plastic board. After waking up, restrained mice were recorded for a second 15 min period under chronic stress.

In order to exclude the influences of other factors such as anesthesia, acrylic plastic boards, surgical tapes, and repeated connections on CeM electrophysiology, the same protocols were repeated from day1 to day 9 without restraint. The second 15-min period was recorded in the free-moving condition after recovering from anesthesia.

Intravital window for confocal microscopy

For intravital confocal imaging of calcium transients in Brunner's gland and pancreas (control), we generated Glp1r-ires-Cre×Ai148(TIT2L-GC6f-ICL-tTA2)-D mice (*Cre*-driven GCaMP6f expression) and Glp1r-ires-Cre×Ai148(TIT2L-GC6f-ICL-tTA2)-D×Ai9 mice (*Cre*-driven GCaMP6f compounded with tdTomato expression). These strain nomenclatures were abbreviated as Glp1r[GCamp6] in main text. When 6-week-old, 8-hour food-restricted animals underwent the surgical procedures as below, followed by proximal duodenal/ pancreas abdominal glass window placement for intravital confocal microscopy. A purse string suture was placed on the incision edge between the rectus abdominis and the abdominal skin. The stomach was exteriorized through the midline incision. The pyloric antrum was loosely stitched to the left rectus abdominis to maximize the field of view over the proximal duodenum and pancreas through the cover glass. Then, the purse string suture was tightened to the groove made on a customized titanium ring (ID ø 14mm, OD ø 32mm, 1mm width, manufactured by Send Cut Send, USA). Drops of Low Toxicity Silicone Adhesive (KWIK-SIL, WPI, Sarasota, FL) were carefully applied to the outer surface of the proximal duodenum and pancreas before being attached to a round coverslip (ø15 mm, Electron Microscopy Sciences, Hatfield, PA) which was previously glued (Ultra Gel Control, Loctite, Hartford, CT) to a second, larger titanium ring (ID ø 14mm, OD ø 46mm, 1mm width manufactured by Send Cut Send, USA). As terminating procedure, anesthesia was switch to urethane 1.0-1.5 g/kg before mounting the animal over the confocal microscope. Calcium imaging was performed using a Leica SP8 confocal microscope equipped with a 10X objective lens along with a 0.75X amplification hardware setting. Scanning pixels were 400×400 per frame, and the pinhole was used at maximum value. Upon visualizing GCaMP6f-expressing Brunner's glands, continuous imaging series were acquired at ~3.2 frames/sec, FOV=2.25mm^2, 400X400 frame scanning speed.

Intravital imaging combined with cholecystokinin infusions

Before intravital window implantation, a MicroRenathane tubing (0.025", Braintree Scientific, Braintree, MA) was inserted into the peritoneal cavity, guided by a 23-gauge needle, and tightened to the skin with a purse string around the tubing. Cholecystokinin (CCK8) or saline infusates were freshly prepared. After a 12 minutes-long baseline and Saline^{ip} image acquisition period, 0.1mL of 10μg/Kg CCK8 was infused via the i.p. catheter at 0.1mL/min, after which post-injection series were acquired. Imaging was acquired continuously through the pre-, injection, and post-injection periods.

Intravital imaging combined with darifenacin and cholecystokinin infusions

Same procedure as above except that mice were infused with 20 mg/kg darifenacin hydrobromide (Sigma-Aldrich, #1164200) i.p., 6 minutes before CCK8 i.p. infusion. The administration dose of darifenacin was as described previously.[66]

Intravital imaging combined with cholecystokinin infusions and vagal lesions

To assess the effects of sensory vagal denervation on the above, nodose ganglia were injected with CCK-SAP or Blank-SAP 2 days before intravital window implantation. Subdiaphragmatic vagotomies were performed immediately before intravital window implantation. Intraperitoneal catheterization and CCK/saline injections were as described above.

Intravital imaging combined with cholecystokinin infusions and the lesions of ChAT positive terminals in BG

As described before, Glp1r-ires-Cre×Ai148(TIT2L-GC6f-ICL-tTA2)-D mice were injected with 200nL Anti-ChAT-SAP into the submucosal layer of duodenum bulb (adjacent to pyloric sphincter) at least 2 days before intravital window implantation. Intraperitoneal catheterization and CCK/saline injections were as described above. Imaging was acquired continuously through the pre-, injection, and post-injection periods.

Intravital imaging combined with vagus nerve electrical stimulation

Glp1r-ires-Cre×Ai148(TIT2L-GC6f-ICL-tTA2)-D mice were used in these experiments. Before intravital window implantation, the left (ventral) or right (dorsal) subdiaphragmatic vagus nerve trunk was separated from the esophagus with a Spinal Cord Hook. Minimally traumatic elastic cuff electrodes (Micro Cuff Sling, 200 μm/3pol/2,5mm/cable entry top, CorTec GmbH) were gently placed under the nerve. The cuff electrode cable ends were soldered to a male miniature pin connector (520200, A-M Systems) and connected to a Grass S48 Pulse Stimulator (A-M Systems). After a 12 minutes-long baseline image acquisition period, electric pulses at 1Hz were triggered via TTL signals (∼1.8mA, 2ms), followed 1-min off rest period. This cycle was repeated multiple times. Then, a 24 minutes-long post simulation image series was recorded.

Intravital imaging combined with electrical stimulation of the central nucleus of the amygdala

Glp1r-ires-Cre×Ai148(TIT2L-GC6f-ICL-tTA2)-D mice were used in these experiments. As described above, brain stimulation electrodes (Protech international; Tungsten 2-Channel Electrode (B Twisted Wire, MS303T/3-B/SPC) implantation was performed 7 days before intravital window implantation. On the experimental day, both the intravital window and an i.p. catheter was implanted. The stimulation electrode was connected to a Grass S48 Pulse Stimulator (A-M Systems). A cycle of 20 Hz electrical pulses were delivered to central amygdala, triggered via TTL signals at the maximum current of 0.2 mA. Experimental design during calcium transients imaging were as follows: *1*) one cycle of electric stimulation (ES1); *2)* i.p. infusion of 200μL of subthreshold dose of CCK (0.05 μg/Kg); *3)* one second electrical stimulation cycle (ES2); *4)* a third cycle of electrical stimulation (ES3); and *5)* one final cycle of electrical stimulation (ES4). Each stimulation cycle lasted one minute, with 10–20-minute intervals in between. 10 minutes-long baselines before simulation and 10 minutes-long post-stimulations resting periods were scanned for normalization and comparison.

Intravital imaging during chemogenetic stimulation of the central nucleus of the amygdala

Glp1r-ires-Cre×Ai148(TIT2L-GC6f-ICL-tTA2)-D mice were used in these experiments. As described above, the non-Cre-dependent construct AAV5-hSyn-hM3D(Gq)-mCherry was injected into CeA (AP: -1.0mm, ML: ±2.5mm, DV: -4.8mm ∼-5.2mm), 7-14 days before intravital window implantation. On the experimental day, both an intravital window and an i.p. catheter were implanted. CNO or vehicle infusates were freshly prepared. After a 12-min baseline and vehicle^{ip} image acquisition period, 0.1 mL of 5 mg/kg CNO was infused via the i.p. catheter at 0.1mL/min, after which a post-injection series was acquired. Imaging was acquired continuously throughout the pre-, injection, and post-injection periods.

Simultaneous Intravital imaging of Brunner's glands and single neuron in vivo recordings in dorsal motor nucleus of vagus

Glp1r-ires-Cre×Ai148(TIT2L-GC6f-ICL-tTA2)-D mice were used in these experiments. After an intravital window and an i.p. catheter implantation, a 16-channel single drive movable recording bundle (Innovative Neurophysiology, Inc. USA) was implanted into DMV (AP: -7.5mm, ML: ±0.3mm, DV: -5.3mm). Recordings were performed with the spike modules of a multichannel acquisition processor (Tucker-Davis Technologies). The locations of electrodes were also confirmed histologically. Time stamps of CCK8 pump infusion and image acquisition were fed into the acquisition processor via TTL signals and aligned with the single unit data.

In vivo ultrasound studies

Mice were maintained anesthetized with inhaled 1.5% isoflurane. Animals were kept in supine position on a 37°C heating platform, and heart and breath rates were monitored throughout. All data videos were recorded under approximately the same anesthesia, heart, and breathing parameters. To measure the sizes of stomach under different experimental conditions, videos were recorded capturing the whole stomach along both the esophagus-directed and duodenum-directed axis. Images were analyzed with Visual Sonics Vevo 2100 high-resolution ultrasound imaging system. To track and evaluate the movement of the duodenum, the analysis considered breathing periods to avoid movement confounds.

Gut permeability

Mice fasted for four hours before 4kDa FITC-dextran, 25 mg/ml (Chrondex #4013), was administered orally (20 mL/kg). Three hours after dosing, mice were anesthetized using isoflurane (induction 5%, maintenance 1.5% isoflurane, 0.7 L/min N2O, 0.3 L/min O2), and retro-orbital blood was collected and stored in heparin-coated tubes. Animals were then euthanized. The samples were centrifuged (4 °C, 7 min, 8000 g) and plasma collected in clear Eppendorf tubes (Fisherbrand™ Premium). Plasmas from PBS-administered control mice were used for defining the standard curve. FITC-dextran concentrations in plasma were analyzed in duplicates using a spectrophotometer (SpectraMax 340PC Microplate reader, Molecular Devices, San Jose, CA, USA), under excitation λ=490nm and emission λ=520nm.

Intraperitoneal Glucose Tolerance Tests

A bolus of a 20% glucose solution (2g glucose/kg) was intraperitoneally injected to 16-hour food restricted animals. Blood glucose levels were measured using the OneTouch Ultra2 Blood Glucose Monitoring System at 0, 15, 30, 60, and 120 minutes post-glucose

injections, through placing a small drop of tail blood on an unused test strip (OneTouch Ultra Test Strips). At the end of the experimental session mice were returned to a clean cage with water and food and monitored.

Oral glucose tolerance tests

Same procedure as above except that mice were orally gavaged with the glucose solution.

Behavioral tests

Food preference test

Mice were single housed for at least a week before testing. During the test, two different types of food pellets, each ~10g in total, were evenly distributed and left at the cage for 24 hours. Then the amounts remaining of each type of food were weighted, returned to cage, and this was repeated for three days at the exact same time of the day. Daily averages of food intake for each type of food were then calculated. We compared intake between four pairs of food types containing different contents of fat, sugar, protein, and fiber. All different types of food were purchased from Research Diets, Inc. Comparisons were as follows: 1. High-fat (D12451) *vs.* fiber-free high-fat (D13121101); 2. High-fat (D12451) *vs.* regular chow (D12450B); 3. fiber-free high-fat (D13121101) *vs.* fiber-free high-protein (D17120803); 4. fiber-free high-protein (D17120803) vs. high-protein (D22072013).

Probiotics preference test

Mice were deprived of water overnight. Two water bottles containing two types of aromatic solutions (banana *vs.* apple, 1:1000) were weighted and provided to the animals for 1hour *ad libitum*. The amount of solution remaining was weighted after the test. Then, for each mouse, the less preferred flavor was identified, and mixed to a probiotics cocktail (300mg/10ml water; probiotics were purchased from RenewLife, Inc). These mixes were provided to condition the mice for three days. In each training day, mice were deprived of water overnight, after which probiotics plus (less preferred) flavor was provided continuously. After three days of conditioning, mice were deprived of water overnight and provided with the two types of flavors (without any probiotics) for one hour. Flavor preferences before and after training were calculated.

Open field tests

Open field tests made use of automated video analyzes (EthoVision XT11.5, Noldus). Animals were placed on a Plexiglas arena (Med Associates, 25 cm × 30 cm). The total area was divided into a central (8.3 × 10 cm) and a marginal subarea. Immediately above the central subarea, a 150-W lamp was activated to induce natural aversion to this location. Animals were tested once in this arena. The sessions were digitally recorded, and animal activity immediately analyzed using automated video analysis algorithms (EthoVision XT11.5, Noldus).

Acute restraint stress protocol for behavioral assessment

The procedures are similar to those used for recording. The mice were transferred to a procedure room. For acute restraint stress, mice were physically confined for 12 h during the light-off period in hand-made tubular restrainers. The 12-hour restraint stress sessions started at 19:00 hs and ended at 7:00 hs.

Chronic restraint stress protocol for behavioral assessment

The mice were transferred to a procedure room. For chronic restraint stress, mice were immobilized as described above for 6 h daily for the next 6 consecutive days. After each restraint session, the animals were returned to their home cages and left undisturbed until the next session.

Early-life maternal separation

Pups were separated from the dam for 4 h each day starting on the second postpartum day (PD2) until day 14 (PD14). During separation, pups were transferred to paper cups containing cleaning bedding during the light-on periods. A heating pad (32°C ± 2°C) was placed under the pups. After 4 h, the pups were transferred back to their home cages with their dams. After day 14, pups remained in their home cages and were left undisturbed until weaning and testing.

Bacterial manipulations

Assessment of intestinal and fecal levels of Lactobacilli

B6 mice were administered sterile 0.9% saline (vehicle) or 10μg/Kg CCK solutions, intraperitoneally, daily, for seven days. Small intestinal contents, large intestinal contents, and feces were collected and diluted into sterile ddH_2O. Small intestinal contents were collected from distal ileum, and large intestinal contents were collected from proximal colon. In both cases, samples were collected from 10mm-long intestinal segments, and fecal samples (0.1mg) were diluted at 1:10000 in sterile water and applied to MRS plates for CFU measurements.

Lactobacilli and Staphylococcus co-cultured with bile in vitro

These experiments employed the chloramphenicol-resistant strain *Lactobacillus rhamnosus* (*Hansen*) *Collins* (ATCC 27773) as well as *Staphylococcus xylosus* (ATCC 29971). Bile was collected from five food-deprived mice. *Staphylococcus xylosus* and *Lactobacillus rhamnosus* were diluted in either 100 μL saline or 100 μL bile at room temperature for approximately 30 min. *Staphylococcus xylosus* solutions were cultured in brain heart infusion (BHI) plates at 37°C. *L. rhamnosus was* cultured on MRS agar plates with 20 mg/L chloramphenicol at 37°C containing anaerobic cultivation sets (Thermo Scientific, AnaeroPack™).

Oral gavage of probiotics

These experiments employed the chloramphenicol-resistant strain *Lactobacillus rhamnosus* (*Hansen*) *Collins* (ATCC 27773). B6 mice were administered sterile 0.9% saline solution (vehicle) or 10μg/Kg CCK solutions daily, for 3 days. On the third day, mice were administered around 10^8 CFUs of *Lactobacillus rhamnosus* by oral gavage. Mice continued to be administered saline or CCK daily for another two days, after which fecal samples were collected. Samples (100μl, from a solution of 1mg feces, diluted at 1:1000 in sterile water) were applied to MRS plates previously treated with 20mg/L chloramphenicol, and clones were counted.

Intra-cecum infusions of probiotics

Animals at the time of experiments were 6-week-old. The abdomen and dorsal back skin were shaved and cleaned. A small incision to the dorsal neck, and a midline incision into the abdomen, were made. The cecum was exteriorized through the midline incision. A purse string suture was placed on the distal caecal wall, proximal to the caecal lymphoid patch, into which the tip of MicroRenathane tubing (0.025", Braintree Scientific, Braintree, MA) was inserted. A purse string was tightened around the tubing, which was then tunneled subcutaneously to the dorsum via a small hole made into the abdominal muscle. A small incision to the dorsum between the shoulder plates was then made to allow for catheter exteriorization. The abdominal incision was then closed with sterile suture. All infusates (Renew Life Extra Care Probiotic, 6mg/mice/day) were freshly prepared in 0.1mL filtered ddH2O and infused at 0.1mL/minute.

Bacterial pathogen colonization experiments

These experiments employed either *Staphylococcus xylosus* (ATCC 29971) or *E. coli* EcAZ-2 (generously provided by Dr. Amir Zarrinpar). In *S. xylosus* experiments, animals lacking Brunner's glands, or their appropriate controls, were treated with probiotics (intra-cecum infusions, see above) or mucin (in drinking water) for three days. Then, mice were orally gavaged ~10^8 CFUs bacteria daily, for seven days. Mortality was recorded daily. For stressor exposure experiments, mice were first exposed to different stress conditions as described above. Then mice were orally gavaged with ~10^8 CFU *S. xylosus* (ATCC 29971) daily for three days. Blood samples were collected and 100μL of the samples were cultured on brain heart infusion (BHI) plates at 37°C.

For *E. coli* EcAZ-2 experiments, animals lacking Brunner's glands, or their appropriate controls, were treated with probiotics (intra-cecum infusions, see above) or mucin (in drinking water) for three days. Then, mice were orally gavaged ~10^{10} CFUs bacteria one single time. Seven days later, fresh stools were collected, cultured on LB agar plates with 50 μg/mL Kanamycin, and resulting clones counted. For stressor exposure experiments, mice were first exposed to different stress conditions as described above. Then mice were orally gavaged ~10^{10} CFUs bacteria one single time. Seven days later, fresh stools were collected, cultured on LB agar plates with 50 μg/mL Kanamycin, and resulting clones counted.

Antibiotic treatments and fecal microbiota transplantation

The broad-spectrum antibiotic treatment for mouse models was described before.[28] Specifically, a broad-spectrum antibiotic cocktail (0.25g Vancomycin, 0.25g metronidazole, 0.5g ampicillin, and 0.5g neomycin) were dissolved into 500 mL filtered water. To mask the bitter taste of this antibiotic solution, 5g of artificial sweetener (Splenda) was added. The resulting solutions were filtered with SteriCup, 0.22μm. The experiment used C57BL/6 mice maintained in the Mount Sinai SPF facility. All the C57BL/6 mice were given *ad libitum* access to the antibiotic mixture for 7 consecutive days in drinking water. Antibiotic treated mice were then orally gavaged daily with a freshly prepared solution from fecal samples of Brunner's gland-lesioned (BGx-DTx) or control (BG-saline) mice, at a concentration of 1g/mL, daily, for the next 7 days. Mortality was recorded daily.

Central Amygdala chemogenetic stimulation

Stereotaxic viral injections were performed 2 weeks before intravital window implantation. During the experiments, the chemogenetic design drug clozapine-N-oxide (CNO, 5mg/kg) and subthreshold CCK (CCK_{Low}, 0.05 μg/kg) were injected intraperitoneally daily. After 7 treatment days, fresh fecal samples were collected and added to MRS plates. For chemogenetic experiments involving EcAZ-2 colonization, mice were treated with CNO and CCK_{Low} for three days, after which they were gavaged once with 10^{10} CFU EcAZ-2. Mice continued to be injected with CNO and CCK_{Low} for three more days. Seven days after gavage, fresh stools were collected, cultured on MRS plates, and resulting clones counted.

Analyses of microbiome composition

Blood and intestine sample collection

Animals received preoperative analgesia (0.05 mg/Kg Buprenorphine s.c.) and maintained under deep anesthesia with 3% isoflurane until euthanasia. The abdomen was shaved and cleaned with iodine soap and wiped with 70% isopropyl alcohol. The abdominal skin was covered with a sterile surgical drape before a midline incision was made. The intestine was pulled onto the surgical drape to expose the inferior vena cava for blood collection. After cutting the duodenum away from pylori, the complete intestine was pulled out from the abdomen cavity and gently stretched over a sterile surgical drape. Different intestine segments were then identified and separated for further analysis.

Fresh fecal sample collection

Freely behaving animals were transferred to a sterile cage without bedding. Around 5 fecal pellets were collected within 15 mins. Feces were stored in -80°C (up to one month) before DNA extraction and sequencing.

Bacteria DNA extraction and targeted library preparation

Bacteria DNA from small and large intestinal contents, and from feces, were extracted using the ZymoBIOMICS®-96 MagBead DNA Kit (Zymo Research, Irvine, CA). Bacterial 16S ribosomal RNA (rRNA) gene targeted sequencing was performed using the

Quick-16S™ NGS Library Prep Kit (Zymo Research, Irvine, CA). Bacterial 16S primers amplified the V3-V4 region of the 16S rRNA gene. These primers were custom designed by Zymo Research to provide the best coverage of the 16S rRNA gene while maintaining high sensitivity. The sequencing library was prepared using an innovative library preparation process in which PCR reactions were performed in real-time PCR machines to control cycles and therefore limit PCR chimera formation. Final PCR products were quantified with qPCR fluorescence readings and pooled together based on equal molarity. The final pooled library was cleaned with the Select-a-Size DNA Clean & Concentrator™ (Zymo Research, Irvine, CA), and then quantified with TapeStation® (Agilent Technologies, Santa Clara, CA) and Qubit® (Thermo Fisher Scientific, Waltham, WA).

16S amplicon sequencing

The final library was sequenced on an Illumina® MiSeq™ with a v3 reagent kit (600 cycles). The sequencing was performed with 10% PhiX spike-in. All the mice including surgical mice were housed in the SPF-level Mount Sinai animal facility before sample collections for bacterial DNA extraction and 16S amplicon sequencing.

Bioinformatics Analysis

Unique amplicon sequences variants were inferred from raw reads using the DADA2 pipeline.[67] Potential sequencing errors and chimeric sequences were removed with the Dada2 pipeline. Taxonomy assignment was performed using Uclust from Qiime v.1.9.1 applied to the Zymo Research Database, a 16S rRNA genes database that was internally designed and curated, as reference. Composition visualization, alpha-diversity, and beta-diversity analyses were performed with Qiime v.1.9.1.[68] If applicable, taxonomy with significant abundance among different groups were identified by LEfSe[69] using default settings. Additional analyses including heatmaps, Taxa2ASV Decomposer, and PCoA plots were performed with Zymo Research proprietary scripts. As a confirmation, and to remove the influence of different reference databases, amplicon sequences were also analyzed using One Codex pipeline and its Targeted Loci Database. Significant enriched species, genera, and families were confirmed through Targeted Loci Database analysis results.

Bacterial culturing and identification

100μl dilutions of small or large intestinal contents, or fecal samples, in sterile water were applied to MRS (deMan, Rogosa, Sharpe, Millipore, #110660) plates containing anaerobic cultivation sets (Thermo Scientific, AnaeroPack™) and maintained at 37°C. For the drug-resistant bacterium *Lactobacillus rhamnosus* (ATCC 27773), the sterile dilutions of bacterial or fecal samples were placed on MRS agar plates with 20mg/L chloramphenicol at 37°C containing anaerobic cultivation sets (Thermo Scientific, AnaeroPack™). For *Staphylococcus xylosus* (ATCC 29971), 100μl of sterile dilutions of freeze-dried bacteria or blood samples were plated on brain heart infusion (BHI) plates or 20ml of BHI culture medium at 37°C. For the *E. coli* strain EcAZ-2, sterile dilutions of bacterial or fecal samples were placed on LB agar plates (for clone counting), or incubated in LB medium with 50 μg/mL Kanamycin (for use *in vivo*) at 37°C. For identification of bacterial strains, colonies were washed out from MRS plate using sterile PBS solution and DNA extracted for 16S rRNA gene sequencing.

Vesicles and membrane secretion analysis

Glp1r-ires-Cre×CD63-emGFP$^{l/s/l}$ mice were used to evaluate vesicle translocation and distribution before and after CCK treatment. The tetraspanin CD63 resides in endosomes, lysosomes, secretory vesicles, and plasma membranes and is transported between these compartments. Whenever robust secretion occurs from Brunner's glands, CD63-emGFP aggregates at the apical membrane region. Double transgenic mice were deprived of food overnight. On the next day, saline, or 10μg/Kg CCK was injected into two groups of mice. After 1h, animals were perfused with filtered saline, followed by 4% paraformaldehyde. Following perfusion, Brunner's glands segments were placed in 4% paraformaldehyde for 24 hours and then moved to a 20% sucrose solution in 0.02M potassium phosphate buffer (KPBS, pH 7.4) for 48hs. 5μm sections were obtained using a cryotome (Thermo Fisher) and mounted for confocal imaging.

Pseudorabies virus tracing

The abdomen of 8-hour food restricted animals was shaved and cleaned. A midline incision was made into the abdomen. Immediately after subdiaphragmatic vagotomy or celiactomy[35] when appropriate, stomachs were exteriorized through the midline incision, and the pyloric antrum was loosely stitched to the left rectus abdominis, to maximize the view of the proximal duodenum. PRV-Introvent-GFP[70] were loaded into a Nanofil™ 36G beveled needle (WPI, Sarasota, FL) and Silflex™ tubing (WPI, Sarasota, FL), connected to a Nanofil™ 10μl syringe (WPI, Sarasota, FL), and mounted on a Pump 11 Elite Nanomite (Harvard Apparatus, Holliston, MA). A 100nL injection was made at 10nL/s into the submucosal layer of duodenum bulb (adjacent to pyloric sphincter) or into the descending part of duodenum in control cases (adjacent to the sphincter of Oddi). The needle tip was carefully guided to avoid mesenteric blood vessels. After completing the infusions, needle was left in place for 5s before removal to ensure full absorption. After removing the loosing suture attached to the stomach, sterile suture was then applied to the skin.

Monosynaptic Retrograde Tracing from Brunner's Glands

Same procedure as above except that mice were injected with 100nL 1% FluoroGold™ (Fluorochrome, USA) solution.

Cross-sectional analysis of Immunological parameters in low-risk gastroduodenal mesenchymal tumors (GISTs) patients

Low-risk GIST surgery cases (Male, n=16, 55.7 ± 13.4 years; Female, n=13, 63 ± 10.1 years) performed at the Guangzhou First People's Hospital from 2020 through 2024 were selected for cross-sectional analysis (Ethical approval # K-2024-045-01). Low-risk GISTs

are treated with surgery alone and do not require radiotherapy/chemotherapy within 7 days after surgery. Preoperative and postoperative complete blood counts (CBC) were collected between 5 and 7 days postsurgery to exclude radiotherapy/chemotherapy effects on the immune system.

The eligibility criteria were as follows. Gastrointestinal bleeding was the initial complaint; ultrasound/endoscopy/CT examination confirmed that the tumor involved the gastroduodenal region; postoperative pathological diagnosis confirmed low-risk gastrointestinal mesenchymal stromal tumor (GIST) (i.e., the tumor is restricted in the intrinsic muscular layer, no infiltration to the plasma membrane nor the lymph nodes were detected, and the tumor didn't exceed the margins of the incision). Exclusion criteria included surgery involving the pancreas, spleen, or liver/biliary systems; serious complications such as sepsis, cachexia, acute renal insufficiency, high-risk hypertension, or splenic infarction. Cases with incomplete records, pregnancy, or lactation were also excluded. All cases were categorized into resection of the duodenal bulb (containing Brunner's glands) and preservation of the duodenal bulb (duodenal sites distal to Brunner's glands). Immunological parameters, including leukocyte, lymphocyte, neutrophil, and monocyte counts, were analyzed under a 2×2, per/post-surgery × resection site design.

Histology analysis

Histological procedures

Mice were deeply anesthetized with a ketamine/xylazine mix (400mg ketamine + 20mg xylazine/kgBW I.P.). All animals were perfused with filtered saline, followed by 4% paraformaldehyde. Following perfusion, brains or intestinal segments were placed in 4% paraformaldehyde for 24 hours and then moved to a 20% sucrose solution in 0.02M potassium phosphate buffer (KPBS, pH 7.4) for 2 days. Brains were then frozen and cut into four series of 40μm sections with a sliding microtome equipped with a freezing stage. To identify electrode locations, relevant sections were identified and mounted on slides. Sections were then photographed under bright field and fluorescence. For Pseudorabies virus visualization, 3,4 or 5 days after viral injection, mice were perfused, and brains cut at 40 μm.

HE staining

All animals were perfused with filtered saline and 4% paraformaldehyde. Intestinal tissues and spleen tissues were post-fixed, embedded in OCT and cryo-sectioned at 5μm. Tissue sections were stained with H&E and imaged using Zeiss Axio Imager using 10X and 40X objectives.

PAS staining-based void scores

To preserve Brunner's glands, goblet cells and intestinal mucus layers for posterior analyses *ex vivo*, immediately after excision, tissues were submerged in Carnoy's solution (60% ethanol, 30% chloroform and 10% glacial acetic acid) at 4°C for 2hrs and then placed into 100% ethanol, as described before.[18,71] Fixed tissues were embedded in OCT and cryo-sectioned at 5μm. Tissue was stained with the Periodic Acid Schiff (PAS) Stain Kit (Abcam, #ab150680) and imaged with Zeiss Axio Imager using 10X and 40X objectives.

Calculation of void scores using Deep Learning

Unlike goblet cells, Brunner's glands are most often in an intermediate state between being fully devoid of, and fully filled with, mucus. Accordingly, we generated a "void score" to approximately quantify mucin storage in each gland. We used the automated segmentation algorithm "Segment anything model" (SAM)[63] to quantify mucin content. When using a rectangle to label an individual gland, the algorithm defines its outer boundary. Now, if the given gland contains a relatively small amount of mucin, the algorithm will define its inner boundary. The quotient of the area associated with the inner boundary over the area associated with the outer boundary was defined as the gland's "void score", representing mucin storage in this gland. Whenever the void score was < 0.05, the gland was considered "void".

Mucin thickness measurements

As described above, duodenal, ileal and colonic samples were fixed with Carnoy's solution and cryo-sectioned at 5μm. Sections were then stained using the Periodic Acid Schiff (PAS) Stain Kit (Abcam, #ab150680), and imaged with a Zeiss Axio Imager (40X). 3-4 images were obtained per sample. imageJ was used to measure mucin thickness across 30-40 different regions of each image, and then to calculate mean thickness values.

Immunohistochemical staining

To visualize Fos via immunofluorescence, sections were incubated with a Rabbit Anti-c-Fos antibody (Rabbit Anti-c-Fos ab190289, 1:1000), followed by DyLight™ 649-conjugated goat anti-rabbit (IgG (H+L) DI-1649-1.5, Vector Laboratories, 1:200). Fos expression was analyzed and quantified as follows: Coronal sections collected at ∼160μm intervals were photographed at 10× magnification and montaged with ImageJ to preserve anatomical landmarks. Fos+ neurons in each section were detected and counted using ImageJ and expressed as the cumulative sum of Fos+ neurons within the relevant regions for each animal.

To visualize B cells, cell proliferation, and FDC light zones via immunofluorescence, 10μm spleen sections were incubated with Alexa647-conjugated anti-mouse IgD antibody (Biolegend, #405707, 1:200, Clone: 11-26c.2a), Brilliant Violet 421-conjuncted anti-mouse CD21/CD35 antibody (Biolegend, # 123421, 1:200, Clone: 7E9), and Alexa488-conjuncted anti-mouse/human Ki-67 antibody (Biolegend, # 151204, 1:200, Clone: 11F6) at 4°C overnight. Slices were washed three times using KPBS solution and imaged using Zeiss LSM980 Airyscan 2 with a 10X objective.

To visualize goblet cells via immunofluorescence, 10μm intestine slices were incubated with Rabbit Anti-MUC2 antibody (Abcam, #ab272692, 1:1000), followed by DyLight™ 649-conjugated affinipure goat anti-rabbit (IgG (H+L) DI-1649-1.5, Vector Laboratories, 1:200). Slices were washed three times using KPBS solution and imaged using Leica STED 3X with a 10X objective.

To visualize Brunner's gland DMV innervation via immunofluorescence, 10μm Brunner's gland slices were separated incubated at 4°C overnight with Goat Anti-GFP antibody (FITC) (Abcam, #ab6662, 1:1000) for DMV fiber; Rabbit polyclonal mCherry antibody (Abcam, #ab167453, 1:1000) for DMV synaptophysin; Goat-anti-ChAT antibody (Millipore, #AB144, 1:1000) for cholinergic neurons and Rabbit polyclonal to beta III Tubulin (Abcam, #ab18207, 1:1000) for neuron. 2nd antibodies were incubated at room temperature with DyLight™ 649-conjugated affinipure goat anti-rabbit (IgG (H+L) DI-1649-1.5, Vector Laboratories, 1:200) or FITC-conjugated affinipure donkey anti-goat IgG (H+L), Jackson Immuno Research Labs, 705-095-147, 1:200). Slices were washed three times using KPBS solution and imaged using Leica STED 3X with a 10X objective. To visualize cytokines Il1a and Cxcl9 signal distribution in colon, 10μm colonic sections were separately incubated at 4°C overnight with PE-conjugated anti-mouse IL-1a (Biolegend, #503203) and PE-conjugated anti-mouse CXCL9 (MIG) (Biolegend, #515603). Slices with mounted sections were washed three times using KPBS solution and imaged using Leica STED 3X with a 10X objective.

Celiac ganglia whole-mount immunostaining and tissue clearing

Whole tissue clearing as described previously.[72] Celiac ganglia were first fixed with 4% PFA at 4°C for > 24hs, tissues were then washed with PBS for 1hr, x 4 times. Tissues were then dehydrated at room temperature in a series of methanol/B1n solutions (20%, 40%, 60%, 80%,100%, 100%), 30 mins for each concentration. After delipidation (Dichloromethane, overnight) and discoloration (10% H_2O_2/methanol, overnight) at 4°C, tissues were rehydrated at room temperature in a series of methanol/B1n solutions (80%, 60%, 40%, 20%, 0%, 0%), 30 mins for each concentration. Tissues were transferred into a PTxwH solution with 1:1000 primary antibody and vibrated in an incubator at 37°C for 72hs. After thoroughly washing with PTxwH solution for 48hs, tissues were shaken in 1:500 secondary antibody PTxwH solution for 72hs and then washed out for 48hs. Each tissue was next imbedded with a mixture of dichloromethane (Sigma)/methanol (2 volumes/1 volume) for 3hr, and then with 100% dichloromethane for 15 mins, twice. The tissue was then transferred to a cover-glass bottomed chamber and then finally cleared with 100% dibenzyl-ether (Sigma) for 1hr twice and was prepared for confocal imaging.

RNAscope

Animals received preoperative analgesia (0.05 mg/Kg Buprenorphine s.c.) and were induced into deep anesthesia with 2% Isoflurane. Animals were transcardially perfused with ice cold Krebs-Henseleit Buffer Modified (K3753-10L, Sigma-Aldrich). Nodose ganglia were exposed and dissected as described previously.[64] The proximal 3mm end of the duodenum (to include the duodenal bulb, within which the glands of Brunner are located) were harvested. All fresh collected tissue were immediately placed into dry ice-cooled cryomolds and embedded with OCT before freezing under -80°C. Tissues were then cryo-sectioned at 10μm and mounted onto Superfrost Plus slides and kept at -80°C. After 1-hour brief fixation in 4% PFA at 4°C, slides were rinsed in PBS and dehydrated with ethanol. The RNAscope procedure was achieved with the RNAscope Multiplex Fluorescent Reagent Kit v2 with TSA Vivid Dyes (Cat No. 323270) and RNAscope® Probes of Mm-Glp1r (418851 RNAscope®), Mm-Cckar-C2 (313751-C2 RNAscope®), Mm-Chrm3-C3 (437701-C3 RNAscope®), 2.5 duplex mouse positive control probe (321651 RNAscope®) and 2-plex negative control probe (320751 RNAscope®).

Immunohistology of human Brunner's glands

Human Specimen

A duodenal section sample was obtained from a female patient aged 12 months who underwent surgery for duodenal duplication at the University of Tubingen Hospital. The sample was collected after approval by the local ethical committee (Project Nr. 066/2023BO2) and with the consent of the patients' parents according to the declaration of Helsinki.

Before embedding, tissue samples were fixed with 4% phosphate buffered paraformaldehyde (Merck KGaA, Darmstadt, Germany) overnight at 4 °C and washed trice with phosphate-buffered saline (PBS). For paraffin embedding, fixed tissue samples were dehydrated in an ascending alcohol series, followed by xylene and overnight infiltration of paraffin at 60 °C using a standard tissue processor (Citadel tissue processor; Shandon-Thermo Scientific, Waltham, MA, USA) for dehydration and transfer into paraffin. Before staining, paraffin sections (5 μm on a HM355 SS microtome, Microm International, Walldorf, Germany) were placed on Super Frost Plus slides (Microm International, Walldorf, Germany), dewaxed (Xylol for 3 × 5 min) and rehydrated by descending alcohol concentrations (100%, 96% and 70% for 5 min each) to distilled water. For tissue evaluation, Heidenhain's Azan staining was used.

For antigen retrieval, sections were heated in a steamer in citric acid monohydrate buffer (10 mM, pH 6.0, Merck, Darmstadt, Germany) and washed 3 times in TBS-buffer for 5 min each. Samples were blocked for 30 minutes with PBS containing 4 % donkey serum (BioRad, Hercules, CA, USA), 0.1 % bovine serum albumin (Roth, Karlsruhe, Germany), and 0.1 % Triton® X-100 (Roth, Karlsruhe, Germany), followed by incubation of anti-beta tubulin type III (1:1000, Biolegend, San Diego, CA, USA, #802001) diluted in PBS with 0.1 % bovine serum albumin and 0.1 % Triton® X-100 overnight at 4 °C in a humidity chamber. Afterwards, samples were washed with PBS three times for 5 to 10 minutes. The secondary antibody (donkey-anti-rabbit-alexa-488, 1:400, Life Technologies, Eugene, OR, USA, #A21206) was diluted in PBS, 0.1 % Triton X-100, and 0.1 % BSA and incubated for 60 minutes at room temperature. Nuclear staining was carried out with 4′,6-diamidino-2-phenylindole (DAPI), (200 ng/ml, Roth, Karlsruhe, Germany). After two washing steps with PBS for 5 minutes, the samples were washed in distilled water for 5 minutes, followed by mounting with Kaiser's glycerol gelatine (Merck, Darmstadt, Germany).

Human gut sections were imaged with a Zeiss Axio Imager.Z1 fluorescence microscope with Apotome module with 358, 488, 543, 647 nm for excitation and appropriate filter sets. Images were acquired using ZEN software. For immunofluorescence staining, exposure time for DAPI was 6.4 ms, and for TUJ 21.6 ms with 20x-objective (Plan-Apochomat 20x/0.8 M27).

Single nuclei sequencing

Duodenal segments containing Brunner's glands were rapidly extracted after perfusion with ice-cold 1X modified Krebs-Henseleit buffer (Sigma, K3753-10X1L). Samples were stored in -80°C for up to one month. Fresh-frozen tissues were disaggregated in 1mL of a nuclear extraction buffer with gentle slicing with a Tungsten Carbide Straight 11.5 cm Fine Scissor (Fine Science Tools, #14558-11) for 10 minutes on ice. Large debris were removed with a 40μm strainer (Falcon, # 352340). The left homogenate was spun at 1000xg for 8 min at 4°C, pellets washed once, and resuspended in 1 ml 1% BSA in PBS. The samples were diluted to 1000 nuclei/μl estimated from counting using Trypan blue staining and performed on a hemocytometer. Nuclei (~2000 per sample) were loaded onto a 10X Genomics Chromium platform to generate cDNAs carrying cell- and transcript-specific barcodes. Sequencing libraries were constructed using the Chromium Single Cell 3′′ Library & Gel Bead Kit 3. Libraries were sequenced on an Illumina NextSeq using paired-end sequencing.

CyTOF

Sample preparation

Animals received preoperative analgesia (0.05 mg/Kg Buprenorphine s.c.) and were induced into deep anesthesia with 2% isoflurane. The abdomen skin was shaved, and a midline incision was made into the abdomen. The spleen and mesenteric lymph nodes (MLNs) were collected. The inferior vena cava was exposed for blood collection. Femurs and humerus were dissected and cut open by removing both epiphyses. Bone marrow (BM) was flushed out and collected. MLNs)/spleen/ BM samples were then placed into 1.5ml tube with RPMI 1640 Media (Gibico, #21870092) + 10% FBS (Thermo Scientific, #A5256701). Tissues were gently sectioned using a Tungsten Carbide Straight 11.5 cm Fine Scissor (Fine Science Tools, #14558-11). Then, a 70μm cell strainer (Fisherbrand, #22-363-548) was placed in a 50-mL tube (Thermo Scientific, #339652), and rinsed with 2mL of RPMI 1640 Media + 10% FBS. Spleen samples were placed in the cell strainer and grinded with a syringe plunger. 10mL of RPMI 1640 Media + 10% FBS was flushed through the strainer. The sample was then centrifuged at 500-600xg for 5min at 4°C, and the supernatant discarded. The cell pellet was resuspended in 2–5mL cold 1x RBC Lysis buffer (Bioscience, #00-4300-54). The suspension was then incubated for 5 minutes at room temperature. The cell suspension was washed with 10–20mL cold RPMI 1640 Media + 10% FBS (ten-fold of RBC lysis buffer). Finally, the cells were 500–600xg centrifuged for 5min at 4°C, and the supernatant discarded. The pellet was resuspended with 2mL of RPMI 1640 Media + 10% FBS and kept on ice until staining. Samples collected from MLNs/Spleen/BM were stained using the mouse antibody panel listed in the key resources table. Cells were stained with an iridium intercalator overnight prior to CyTOF acquisition. Samples were washed twice with water, resuspended in normalization beads (Fluidigm), and filtered through a cell strainer.

Sample Processing

Samples were delivered to the processing facility (Mount Sinai HIMC) in fresh media. Cell counts were performed on a Nexcelom Cellaca Automated Cell Counter (Nexcelom Biosciences, Lawrence, MA, USA), and cell viability was measured utilizing Acridine Orange/Propidium Iodide viability staining reagent (Nexcelom). After washing cells in Cell Staining Buffer (CSB) (Fluidigm Corporation) Fc receptor blocking (Biolegend Inc., San Diego, CA, USA) and Rhodium-103 viability staining (Fluidigm) were performed simultaneously with surface markers for 30min at room temperature. Cells were subsequently washed twice in CSB and then fixed and permeabilized using the eBioscience Foxp3 / Transcription Factor Staining Buffer Set. After 30min incubation on ice with the fix/perm buffer, palladium barcoding was performed on each sample utilizing the Fluidigm Cell-ID 20-Plex Pd Barcoding Kit (Fluidigm) following manufacturer's instructions. After a 30min incubation at room temperature, samples were washed twice in CSB and pooled. Samples were washed in eBioscience Permeabilization wash and intracellular CyTOF staining was performed. Heparin blocking (100 units/mL) was utilized to prevent non-specific binding of intracellular antibodies to eosinophils.[73] After 30min incubation on ice, cells were washed twice in Permeabilization wash and final fixation was performed. Samples were fixed in 1mL 4.4% paraformaldehyde (Electron Microscopy Sciences Inc., Hatfield, PA, USA).125nM Iridium-193 (Fluidigm) and 2nM Osmium tetroxide (EMS) cell labeling was performed simultaneously with sample fixation.[74] After 30min incubation at room temperature, samples were washed twice with CSB and stored in FBS + 10%DMSO at -80°C until acquisition.

Data Acquisition/Processing

Prior to data acquisition, samples were washed in Cell Acquisition Solution (Fluidigm) and resuspended at a concentration of 1 million cells per ml in Cell Acquisition Solution containing a 1:20 dilution of EQ Normalization beads (Fluidigm). The samples were then acquired on a Helios Mass Cytometer equipped with a wide bore sample injector at an event rate of <400 events per second. After acquisition, repeat acquisitions of the same sample were concatenated and normalized using the Fluidigm software. The FCS file was further cleaned using the Human Immune Monitoring Center at Mt. Sinai's internal pipeline. The pipeline removed any aberrant acquisition time-windows of 3 seconds where the cell sampling event rate was too high or too low (2 standard deviations from the mean). EQ normalization beads that were spiked into every acquisition and used for normalization were removed, along with events that had low DNA signal intensity. The pipeline also was used to demultiplex the cleaned and pooled FCS files into constituent single sample files. The cosine similarity of every cell's Pd barcoding channels to every possible barcode used in a batch was calculated and then was assigned to its highest similarity barcode. Once the cell had been assigned to a sample barcode, the difference between its

highest and second highest similarity scores was calculated and used as a signal-to-noise metric. Any cells with low signal-to-noise were flagged as multiplets and removed from that sample. Finally, acquisition multiplets were removed based on the Gaussian parameters Residual and Offset acquired by the Helios mass cytometer.

Data analysis

Samples were normalized and debarcoded using the *Premessa* package in R. Cell populations were manually gated using FCS Express (https://www.standardbio.com/products/software/fcs-express, gating strategy, Figure S6A). Cell frequencies were calculated as the fraction of $CD45^+$ cells, which were quantified as a percentage of singlet cells. Relative abundances of major cell types such as total B cells, T cells, immature B cells, mature B cells, CD4 T cells, CD8 T cells, dendrite cells, macrophages and monocytes were calculated.

Olink proteomics analysis

Blood collection from inferior vena cava was described as above. Serum was separated from centrifuged blood. Olink data were generated from serum samples submitted to Olink Proteomics for analysis using the Olink Target 96 Mouse Exploratory panel assay of 92 analytes (Table S2). Out of 92 proteins, 69 were detected in >75% of samples and used in analysis. Data are presented as normalized protein expression values (NPX, Olink Proteomics arbitrary unit on $\log_2$ scale). See Table S2 for Olink missing values.

Metabolomics analysis for Short Chain Fatty Acids

The Neurometabolomics and Neuroinformatic Core at Mount Sinai conducted total fatty acid analysis using an Agilent 5977B GC/MSD gas chromatography-mass spectrometry system equipped with a Chemical Ionization (CI) source using methane as the reaction gas. Briefly, 40μl of plasma were dissolved into 300μl of ice-cold water acidified with 40μl of HCl 5N and further extracted with 300ul of diethyl ether. After this, 25μl of 1% pentafluorobenzylbromide (PFBBr) and 25 μl of 1% Diisopropylethylamine were added to the extracted diethyl ether solution and exposed for 30 min to room temperature to generate SCFA-PFB derivatives. Finally, a 1μl sample was injected into the GC/MS, with concentrations estimated using internal standard calibration curves, employing d7-isobutyric acid as the sample internal surrogate.

QUANTIFICATION AND STATISTICAL ANALYSIS

The exact value of all N (always number of animals), df, T/F, and p values are reported in Table S3 containing details on the statistics in the interest of space in text/legends. Figure legends report p values whenever relevant.

Data analyses, excluding electromyogram/electrophysiological/calcium imaging data, were performed using SPSS (v.21.0, IBM Predictive Software), Ethovision XT 11.5 (Noldus), GraphPad Prism 7 (GraphPad) and Matlab (v.17b, MathWorks). Before experiments, groups of animals assigned to the different experimental conditions were formed by naïve littermates, so that no randomization or other *a priori* criteria were adopted for group assignments. Experimental manipulations were analyzed according to within-subject repeated-measures designs whenever appropriate. Order of experimental conditions was randomly assigned across subjects. Samples sizes were chosen based on our previous studies employing similar intravital imaging, electrophysiological, behavioral, and neuronal ablation approaches. Samples sizes adopted in our current study were sufficient for detecting robust effect sizes while complying with guidelines from the Institutional Animal Care and Use Committee enforcing minimal and ethical animal usage. Experimenters were not blind to experimental conditions. Only animals carrying signs of distress/infection/bleeding/anorexia after the surgical procedures were excluded. Data from all animals used in the experiments were included in the final analyses and plots.

Mouse behavioral data analysis

For all behavioral studies, including those resulting from cell type-targeted lesions, or chemogenetic experiments, analyses made use of standard linear models (Pearson correlation), as well as one- or two-way (repeated measures) ANOVAs and post-hoc t-tests tests whenever relevant, for correcting for multiple comparisons. All data were reported as mean±SEM. In all cases sample sizes (N) denote number of animals used. All p-values associated with the t-tests performed correspond to two-tailed tests, and all post-hoc tests were corrected for multiple comparisons by employing Bonferroni correction. To assess potentially spurious results associated with non-normality, all significant effects were confirmed by rerunning the tests using the appropriate non-parametric test. All data are individually plotted (Prism 7, GraphPad), and the corresponding bar plot of the precision measures (mean ± SEM) were overlaid on the figure. The exact value of all N, df, T/F, and p values are reported in Table S3 containing details on the statistics. Effects were considered statistically significant whenever the corresponding statistic was associated with a p-value (Bonferroni-corrected when appropriate) strictly less than 0.05.

Calcium imaging data analysis

The raw data from calcium transients were first denoised using Noise2Void, a self-supervised deep-learning method for spatiotemporal enhancement of calcium imaging data.[62] Unlike Noise2Noise-based DeepCAD,[66] Noise2Void does not need paired images. Specifically, the first 2000 frames of the whole stack were transferred into patches with a (32, 64, 64) format, 70% of which were used for training and 30% for testing. Overall number of training epochs was ~150-200, allowing for obtaining the best model.

The learning rate started at 0.0004; if the loss-of-function value did not decrease within 10 epochs, a learning rate was defined as 0.5 x current rate. The whole stack was then transferred to a denoised dataset using the best model. The data were then motion-corrected using NoRMCorre.[60] We then generated the maximum intensity projection of the time-lapse images and utilized Cellpose, a deep learning-based segmentation method or a Mask R-CNN plus PointRend,[75] to segment individual glands. The output files corresponding to each region of interest (ROIs) of individual glands were stored as an ImageJ ROI file. Using the motion-corrected imaging data and segmentation ROI files, the mean values of both ROI GCaMP signals (ROI-Signal$_{Mean}$) and of the surrounding background (Background-Signal$_{Mean}$) for each individual gland were then calculated, following the strategy of the CaImAn software package.[60] The calcium signal of each gland was then defined as ROI-Signal$_{Mean}$ – Background-Signal$_{Mean}$. We then denoised each gland-associated raw data using a Gaussian filter. Next, for each gland, calcium signal z-scores were computed using the mean values and standard deviations obtained from 6min-long baseline periods without any stimulation. The *Python*-based packages used for data analysis included NumPy (version 1.22.0), SciPy (version 1.7.1), Pandas (version 1.4.1), Matplotlib (version 3.4.3), and Seaborn (version 0.11.2).

Electrophysiology data analysis

All electrophysiological data were stored in the TDT data storage structure. Spike sorting was performed manually using *offlinesorter* (Plexon). Data were imported into Python for analysis using custom-written software. The code for the analysis is available upon request. For DMV recordings, single unit firing rates were discretized into 5-s bins. Firing rates were Z-transformed, and the principal components of the transformed rates of all recorded units in response to the experimental infusion were calculated. To calculate the CCK response time (50% of max z-score values), the CCK injection time of data from both single units and BG calcium signals was set as 0. Then, 50% of the maximum z-score values of each single unit or BG calcium signal were calculated and set as thresholds. The z-score values were iterated from time 0. The time intervals were outputting when the z-score values are larger than the thresholds. CCK non-responsible neurons and BGs were removed from the analysis. For CeM recordings, single units' firing rates were discretized into 5 second bins. Firing rates were Z-transformed, and the principal components of the transformed rates of all recorded units in response to the experimental infusion were calculated. Single units' firing frequencies (firing events per second) were calculated for 15 minutes baseline and 15 minutes in the experimental conditions, including no stress, acute stress and chronic stress. Log_2 values of fold change were calculated by normalizing the mean frequency of the 15 minutes experimental condition to the mean frequency of the 15 minutes baseline condition. For DMV optical tagging data, ChAT+ neurons were verified using stimulus-associated spike latency test (SALT).[76,77]

Single nuclei sequencing data analysis

The unique molecular identifier (UMI) count matrices obtained from Cell Ranger (v. 7.1.0) processing for cell barcode aggregation, genome alignment, and unique molecular identifier transcript quantification was cleaned from cell free mRNA contamination with SoupX (v. 1.6.1) package[61] for R programming environment. The filtered matrices were analyzed with the Scanpy (v. 1.9.1) package[78] for a Python programming environment. For downstream analysis, low-quality cells were removed based on the following criteria. (i) Cells with relative high percentage of mitochondrial genes were removed. (ii) Cells with fewer than 120 genes were removed. (iii) Cells with doublet scores, which were estimated using Scrublet package higher than 0.4, were removed. Remaining cells were normalized to 10,000 reads per cell for downstream comparison. The top 3,000 variable genes were preselected and used for dimensionality reduction by PCA. Next, cell clusters were detected by constructing a shared nearest neighbor graph. The detected cell clusters were visualized by performing the PAGA combined UMAP algorithm. After fixing the clusters, marker genes were identified using Wilcoxon rank test. Panels of *dotplots* and *umaps* were created with Scanpy and matplotlib packages. The cell ontology classes were annotated using PanglaoDB (https://panglaodb.se/index.html).

CellPress
OPEN ACCESS

Supplemental figures

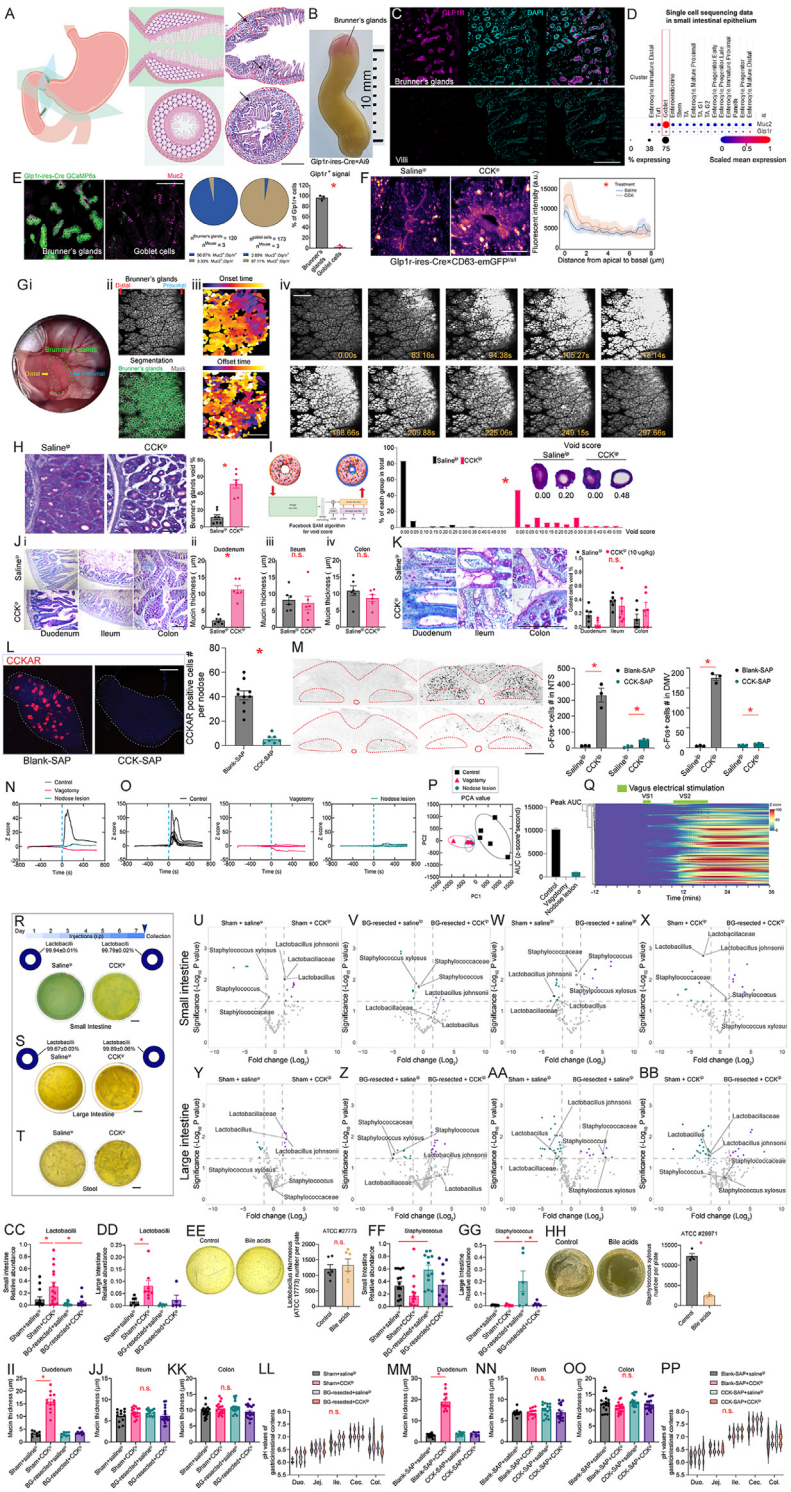

(legend on next page)

Figure S1. Vagal signals control the microbiome via the glands of Brunner, related to Figure 1

(A) The glands of Brunner (BG) are located within the submucosa of the proximal duodenum. Scale bar, 1 mm.

(B) In Glp1r-ires-Cre×Ai9 mice, Brunner's glands were easily visualized in the proximal duodenum, spanning 2 mm length × 3–5 mm width regions. Scale bar, 10 mm.

(C) *In situ* hybridization for *Glp1r* transcripts in BG and overlaying duodenal villi. Glp1r-reactive cells exclusively located in BG. Scale bar, 100 μm.

(D) We confirmed the previous finding using public transcriptome databases. Single-cell sequencing data from small intestine epithelium shows that goblet cells are Muc2-positive and Glp1r-negative (GEO: GSE92332, Single Cell Portal).

(E) Confocal imaging of duodenal samples from Glp1r [GCamp6] mice. Around 96.67% of Glp1r positive cells were localized to Brunner's glands, and only 2.89% to Muc2+ (goblet) cells. BG exhibited strong Cre-dependent GCaMP6 signals. By contrast, GCaMP6 signal was absent from mucous (Muc2+) goblet cells. Scale bar, 100 μm.

(F) Glp1r-ires-Cre×CD63-emGFP$^{l/s/l}$ mice were injected with vehicle or CCK^{ip} 1h before perfusion. Left: differential distribution of CD63-emGFP fluorescent intensities indicate greater translocation of vesicles to membrane after CCK^{ip} vs. saline^{ip} injections. Right: fluorescent intensity distribution from apical membrane to ~8 μm toward basal membrane, ANOVA effects of injection. *$p < 0.0001$. Scale bar, 10 μm.

(G) (i) Gut window for BG calcium imaging. (ii) Deep learning algorithms were used for segmenting individual glands for further analyses (segmented glands in green on right panel). (iii) Glands closer to the proximal end of duodenum display early onset and protracted deactivation of calcium transients. Scale bar, 200 μm. (iv) Timelapse of Brunner's glands calcium transients from onset (upper) to deactivation (lower).

(H) 1 h after an intraperitoneal CCK injection (CCK^{ip}, 10 μg/kg), PAS staining reveals robust BG voiding and mucin secretion: percentage of empty glands (void scores > 0.05). Scale bar, 100 μm.

(I) Left: the deep learning model "segment-anything" was used to calculate the "void score" of a given gland by adaptively detecting both the outside boundary and the internal (void) region (see STAR Methods for details). Right: histogram showing the distribution of BG void scores in saline vs. CCK injected mice. A total of 110 glands from 7 mice in each group.

(J) (i) Mucin thickness as assessed with PAS staining of samples from duodenum(ii), ileum(iii), and colon (iv). Scale bar, 200 μm.

(K) Left: PAS staining of duodenum, ileum, and colon epithelia in saline- vs. CCK-treated mice. Right: percentage of void goblet cells in duodenum, ileum, and colon epithelia in vehicle- vs. CCK^{ip}-treated mice, two-way mixed RM-ANOVA, injection × segment, $p = 0.1473$. Scale bar, 200 μm.

(L) CCK-SAP injected into nodose ganglia to ablate gut-innervating vagal sensory neurons. Controls injected with Blank-SAP. CCKAR^{+} neurons were completely ablated after CCK-SAP (counts from *in situ* hybridization). Scale bar, 100 μm.

(M) 10 μg/kg CCK^{ip}-induced Fos expression in NTS and DMV was disrupted by CCK-SAP-induced ablation of CCKAR^{+} neurons in nodose ganglia. Shown is Fos expression in NTS (middle) and in DMV (right). Scale bar, 100 μm.

(N) Average calcium transient *Z* scores before vs. after CCK infusions in control, vagotomized, and nodose-lesioned (CCK-SAP) mice. Blue line = CCK^{ip}.

(O) As in (N), this time showing data from all individual mice: Sham intact (left), vagotomized (middle) and CCK-SAP (right). Blue lines = CCK^{ip}.

(P) Left: principal-component analyses (PCAs) applied to *Z* scores from the three groups. Values from vagotomized and nodose-lesioned mice clustered together but were fully separate from the intact mice cluster. Right: the corresponding total area under the curve (AUC) values were calculated for the three groups.

(Q) Electrical stimulation of the vagus nerve (~1.8 mA) induces robust calcium transients in BG during intravital imaging. VS1, vagal stimulation period 1 (short); VS2, vagal stimulation period 2 (long).

(R and S) Confirmation that clones from MRS culture plates are *Lactobacilli*. Representative examples of MRS-based culture plates of small intestine, large intestine, and fecal contents in saline^{ip} and CCK^{ip} conditions. Upper percentage graph in (R): two MRS plates each from vehicle- vs. CCK-treated mice. Small intestine contents were sequenced using 16S protocols, and >99.7% of the clones were identified as *Lactobacilli*. (S) Same as in (R) but for large intestine: >99.6 of the clones were identified as *Lactobacilli*.

(T) MRS plates from fecal samples. Scale bars, 20 mm.

(U) Volcano plot contrasting relative abundances of bacteria after 16S sequencing of small intestine contents in sham + saline^{ip} vs. sham + CCK^{ip} injection. Cyan represents downregulated, and purple upregulated, species.

(V) As in (U), but for BG-resected + saline^{ip} vs. BG-resected + CCK^{ip} groups.

(W) As in (U) and (V), but for sham + saline^{ip} vs. BG-resected + saline^{ip} groups.

(X) As in (U)–(W), but for sham + CCK^{ip} vs. BG-resected + CCK^{ip} groups.

(Y) As in (U), but for large intestine.

(Z) As in (V), but for large intestine.

(AA) As in (W), but for large intestine.

(BB) As in (X), but for large intestine.

(CC–GG) Effects of BG resection on the microbiome. (CC) Relative abundances of total *Lactobacilli* count between sham + saline^{ip}, sham + CCK^{ip}, BG-resected + saline^{ip}, and BG-resected + CCK^{ip} from small intestinal samples. Two-way mixed RM-ANOVA, Sham vs. BG-resected, $p = 0.0016$. (DD) Same as (CC), but for large intestinal contents. Sham vs. BG-resected, $p = 0.0378$. (EE) *Lactobacilli* are resilient to bile acids. Testing strain is *Lactobacillus rhamnosus* (ATCC 27773). (FF) Same as (CC), but for *Staphylococci* instead of *Lactobacilli* for small intestinal contents, Sham vs. BG-resected, *$p = 0.0027$. (GG) Same as (FF), but for *Staphylococci* instead of *Lactobacilli* (large intestine contents). Sham vs. BG-resected, $p = 0.0120$.

(HH) *Staphylococcus xylosus* (ATCC 29971) is highly sensitive to bile acids.

(II) Mucin thickness as assessed with PAS staining. Samples duodenum of vehicle- vs. CCK^{ip}-treated sham and BG-resected mice. Two-way mixed RM-ANOVA, group × treatment, $p < 0.0001$.

(JJ) As in (II), but for ileal samples, $p = 0.0214$.

(KK) As in (II), but for colonic samples, $p = 0.0110$.

(LL) pH values were measured using contents from duodenum, jejunum, ileum, cecum, and colon of sham- and BG-resected mice. Two-way mixed RM-ANOVA, group × segment, $p = 0.3826$.

(MM) Mucin thickness as assessed with PAS staining. Samples from duodenum of vehicle- vs. CCK^{ip}-treated mice with nodose ganglia lesioned with CCK-SAP and controls (Blank-SAP). Two-way mixed RM-ANOVA, group × treatment, $p < 0.0001$.

(NN) As in (MM), but for ileal samples, group × treatment $p = 0.4507$; treatment, $p = 0.3532$; group, $p = 0.2687$.

(OO) As in (MM), but for colonic samples, group × treatment, $p = 0.5360$; treatment, $p = 0.013$; group, $p = 0.0985$.

(PP) pH values were measured using contents from duodenum, jejunum, ileum, cecum, and colon in Blank-SAP and CCK-SAP mice. Two-way mixed RM-ANOVA, group × segment, $p = 0.8260$.

All data are presented as mean ± SEM.

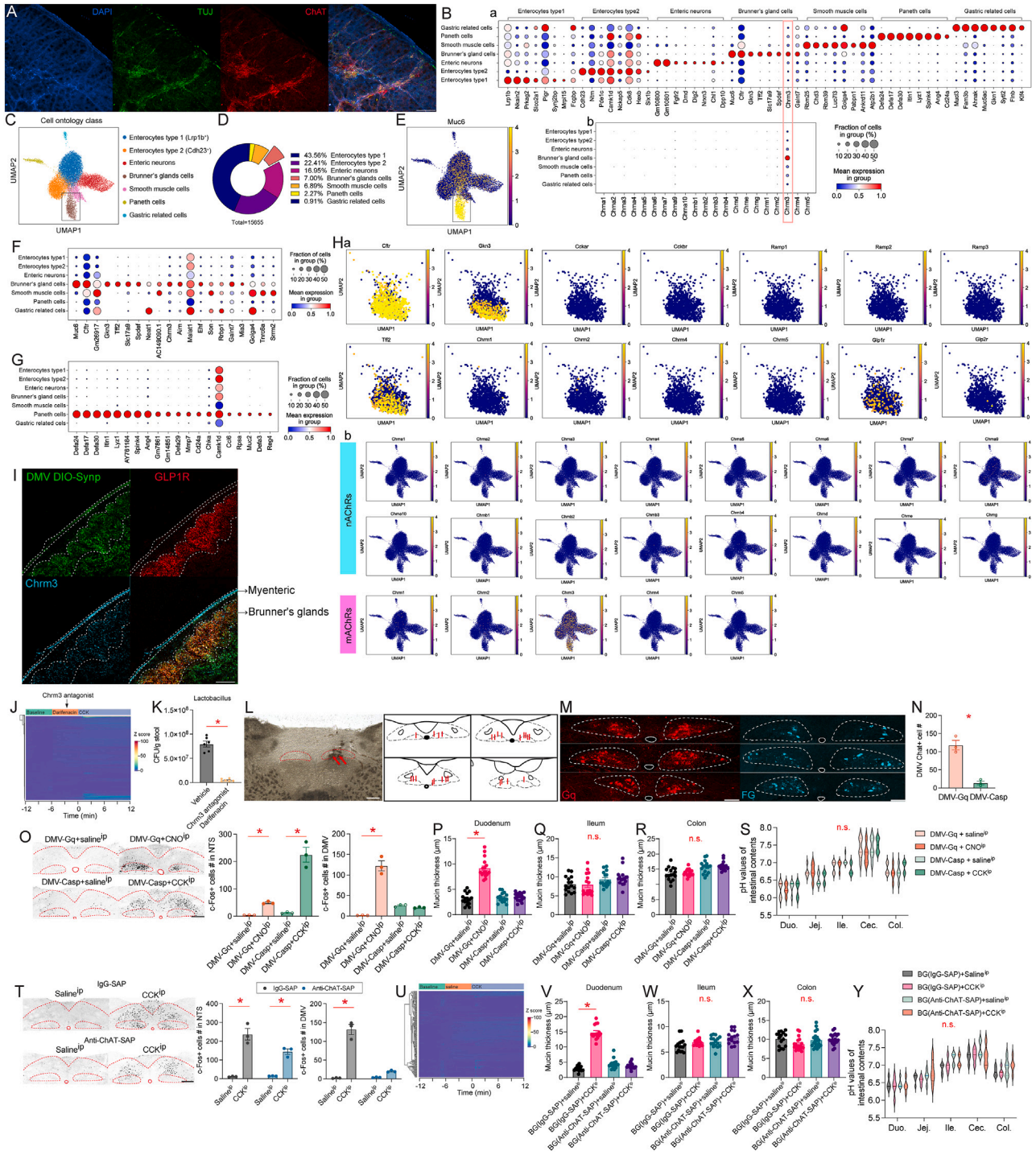

Figure S2. Vagal efferents control Brunner's glands, related to Figure 2

(A) Neuronal innervation of Brunner's glands in the mouse duodenum. Leftmost: nuclei were labeled with DAPI; middle left: neurites immunostaining against b-III tubulin (TUJ, green); middle right: ChAT positive neurites are stained for using an immunostaining against choline acetyltransferase (ChAT, red); rightmost: image with composition channels. Scale bar, 100 μm.

(B) (a) Top eight most enriched marker genes for the seven major cell types, namely, enterocytes type I (Lrp1b^{+}), enterocytes type II (Cdh23^{+}), enteric neurons, Brunner's glands cells, smooth muscle cells, Paneth cells, and gastric-related cells. Note the cholinergic secretory muscarinic receptor 3, *Chrm3*, among the topmost enriched genes in Brunner's glands cells. (b) Shown are all cholinergic receptor genes for the seven major cell types.

(C) Cell ontology class of duodenal tissue containing Brunner's glands, as defined by single nuclei sequencing.

(legend continued on next page)

(D) Percentage of the total number of validated cells for each cell type. In proximal duodenum, 7% of cells were identified as Brunner's glands cells.
(E) *Muc6* is the major marker used to annotate Brunner's glands cells.
(F) Top 20 most enriched genes in Brunner's glands.
(G) Top 20 most enriched genes in Paneth cells.
(H) (a) Previously reported marker genes for Brunner's glands cells: *Cftr*, *Gkn3*, and *Tff2* and co-expression with different receptor types present in Brunner's glands cells. Note the absence of CCK receptor *Ccka* and *Cckb* transcripts. (b) Related to (Bb), nicotinic acetylcholine (nAChRs) and muscarinic acetylcholine (mAChRs) receptor levels in BG-containing regions of duodenum.
(I) The AAV8.2-hEF1a-DIO-synaptophysin-EYFP construct was injected into DMV of ChAT-ires-Cre mice, and neural terminals as well as *RNAscope* probes for *Glp1r* and *Chrm3* were visualized in BG-containing slices. *Glp1r* and *Chrm3* and DMV-synaptophysin terminals co-localized on BG. Scale bar, 100 μm.
(J) CCK^{ip} (10 μg/kg) failed to induce calcium transients in BG after treatment with the Chrm3-selective antagonist darifenacin (20 mg/kg).
(K) Decreased fecal levels of *Lactobacilli* (culturing samples in MRS plates) after 3 daily doses of darifenacin (20 mg/kg).
(L) Histological identification of electrophysiological recording sites in DMV. Scale bar, 100 μm.
(M) Left: a representative example of red fluorescent protein-labeled ChAT+ neurons in DMV, after injection of the excitatory chemogenetic construct AAV9-DIO-DREADD(hM3Dq)-mCherry into DMV of ChAT-ires-Cre mice ("DMV-Gq mice"). Right: a number of DMV neurons were labeled by injecting retrograde dye fluorogold (FG) into Brunner's glands region in duodenum in mice. DMV regions infected with chemogenetic construct coincides with BG-projecting regions. Scale bars, 100 μm.
(N) Quantification for data shown in Figure 2J. *Caspase-3* overexpression ablated DMV ChAT+ neurons.
(O) Upper left: CNO-induced Fos expression in DMV of DMV-Gq mice. Lower left: CCK^{ip} failed to induce Fos expression in NTS and DMV after ablation of DMV ChAT+ neurons with *caspase-3* ("DMV-Casp" mice). Scale bar, 100 μm. Middle: Fos+ neuron count in NTS. Right: Fos+ neuron count in DMV.
(P) Mucin thickness as assessed with PAS staining of samples from duodenum for DMV-Gq + $saline^{ip}$, DMV-Gq + CNO^{ip}, DMV-Casp + $saline^{ip}$, and DMV-Casp + CCK^{ip} mice. One-way ANOVA, $p < 0.0001$.
(Q) As in (P) for ileum, $p = 0.0516$.
(R) As in (P) for colon, $p < 0.0001$.
(S) pH values of contents from duodenum, jejunum, ileum, cecum, and colon in DMV-Gq + $saline^{ip}$, DMV-Gq + CNO^{ip}, DMV-Casp + $saline^{ip}$, and DMV-Casp + CCK^{ip} mice. Two-way mixed RM-ANOVA, group × segment, $p = 0.2839$.
(T) Left: representative staining of Fos expression in NTS and DMV from BG(IgG-SAP) + $saline^{ip}$, BG(IgG-SAP) + CCK^{ip}, BG(anti-ChAT-SAP) + $saline^{ip}$, and BG(anti-ChAT-SAP) + CCK^{ip} mice. Scale bar, 100 μm. Middle: Fos+ neuron counts in NTS. Right: Fos+ neuron counts in DMV.
(U) CCK^{ip} (10 μg/kg) failed to induce calcium transients in BG in mice sustaining cholinergic denervation of BG, i.e., BG(anti-ChAT-SAP), but not controls BG(IgG-SAP) mice.
(V) Mucin thickness as assessed with PAS staining of samples from duodenum of vehicle- vs. CCK^{ip}-treated BG(IgG-SAP) and BG(anti-ChAT-SAP) mice. Two-way mixed RM-ANOVA, group × treatment, $p < 0.0001$.
(W) As in (V) for ileum, group × treatment, $p = 0.6553$; treatment, $p = 0.0127$; group, $p = 0.0057$.
(X) As in (V) for colon, group × treatment, $p = 0.0478$; treatment, $p = 0.1759$; group, $p = 0.1781$.
(Y) pH values of contents from duodenum, jejunum, ileum, cecum, and colon in vehicle- vs. CCK^{ip}-treated BG(IgG-SAP) and BG(anti-ChAT-SAP) mice. Two-way mixed RM-ANOVA, group × segment, $p = 0.7603$.
All data are presented as mean ± SEM.

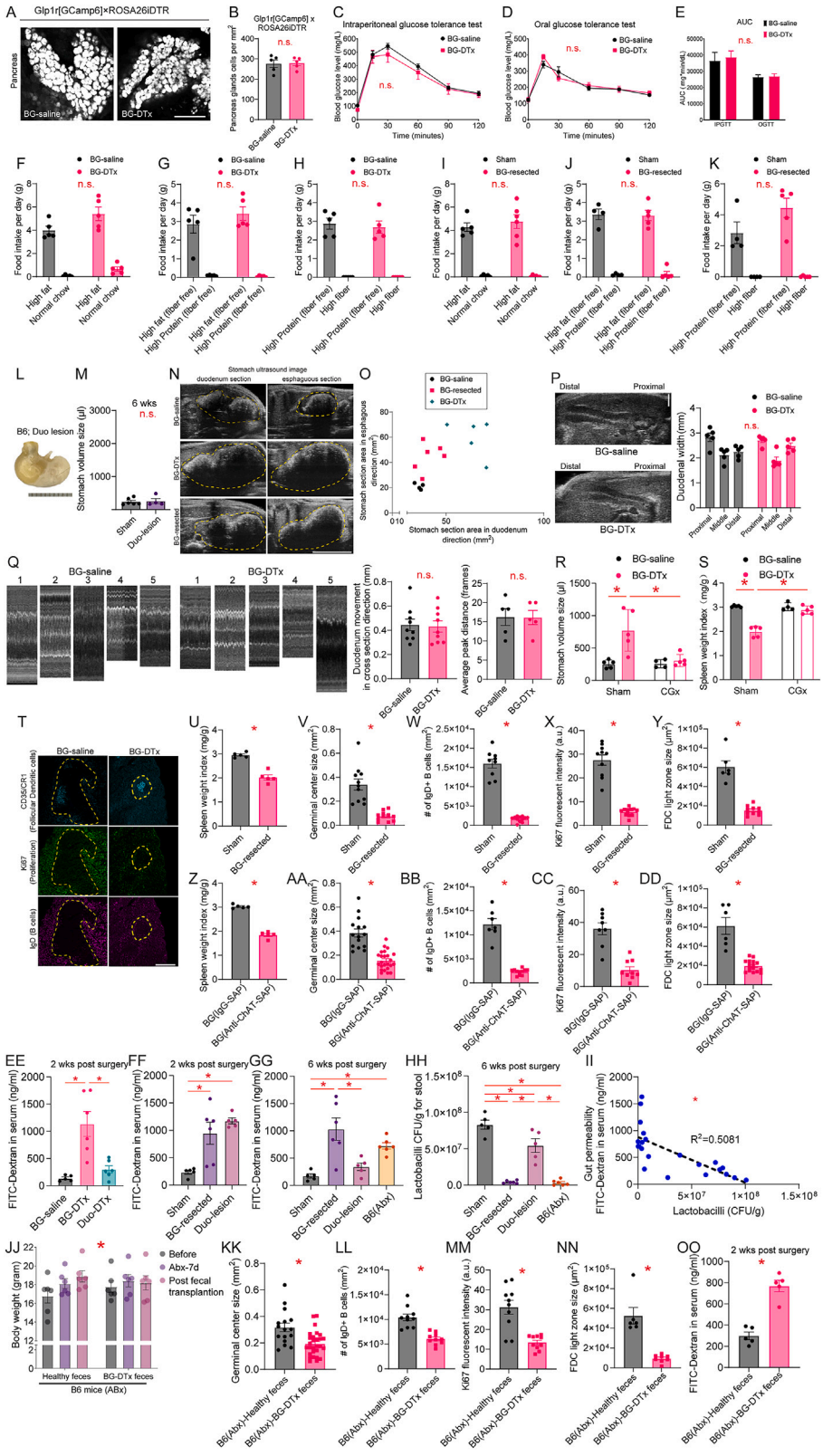

(legend on next page)

Figure S3. Ablation of the glands of the Brunner leads to an immunodeficiency syndrome and to mortality upon intestinal infection, related to Figure 3

(A and B) Glp1r[GCamp6]×ROSA26iDTR triple transgenic mice were used to exclude potential pancreatic lesions after DTx microinjections into BG. (A) Confocal imaging of gland cells in pancreas head. (B) $Glp1r^+$ pancreas glands cells/mm^2 in BG-vehicle vs. BG-DTx. Scale bar, 200 μm.

(C and D) DTx microinjections into BG did not alter blood glucose homeostasis. (C) Intraperitoneal glucose tolerance test (IPGTT), in BG-vehicle vs. BG-DTx mice, two-way mixed RM-ANOVA, surgery × sampling time, $p = 0.8065$. (D) Oral glucose tolerance test (OGTT), surgery × sampling time, $p = 0.0942$.

(E) AUC values for IPGTT and OGTT. No significant between-group effects detected. Unit is mg*min/dL.

(F) Daily food preferences for high-fat vs. chow pellets in BG-vehicle and BG-DTx mice. No significant between-group effects detected; two-way mixed RM-ANOVA $p = 0.5069$.

(G) As in (F) but for high-fat (fiber free) vs. high-protein (fiber free) pellets, $p = 0.3487$.

(H) As in (F) and (G) but for high-protein (fiber free) vs. fiber-rich pellets, $p = 0.6747$.

(I) As in (F) but for sham vs. BG-resected mice, $p = 0.4965$.

(J) As in (G) but for sham vs. BG-resected mice, $p = 0.7637$.

(K) As in (H) but for sham vs. BG-resected mice, $p = 0.1327$.

(L and M) In control experiments, resection of duodenal layers underneath Brunner's glands (Duo-lesion) failed to cause gastric distension. (L) Representative example of the aspect of the stomach in Duo-lesion mice. (M) Stomach size of Duo-lesion vs. Sham. Sham data as in Figure 3J. Scale bar, 10 mm.

(N and O) Ultrasound imaging was used to confirm gastric distension *in vivo*. Intact, BG-DTx, and BG-resection mice on a Glp1r-ires-Cre×ROSA26-iDTR background were anesthetized under isoflurane. Stomach section sizes in both the duodenal and esophageal orientations were measured. (N) Representative examples from control, BG-DTx, and BG-resection mice. Scale bar, 5 mm. (O) BG-DTx stomachs distended in both directions, while BG-resection stomachs distended preferentially in the esophageal direction.

(P) BG-saline and BG-DTx mice show similar sizes of proximal, middle, and distal duodenal segments. Two-way mixed RM-ANOVA, $p = 0.1951$. Scale bar, 2 mm.

(Q) No effects of lesions on duodenal movement patterns. Left: kymographs of duodenum movements in BG- saline and BG-DTx mice. Middle: duodenal cross-sectional movement. Right: peak distances of duodenum movement (frames).

(R) Celiactomies (CGx) rescued stomach sizes in BG-DTx mice. Two-way mixed RM-ANOVA, celiactomy surgery × DTx treatment, $p = 0.0118$; celiactomy surgery, $p = 0.0132$; DTx treatment, $p = 0.0035$.

(S) Celiactomies (CGx) rescued spleen sizes in BG-DTx mice. Two-way mixed RM-ANOVA, celiactomy surgery × DTx treatment, $p < 0.0001$; celiactomy surgery, $p<0.0001$; DTx treatment, $p < 0.0001$.

(T) Spleen sections stained against IgD, Ki67, and CD35/CR1 antibodies. Scale bar, 200 μm.

(U–Y) BG surgical ablation alters spleen characteristics, phenocopying BG-DTx animals. (U) Significantly smaller spleen sizes in BG-resected vs. Sham mice. (V) Smaller spleen germinal center sizes in BG-resected vs. Sham mice. (W) Marked suppression of B cell population in spleen of BG-resected mice. Shown is total number of IgD^+ B cells/mm^2 of spleen sections. (X) Suppression of cell proliferation markers in spleen of BG-resected mice. Shown is mean Ki67 fluorescent intensity in Sham vs. BG-resected mice. (Y) Suppression of follicular dendritic cell (FDC) markers in spleen of BG-resected mice. Shown is FDC light zone size in spleens of BG-resected vs. Sham mice.

(Z–DD) Cholinergic denervation of BG alters spleen characteristics, phenocopying BG-DTx animals.

(Z) Significantly smaller spleen sizes in BG(anti-ChAT-SAP) vs. BG(IgG-SAP) mice.

(AA) Smaller spleen germinal center sizes in BG(anti-ChAT-SAP) vs. BG(IgG-SAP) mice.

(BB) Marked suppression of B cell population in spleen of BG(anti-ChAT-SAP) mice. Shown is total number of IgD^+ B cells/mm^2 of spleen sections.

(CC) Suppression of cell proliferation markers in spleen of BG(anti-ChAT-SAP) mice. Shown is mean Ki67 fluorescent intensity in BG(anti-ChAT-SAP) vs. BG(IgG-SAP) mice.

(DD) Suppression of follicular dendritic cell (FDC) markers in spleen of BG(anti-ChAT-SAP) mice. Shown is FDC light zone size in spleens of BG(anti-ChAT-SAP) vs. BG(IgG-SAP) mice.

(EE) Genetic and surgical BG ablation induces a "hyperpermeable gut." Intestinal permeability measured by FITC-dextran penetration into systemic circulation 3 h after intraluminal injection of 4 kDa in BG-vehicle, BG-DTx, and Duo-DTx mice (Glp1r-ires-Cre×ROSA26-iDTR background). One-way ANOVA, $p = 0.0006$.

(FF) As in (EE) for sham, BG-resected, Duo-lesion mice (B6 background). Sham, BG-resected, and Duo-lesion mice were first measured early (2 weeks) after surgeries. One-way ANOVA, $p = 0.0011$.

(GG) As in (EE) but this time measurements were performed after full recovery from surgery (>6 weeks). Antibiotic-treated mice (B6 mice treated with antibiotics cocktails for 7 days, no surgical interventions) were also assessed. Duo-lesion mice now exhibited normal gut permeability, but BG-resected mice retained the full hyperpermeable gut phenotype. Note hyperpermeable gut after antibiotic treatment. One-way ANOVA, $p = 0.0004$.

(HH) Fecal levels of *Lactobacilli* (MRS culture plates) in Sham, BG-resected, and Duo-lesion mice 6 weeks after surgery. Antibiotic-treated mice (B6 mice treated with antibiotics cocktails for 7 days, no surgical interventions) were also assessed. One-way ANOVA, $p < 0.0001$.

(II) Negative linear association between *Lactobacilli* CFU counts and intestinal permeability across conditions ($n = 23$). Pearson $^*p = 0.0002$, $r = -0.7128$, and $R^2 = 0.5081$.

(JJ) Body weights of B6 mice after antibiotic cocktail (Abx) treatment and BG-DTx fecal transplant. Two-way mixed RM-ANOVA, group, $p = 0.831$; group × time, $^*p = 0.011$.

(KK-NN) Spleen characteristics were evaluated in C57BL/6J SPF mice following 7 days of treatment with an antibiotic cocktail (Abx). Abx mice were transplanted with fecal samples from BG-DTx and BG-saline mice.

(KK) Smaller spleen germinal center sizes in B6(Abx) transplanted with BG-DTx feces vs. B6(Abx) transplanted with BG-saline mice.

(LL) Marked suppression of B cell population in spleen of B6(Abx) transplanted with BG-DTx feces. Shown total number of IgD^+ B cells/mm^2 across spleen sections.

(MM) Suppression of cell proliferation markers in spleen of B6(Abx) transplanted with BG-DTx feces. Shown mean Ki67 fluorescent intensity in B6(Abx) transplanted with BG-DTx feces vs. B6(Abx) transplanted with BG-saline mice.

(NN) Suppression of follicular dendritic cell (FDC) markers in spleen of B6(Abx) transplanted with BG-DTx feces.

(OO) Intestinal permeability was assessed by measuring FITC-dextran concentrations in B6(Abx) transplanted with BG-DTx feces vs. B6(Abx) transplanted with BG-saline mice.

All data are presented as mean ± SEM.

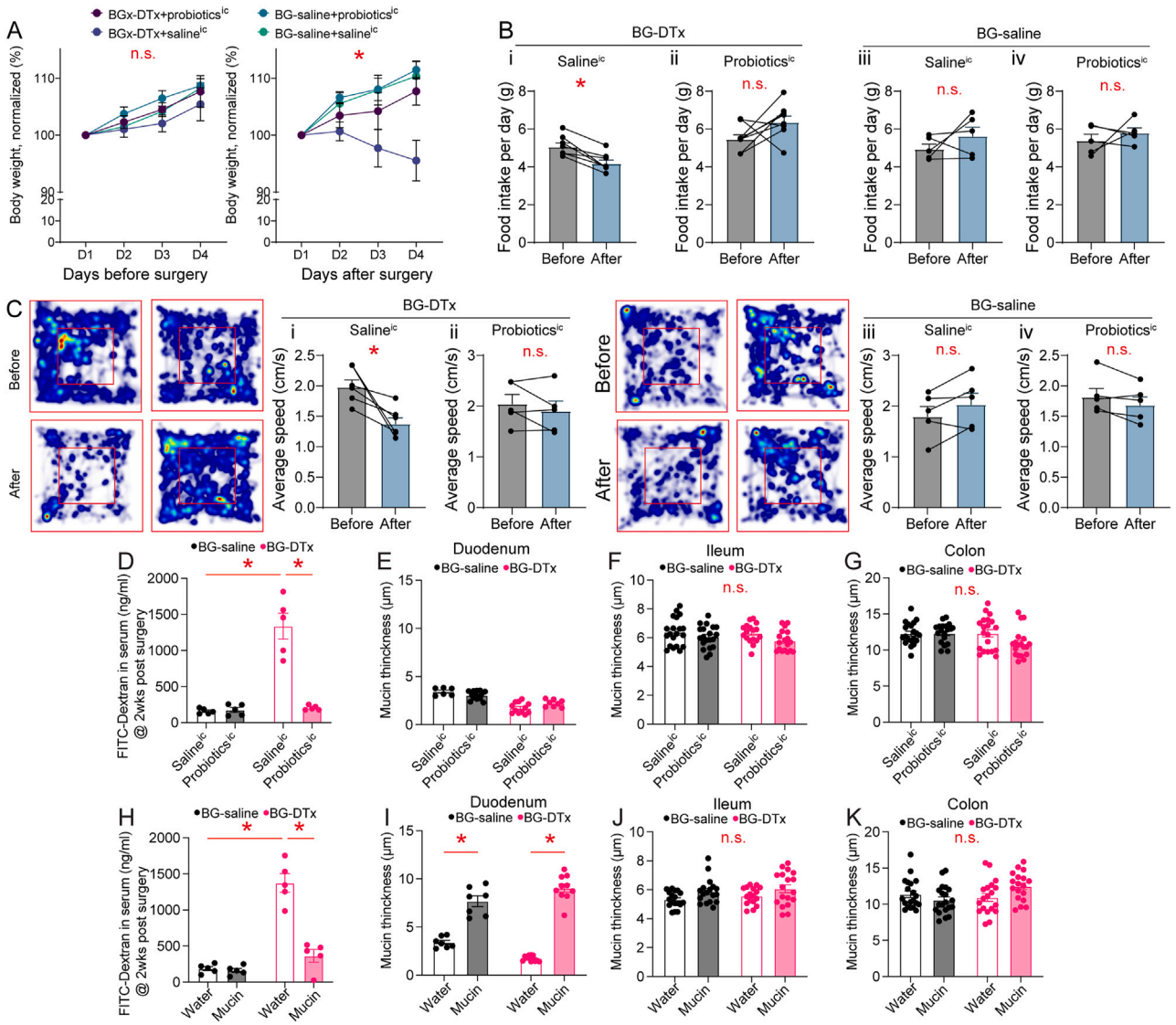

Figure S4. Probiotics and mucin restore immune functions and promote survival in animals lacking glands of Brunner, related to Figure 4

(A) Body weights before (left) and after (right) BG ablation followed by intra-cecal probiotic administration, two-way mixed RM-ANOVA, before surgery, intervention effect, $p = 0.3932$; after surgery: $p = 0.0144$.

(B) Daily food intake before and after surgery for saline and probiotics treatments. (i) BG-DTx + saline^{lc}. (ii) BG-DTx + probiotics^{lc}. (iii) BG-saline + saline^{lc}, and (iv) BG-saline + probiotics^{lc}.

(C) Open-field tests for vehicle and probiotics treatments. Upper: heatmaps of mice in the 4 treatment groups before and after surgery. Lower: (i) BG-DTx + saline^{lc}. (ii) BG-DTx + probiotics^{lc}. (iii) BG-saline + saline^{lc}, and (iv) BG-saline + probiotics^{lc}.

(D) Hyperpermeable gut recovered by probiotics. Intestinal permeability measured by FITC-dextran penetration into systemic circulation 3 h after intraluminal injection of 4 kDa FITC-dextran in BG-saline + saline^{lc}, BG-saline + probiotics^{lc}, BG-DTx + saline^{lc}, and BG-DTx + [*Lac* + *Bif*]probiotics^{lc} mice. Two-way mixed RM-ANOVA, group × treatment, $p < 0.0001$.

(E) Mucin thickness as assessed with PAS staining of samples from duodenum of BG-saline + saline^{lc}, BG-saline + [*Lac* + *Bif*]probiotics^{lc}, BG-DTx + saline^{lc}, and BG-DTx + [*Lac* + *Bif*]probiotics^{lc} mice. Two-way mixed RM-ANOVA, group × treatment, $p = 0.0074$.

(F) As in (E) for ileum, $p = 0.5627$.

(G) As in (E) for colon, $p = 0.0801$.

(H) Intestinal permeability was assessed by measuring FITC-dextran in systemic circulation 3 h after intraluminal injection of 4 kDa FITC-dextran in BG-saline + water, BG-saline + mucin, BG-DTx + water, and BG-DTx + mucin mice. Two-way mixed RM-ANOVA, group × treatment, $p < 0.0001$; treatment, $p < 0.0001$; group, $p < 0.0001$.

(I) Mucin thickness as assessed with PAS staining duodenal samples from BG-saline + water, BG-saline + mucin, BG-DTx + water, and BG-DTx + mucin mice. Two-way mixed RM-ANOVA, group × treatment, $p = 0.0001$.

(J) As in (I) for ileum, $p = 0.8661$.

(K) As in (I) for colon, $p = 0.019$; treatment, $p = 0.4571$; group, $p = 0.1752$.

All data are presented as mean ± SEM.

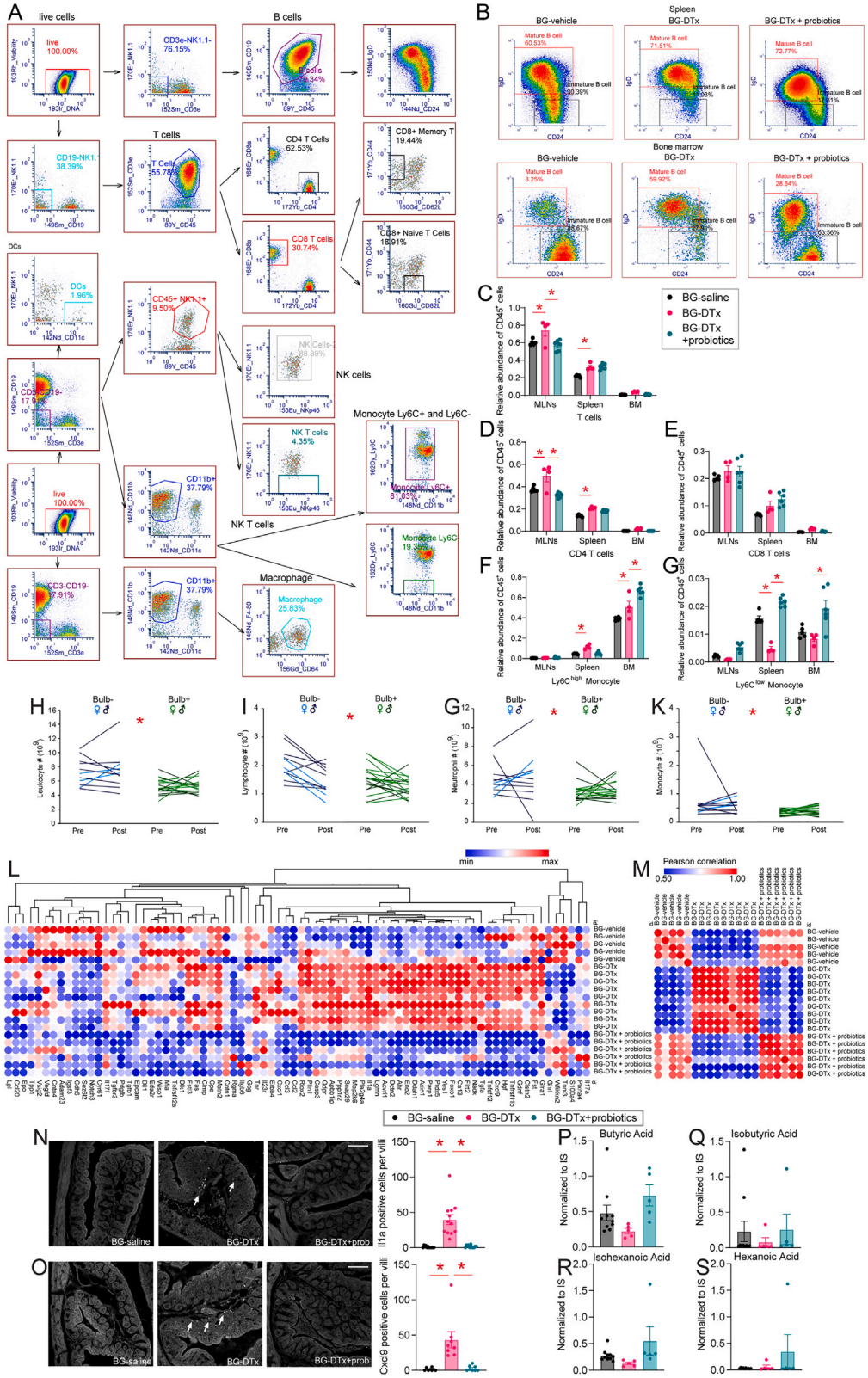

(legend on next page)

Figure S5. Immune and metabolomics signatures are rescued by probiotic treatment in animals lacking the glands of Brunner, related to Figure 5

(A) Depiction of the manual cell subpopulation gating strategy.

(B) In spleen and bone marrow, B cell subpopulations characteristics are changed in BG-DTx mice, an effect partially rescued by probiotics.

(C–G) Relative abundance of immune cells from the total pool of live $CD45^+$ cells in mesenteric lymph node, spleen, and bone marrow from BG-saline, BG-DTx, and BG-DTx + probiotics mice on a Glp1r-ires-Cre × ROSA26-iDTR background. (C) Total T cells, (D) CD4 T cells, (E) CD8 T cells, (F) $Ly6C^{high}$ monocytes, and (G) $Ly6C^{low}$ monocytes. In all cases, two-way RM-ANOVA, group effect, and organ × group (except CD8 T cells) $p < 0.006$. Bonferroni BG-saline vs. BG-DTx, and BG-DTx vs. BG-DTx + probiotics in different organs, all comparisons $^*p < 0.05$. All other comparisons resulted non-significant (n.s.).

(H–K) Cross-sectional analysis of immune profiles of gastroduodenal stromal tumor patients. The cases are divided into duodenal bulb resection group (loss of region containing BG, Bulb−, 8 males, 52.7 ± 16.7 years; 3 females, 70 ± 2.3 years) and duodenal bulb preservation group (Bulb+, 8 males, 58.7 ± 9.3 years; 10 females, 60.8 ± 10.5 years). Whole blood sample cell counts before and after tumor resection surgery were selected (>5 and <8 post-surgical days) and analyzed (two-way mixed RM-ANOVA). (H) Leukocytes, surgery type effect, $^*p < 0.001$; period (pre- vs. post-surgery) effect, $p = 0.724$; surgery × period, $p = 0.875$. (I) Lymphocytes, surgery effect, $^*p = 0.014$; period, $p < 0.001$; surgery × period, $p = 0.112$. (J) Neutrophils, surgery effect, $^*p = 0.007$; period, $p = 0.617$; surgery × period, $p = 0.974$. (K) Monocytes, surgery effect, $^*p = 0.004$; period, $p = 0.79$; surgery × period, $p = 0.347$.

(L) Heatmap of the Olink proteomic results.

(M) Pearson correlation matrices based on the Olink proteomics analyses across BG-saline, BG-DTx, and BG-DTx + probiotics groups.

(N) Left: representative images of colon sections from BG-saline, BG-DTx, and BG-DTx + [*Lac* + *Bif*]probiotics mice using an immunostaining against Il1a antibody (white). Right: Il1a positive signals in colon tissue of BG-DTx mice. One-way ANOVA, $p < 0.0001$. Scale bar, 100 μm.

(O) Left: as in (N) but for immunostaining against Cxcl9 antibody (white). Right: Cxcl9 positive signals in colon tissue of BG-DTx mice. One-way ANOVA, $p = 0.0002$. Scale bar, 100 μm.

(P–S)Metabolomic analysis of blood samples from BG-saline, BG-DTx, and BG-DTx + probiotics. (P) Butyric acid: one-way ANOVA, $p = 0.0542$. (Q) Isobutyric acid: $p = 0.7495$. (R) Isohexanoic acid: $p = 0.1063$. (S) Hexanoic acid: $p = 0.2572$.

All data are presented as mean ± SEM.

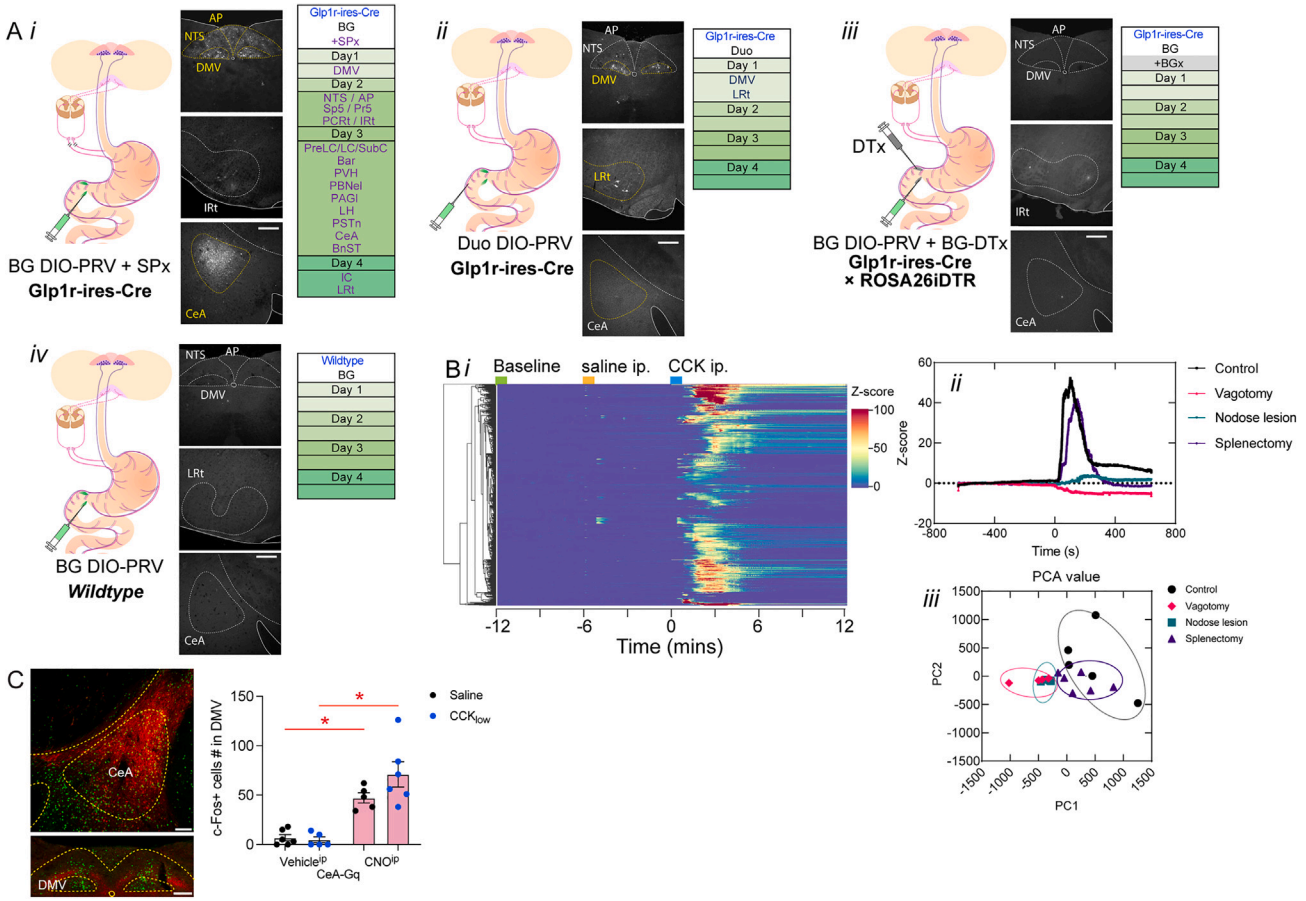

Figure S6. Central nucleus of the amygdala controls the intestinal microbiome via modulation of Brunner's glands secretion, related to Figure 6

(A) Control experiments for *Cre*-dependent DIO-PRV tracing. (i) DIO-PRV tracing from Brunner's glands in Glp1r-ires-Cre mice sustaining splenectomies (SPx) failed to alter labeling; (ii) DIO-PRV tracing from duodenum Glp1r^{+} enteric neurons in Glp1r-ires-Cre mice failed to yield brain labeling; (iii) DIO-PRV tracing from Brunner's glands in BG-lesioned (BG-DTx) Glp1r-ires-Cre×ROSA26iDTR mice failed to yield labeling in brain; (iv) DIO-PRV tracing from Brunner's glands in wild-type mice failed to yield brain labeling. The *Z* score data for other conditions in (ii) and (iii) are also from Figure 1. Scale bars, 100 μm.

(B) Duodenal sympathetic denervation (splenectomies) failed to block Brunner's glands calcium transients and secretion after CCK infusions.

(C) Left: representative image of neuronal fibers (red) of CeA origin innervating the NTS and DMV regions. Scale bars, 100 μm. Right: both chemogenetic CeA stimulation + saline and chemogenetic CeA stimulation + CCK $_{low}$ increased neural activity in dorsal vagal complex (DMV), as measured by *Fos* reactivity. Two-way mixed RM-ANOVA, main effect of CeA activation, $p < 0.0001$; CeA activation × CCK $_{low}$ treatment, $p = 0.1134$; CCK $_{low}$ treatment, $p = 0.1779$.

dorsal motor nucleus of the vagus, DMV; lateral reticular nucleus, LRt; nucleus of the solitary tract / area postrema, NTS / AP; nucleus ambiguus, Amb; spinal trigeminal nucleus / principal trigeminal sensory nucleus, Sp5 / Pr5; parvicellular reticular nucleus / intermediate reticular nucleus, PCRt / IRt; per-locus coeruleus / locus coeruleus / subcoeruleus, PreLC / LC / SubC; Barrington's nucleus, Bar; paraventricular hypothalamic nucleus, PVH; parabrachial nucleus, externolateral part, PBNel; lateral periaqueductal gray, PAGl; lateral hypothalamus, LH; parasubthalamic nucleus, PSTn; central nucleus of the amygdala, CeA; bed nucleus of the stria terminalis, BnST; insular cortex, IC; ventral tegmental area, VTA. All data are presented as mean ± SEM.

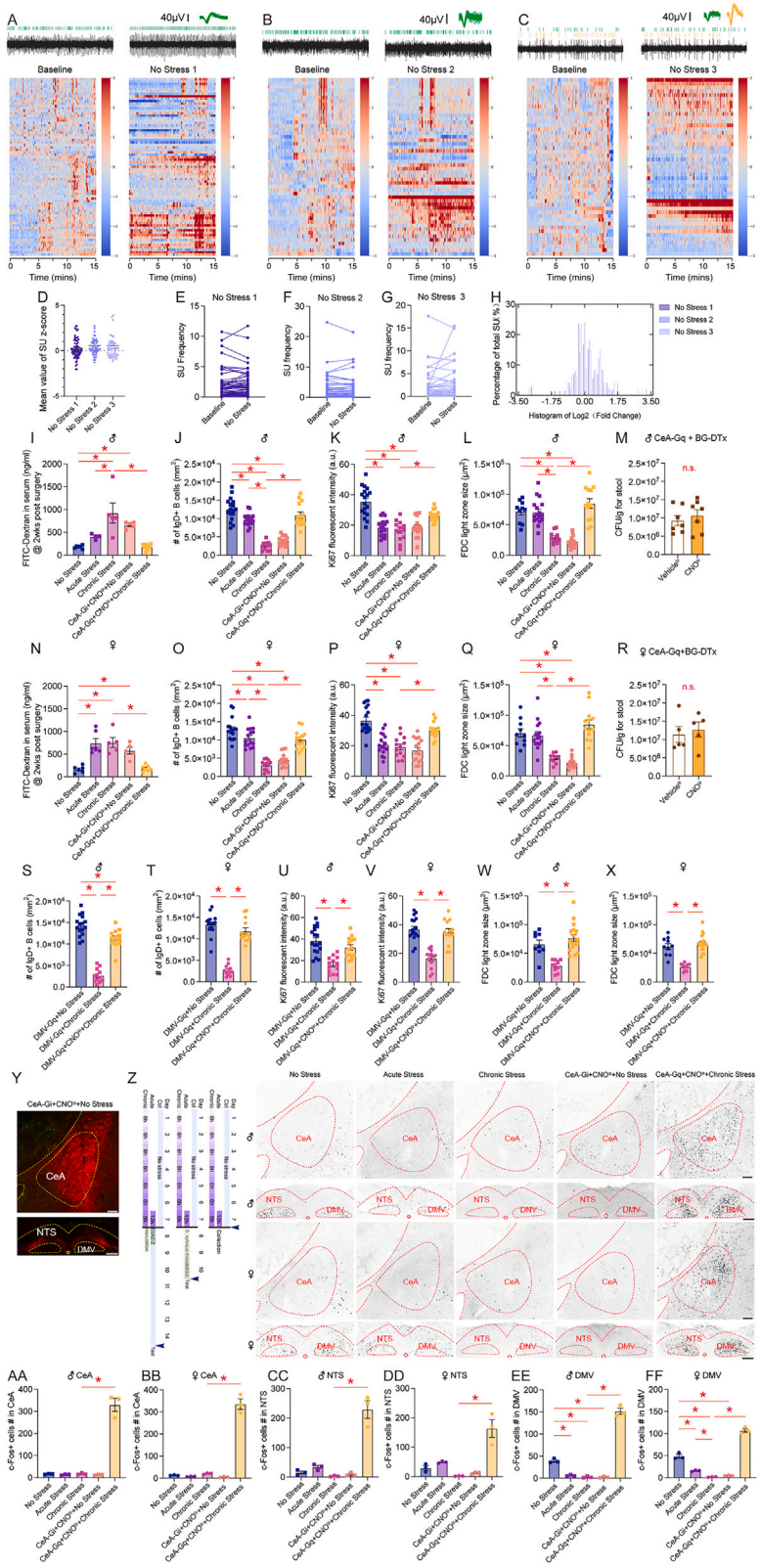

(legend on next page)

Figure S7. Amygdalo-vagal-glandular circuits are inhibited by chronic stress and mediate stress-induced altered intestinal microbiome and immunodeficiency, related to Figure 7

(A–C) Single neuron activity in CeA remain stable in the absence of stress. CeA cells were recorded as in Figure 7 but in the absence of stress. Scale bars, 40 μV.
(A–C) Examples of CeA population activity in the absence of restraint stress (A, 73; B, 50; C, 47 single units). Top: representative traces of single neuron activity in CeA. Bottom: heatmap shows Z-transform of time-binned firing frequencies of recorded units, calculated with respect to baseline in the *non-stress condition*.
(D) *Z* score values of the firing frequencies for each recorded CeA cells remained stable in the *non-stress* condition. One-way ANOVA, $p = 0.4612$.
(E–G) Refer to (A)–(C) above. The firing frequencies associated with the CeA units (shown respectively in A-C) remained stable in no-stress condition. Paired t tests, $p > 0.2$.
(H) Histograms calculated from fold changes in firing frequency (log_2) from examples above.
(I) Intestinal permeability was assessed by measuring FITC-dextran in systemic circulation 3 h after intraluminal injection of 4 kDa FITC-dextran. Experimental conditions were non-stress, acute stress, chronic stress, CeA suppression (CeA-Gi + CNO^{ip}; no stress), and CeA activation with chronic stress (CeA-Gq + CNO^{ip} + chronic stress). In male mice, intestinal permeability increased in response to both chronic stress and CeA suppression, an effect reversed by CeA activation. One-way ANOVA, $p < 0.0001$.
(J–L) As in (I) but for spleen characteristics. (J) As in (I) for total number of IgD^+ B cells/mm^2 in spleen sections, $p < 0.0001$. (K) As in (I) for mean Ki67 fluorescent intensity, $p < 0.0001$. (L) As in (I) for FDC light zone size, $p < 0.0001$.
(M) CeA activation fails to enhance *Lactobacilli* growth in male mice with BG lesions.
(N) As in (I) but for female mice, $p < 0.0001$.
(O–Q) As in (J–L), but for female mice. One-way ANOVAs, all $p < 0.0001$.
(R) As in (M), for female mice.
(S–X) Altered spleen characteristics produced by chronic stress are recovered by vagal stimulation in both male and female mice.
(S) Total number of IgD^+ B cells/mm^2 in male mice, one-way ANOVA, $p < 0.0001$.
(T) Total number of IgD^+ B cells/mm^2 in female mice, $p < 0.0001$.
(U) Mean Ki67 fluorescent intensity in male mice, one-way ANOVA, $p < 0.0001$.
(V) Mean Ki67 fluorescent intensity in female mice, $p < 0.0001$.
(W) FDC light zone size in male mice, $p < 0.0001$.
(X) FDC light zone size in female mice, $p < 0.0001$.
(Y) Representative examples of CeA, NTS, and DMV sections after the inhibitory chemogenetic construct AAV5-hM4Di-mCherry was injected into the CeA region. Scale bars, 100 μm.
(Z) Representative examples of Fos expression in male and female mice in non-stress, acute stress, chronic stress, CeA-Gi + CNO^{ip}, and CeA-Gq + CNO^{ip} + chronic stress. Scale bars, 100 μm.
(AA) Fos expression in CeA of male mice. One-way ANOVA, $p < 0.0001$.
(BB) Fos expression in CeA of female mice, $p < 0.0001$.
(CC) Fos expression in NTS of male mice, $p < 0.0001$.
(DD) Fos expression in NTS of female mice, $p < 0.0001$.
(EE) Fos expression in DMV in male mice, $p < 0.0001$.
(FF) Fos expression in DMV of female mice, $p < 0.0001$.
All data are presented as mean ± SEM.